2013

Multi-meson systems from Lattice Quantum Chromodynamics

Zhifeng Shi
College of William & Mary - Arts & Sciences

Recommended Citation

Shi, Zhifeng, "Multi-meson systems from Lattice Quantum Chromodynamics" (2013). *Dissertations, Theses, and Masters Projects.* Paper 1539623623.
https://dx.doi.org/doi:10.21220/s2-xsf3-9931

Multi-meson systems from Lattice Quantum Chromodynamics

Zhifeng Shi

Master of Science, College of William and Mary, 2010
Bachelor of Science, Nanjing University, 2008

A Dissertation presented to the Graduate Faculty
of the College of William and Mary in Candidacy for the Degree of
Doctor of Philosophy

Department of Physics

The College of William and Mary
August 2013

APPROVAL PAGE

This Dissertation is submitted in partial fulfillment of
the requirements for the degree of

Doctor of Philosophy

Zhifeng Shi

Approved by the Committee, May, 2013

Co-Committee Chair
Associate Professor Konstantinos Orginos, Physics
The College of William and Mary

Co-Committee Chair
Adjunct Assistant Professor William Detmold, Physics
The College of William and Mary
Assistant Professor, Physics
Massachusetts Institute of Technology

Professor Marc Sher, Physics
The College of William and Mary

Associate Professor Joshua Erlich, Physics
The College of William and Mary

Dr. Robert Edwards, Senior Scientist
Thomas Jefferson National Accelerator Facility

ABSTRACT

Systems of non-zero isospin chemical potential (μ_I), where the chemical potential for up and down quarks is equal in magnitude but of opposite sign, do not suffer from the sign problem, and normal LQCD techniques can be successfully adapted to study such systems. From chiral perturbation theory (χPT), in addition to the deconfined phase transition at high temperature at zero chemical potential, another phase transition from ordinary hadronic states to a Bose Einstein Condensate (BEC) state has been conjectured [1] at non-zero isospin chemical potential. Such a BEC phase is of phenomenological relevance in the interior of neutron stars.

In LQCD, one way to investigate non-zero isospin chemical potential system is from a grand canonical approach by directly working with fermion actions of targeted isospin chemical potentials. Another approach to isospin chemical potential is by explicitly constructing systems of fixed isospin density, and inferring the isospin chemical potential from its ground state energy. In Ref. [2], the first studies of non-zero isospin chemical potential system from this approach were presented, finding that the dependence of the isospin chemical potential on the isospin density agrees with predictions from Ref. [1] at low density. In this thesis, we studied systems with the quantum numbers of up to 72 pions with newly constructed algorithms, and clearly identified the conjectured phase transition from a pion gas to a BEC state at $\mu_I = 1.3\ m_\pi$ at $\mathcal{T} \approx 20$ MeV for the first time.

Having numerically constructed a novel state of matter, a natural question to ask is how it can be investigated. The suppression of J/ψ and Υ resonances [3] at non-zero temperature in heavy ion collision is an important diagnostic of the formation of a quark-gluon plasma. Such suppression effects have been experimentally observed at Super Proton Synchrotron(SPS), RHIC and LHC [3]. Heavy quarks are naturally also expected to be useful probes of phase transitions at non-zero baryon chemical potential and non-zero isospin chemical potential. In this thesis, we investigated both bottomonium and charmonium in media of non-zero isospin chemical potential.

The investigation of QCD at non-zero isospin density presented in this thesis provide a numerical window into a novel state of strongly interacting matter. This matter is difficult to create in experiment but may play an important role in dense astrophysical environments.

TABLE OF CONTENTS

CHAPTER

---

[1] This section is in collaboration with William Detmold, and results have been published in Paper. [4].

[2] This section is in collaboration with William Detmold and Kostas Orignos, and results have been published in Paper. [5].

---

[3] This method is suggested by Anyi Li [6]

[4] This section is in collaboration with William Detmold and Stefan Meinel, and results for bottomonium studies can be found in Ref. [7].

ACKNOWLEDGMENTS

I would like to thank my advisor, William Detmold, for his help in my physics career in last four years, for his patience in going through this thesis, and his important advice.

I present this thesis in honor of my parents.

LIST OF TABLES

LIST OF FIGURES

MULTI-MESON SYSTEMS FROM LATTICE QUANTUM CHROMODYNAMICS

CHAPTER 1

Introduction

Quantum Chromodynamics (QCD) has played important roles in understanding strong interactions between elementary particles, quarks and gluons, which also enables us to understand interactions between hadrons made up of these elementary particles from first principles. At large interacting energies, the strong coupling is relatively small, $\alpha_s(m_Z) = 0.11$ [12], and perturbation theory can be effectively applied, however the strong coupling constant becomes larger with decreasing interacting energies, and eventually perturbation theory starts to fail. At small energies (< 1GeV), the chiral perturbation theory (χPT) has been developed, and it can be effectively used to study such low energy systems by predetermining a few low-energy constants (LECs). However at intermediate energy scales, no analytical method can be applied, and performing non-pertubative calculations from first principles by applying Lattice Quantum Chromodynamics (LQCD) technique is vital in understanding properties of, and interactions between, hadrons at low and intermediate energy scales. QCD is a quantum field theory which is naturally formulated in the form of a path integral in the space of configurations of quark and gluon fields. Such a path integral a functional integral, where the degrees of freedom need to be integrated on every space and time point. In order to define the path integral in a computationally tractable way, space and time are discretized and Monte Carlo methods are applied to numerically estimated such path integrals in LQCD. More details can be found in the next section.

1.1 Path integral

1.1.1 Path integral in Minkowski space

In classical mechanics, only the path having the extreme action is allowed, for example the classical Lagrangian method, which identifies the path minimizing the action as the only physically allowed path. But in Quantum mechanics, all paths are allowed. In order to get correct results, contributions from all paths must be considered, for example the partition function shown in the following equation in Minkowski space includes contributions from all possible paths ($\psi(x)$),

$$Z = \int D[\psi(x)] e^{iS_M[\psi]}, \tag{1.1}$$

where the integration measure, $D[\psi(x)]$, is given by

$$D[\psi(x)] = d\psi(x_1) d\psi(x_2) \cdots d\psi(x_n), \tag{1.2}$$

which denotes that the integration is performed over all paths in every space and time location, x_i. The action

$$S_M(\psi) = \int d^4x \mathcal{L}_M(\psi), \tag{1.3}$$

where $\mathcal{L}_{\mathcal{M}}(\psi)$ is the corresponding Lagrangian in Minkowski space. In QCD equations need to have quarks and gluon fields in them. The QCD Lagrangian, $\mathcal{L}$, is given by

$$\mathcal{L}(\psi,\bar{\psi}),\mathcal{A} = \bar{\psi}^f(x)(i\gamma^\mu D_\mu - m)\psi^f(x) - \frac{1}{4}F^a_{\mu\nu}F^{\mu\nu}_a, \tag{1.4}$$

where $D_\mu = \partial_\mu + iA_\mu$ is covariant derivative, which ensures the gauge invariance, and $\mu = 0, 1, 2, 3$ is the Lorentz index. The ψ^f denotes the fermion field, and $\bar{\psi}^f$ is defined as $\bar{\psi}^f(x) = \psi^{f\dagger}(x)\gamma_0$, where f denotes quark species, f = u, d, c, s, t, b. The gluon gauge tensor, $F^a_{\mu\nu}$, is defined as

$$F^a_{\mu\nu} = \partial_\mu A^a_\nu - \partial_\nu A^a_\mu + gf^{abc}A^b_\mu A^c_\nu, \tag{1.5}$$

where $A(x)$ is the SU(3) algebra-valued gauge field, and f^{abc} are the completely anti-symmetric structure constant, where $a = 1, 2, \cdots, 8$ is the color index. In Equation (1.4), summation over indexes, f and a, is implied. As SU(3) gauge fields do not commute with each other, the last term in Equation (1.5) allows gluons to interact with each other, and thus 3-, and 4- gluon interactions must be included. Such gauge field self-interactions are absent in the electromagnetic interaction.

Physical information about systems interacting with strong interactions can be extracted from correlation functions. An example is the following two point correlation function

$$<\Omega|\psi(x_1)\psi(x_2)|\Omega> = \lim_{T\to\infty(1-i\epsilon)} \frac{\int D[\psi(x)]D[A_u]\mathcal{O}(x_1)\mathcal{O}(x_2)e^{iS_M[\psi]}}{Z_{QCD}}, \tag{1.6}$$

where Ω denotes the vacuum state, $\mathcal{O}(x_1)$ and $\mathcal{O}(x_2)$ are operators of physical states at x_1 and x_2, and the integration over temporal extent is from $-T$ to T. The partition function Z_{QCD} above is given by

$$Z_{QCD} = \lim_{T \to \infty(1-i\epsilon)} \int D[\psi(x)] D[A_u] e^{iS_M[\psi]}. \tag{1.7}$$

From Equation (1.6), the spectrum of states with the corresponding quantum numbers can be extracted and will be discussed below.

1.1.2 Path integral in the Euclidean space

Computing Equation (1.6,1.7) directly leads to great difficulties. Since it is a functional integral, the integration measure is the product of fields at every spacetime location. Such integral involves infinite number of degrees of freedom, and brute force computation of this integral is prohibitive. Additionally, the function in the exponential, $iS[\psi]$, is complex, so the exponential of the action is an oscillating function. Two states having actions separated by many magnitudes can have equally important contributions to the integration. In order to get correct results, detailed cancellations between all contributions are required.

In order to overcome the second difficulty, Wick rotation, can be applied to transform an integration defined in the Minkowski space into an integration in Euclidean space.[1] After rotation, spatial coordinates are untouched, while the temporal coordinate changes according to $\tau \to -it$. Similarly, gamma matrices, field strength tensors, and integration measures are also transformed accordingly. Since the Lagrangian is hermitian, the corresponding action is real. A great benefit that the Wick rotation indeed brings is that the oscillating function e^{iS_M} in Minkowski space is transformed into an exponentially decreasing function e^{-S_E} in Euclidean space.

---

[1] In Minkowski space $x^0 = \tau$, while in Euclidean space $x^4 = t$.

The action in Euclidean space, S_E is given by

$$S_E = \int d^4x \bar{\psi}^f(x)(\gamma^\mu D_\mu + m)\psi^f(x) + \frac{1}{4}F^a_{\mu\nu}F^{\mu\nu}_a. \tag{1.8}$$

Because of the exponential decay property of e^{-S_E}, contributions with small actions dominate the integration. Instead of summing over a large number of states as required in Minkowski space to get a good estimation of the path integral, only a small number of configurations with small actions are required in evaluating the integral after the rotation. Importance sampling techniques can be applied to generate configurations of small actions with the required distribution. Additionally, the original difference between spatial direction and temporal direction, originated from the different signs in $g_{\mu\nu}$, vanished after the transformation. As discussed above, transforming from Minkowski space to Euclidean space brings us multiple advantages in term of applying numerical simulations.

In Euclidean space, the QCD partition function is defined as

$$Z = \int D[\psi(x), \overline{\psi}(x)]D[A_\mu(x)]e^{-S_E[\psi,\overline{\psi}(x)]}, \tag{1.9}$$

where the integration measure $D[\psi(x), \overline{\psi}(x_i)]$ and $D[A_u(x)]$ are

$$\begin{aligned} D[\psi(x), \overline{\psi}(x)] &= d\psi(x_1)d\overline{\psi}(x_1)d\psi(x_2)d\overline{\psi}(x_2)\cdots d\psi(x_n)d\overline{\psi}(x_n) \\ D[A_\mu(x)] &= \prod_{\mu=1}^{4} dA_\mu(x_1)dA_\mu(x_2)\cdots dA_\mu(x_n) \end{aligned} \tag{1.10}$$

The $\psi(x_i)$ ($\overline{\psi}(x_i)$) are quark (anti-quark) fields, and x_i for $i = 1, 2\cdots, n$ is a 4-vector, denoting a single space-time point. Although the oscillating properties of the complex integrand disappears, computing Z involves computing integration over $\psi(x)$ in every space-time location, which is an infinite dimensional integral. To define the path integral in a computationally tractable way, we discretize the whole space and time and impose boundary conditions, and projecting the continuous space-time into a finite dimension lattice, whose dimension is usually around 10^8 sites. Suitable boundary conditions are chosen, for example periodic boundary conditions for three space directions and anti-periodic boundary condition for the fermion field and periodic boundary condition for the gauge field in the temporal direction. Such boundary conditions correspond to considering the field theory at non-zero temperature. A common procedure of LQCD simulation is by first generating configurations with required distributions of actions, which are determined by the fermion action and the gauge action, by applying importance sampling techniques. Partition functions, for example Equation (1.9), and correlation functions of desired quantum numbers (the Euclidean space version of Equation (1.6)) are then calculated on each configuration. Physical information about systems under study can then be extracted from these correlation functions. More details of the methodologies of applying LQCD calculations will be discussed in the next section.

1.1.3 Path Integrals on the Lattice

The partition function defined in Equation (1.9) is an infinite dimensional integral in the continuum, which can be estimated by projecting the continuous space and time onto lattices with finite space and time, which is also a nice way to renormalize the theory. After discretization, the infinite dimension integration measure, $D[\psi(x), \overline{\psi}(x)]$, becomes finite, and it is defined in Equation (1.10). The dimension of $D[\psi(x), \overline{\psi}(x)]$ is $M = 2N_x \times N_y \times N_z \times N_t$ on a lattice, where N_x (N_y, N_z, N_t) denotes lattice size in the direction x (y, z, t), and ψ and $\bar{\psi}$ are considered as independent variables. The fermion action defined in Equation (1.8) can be discretized similarly, which is illustrated in the following example. In a trivial gauge field $A_\mu = 0$, the fermion action for one quark flavor is

$$S_E = \int d^4x\bar{\psi}(x)(\gamma_\mu\partial_\mu + m)\psi(x). \tag{1.11}$$

After discretization, the integral is replaced by summation over sites, and the derivative is replaced by a finite difference[2]. After discretization, the lattice version of Dirac action defined Equation (1.11) is

$$S_E = a^4\sum_{n\in\Gamma}\bar{\psi(n)}\left(\sum_{\mu=1}^{4}\gamma_\mu\frac{\psi(n+\hat{\mu})-\psi(n-\hat{\mu})}{2a}+m\psi(n)\right), \tag{1.12}$$

where a is the lattice spacing, and the summation is over all lattice sites, n, in the 4-dimension lattice Γ.

In order to preserve the gauge invariance of the Dirac action in the continuum, the discretized Dirac action on the lattice needs additional improvements. In order to see the reason, we can consider the following gauge transformation

$$\psi(n) \to \Omega(n)\psi(n) \quad \bar{\psi}(n) = \bar{\psi}(n)\Omega(n)^\dagger. \tag{1.13}$$

The mass term in the discretized Dirac action S_E is invariant, but terms connecting different sites are not gauge invariant, as it transforms as

$$\bar{\psi}(n)\psi(n+\hat{\mu}) \to \bar{\psi}(n)\Omega(n)^\dagger\Omega(n+\hat{\mu})\psi(n+\hat{\mu}). \tag{1.14}$$

The gauge transformation, $\Omega(n)$, defined in different sites are independent, and the combination $\Omega(n)^\dagger\Omega(n+\hat{\mu})$ is not unity for all gauge transformations, thus the lattice version of the QCD action defined in Equation (1.12) is not yet gauge invariant. In

---

[2] Different discretization approach can be used, for example forward/backward difference. Here the central difference is chosen.

order to make the lattice Dirac action invariant, gauge links, $U_{\hat{\mu}}(n)$, connecting sites n and $n+\hat{\mu}$, and transforming accordingly under the gauge transformation are needed to be introduced into the lattice Dirac action. After including such gauge links, the fermion action in Equation (1.12) becomes [3]

$$S = a^4 \sum_{n\in\Gamma} \bar{\psi}(n) \left(\sum_{\mu=1}^{4} \gamma_\mu \frac{U_\mu(n)\psi(n+\hat{\mu}) - U_{-\mu}(n)\psi(n-\hat{\mu})}{2a} + m\psi(n) \right), \tag{1.15}$$

where the gauge link, $U_\mu(n)$, transforms as

$$U_\mu(n) \to \Omega(n) U_\mu(n) \Omega^\dagger(n+\hat{\mu}) \tag{1.16}$$

and

$$U_{-\mu}(n) = U_\mu^\dagger(n-\hat{\mu}). \tag{1.17}$$

Under such a transformation, it can easily be confirmed that the action defined in Equation (1.15) is gauge invariant under transformations defined in Equation (1.13) and(1.16).

As illustrated in Fig. 1.1, quark fields $\bar{\psi}(n)$ and $\psi(n)$ live on sites, and guage links, $U_\mu(n)$ live on the links connecting neighboring sites, n and $n+\hat{\mu}$. The naive action defined in Equation (1.15) has 16 doublers[4] in the massless limit, as can be shown by Fourier transformations of the Dirac action with unit gauge links. In order to eliminate or reduce doubles more advanced actions have been constructed, for example the Wilson action. For the Wilson action, one additional term,

$$-a \sum_{\mu=1}^{4} \bar{\psi}(n) \left(\frac{U_\mu(n)_{ab}\delta_{n+\hat{\mu},m} - 2\delta_{ab}\delta_{n,m} + U_{-\mu}(n)_{ab}\delta_{n-\hat{\mu},m}}{2a^2} \right) \psi(m), \tag{1.18}$$

---

[3] In the rest of the thesis, unless otherwise specified we are exclusively working in the Euclidean space and the index E is dropped from now on.

[4] Doublers are lattice artifacts, which render distinct contributions from different momenta in the continuum being identical after discretization.

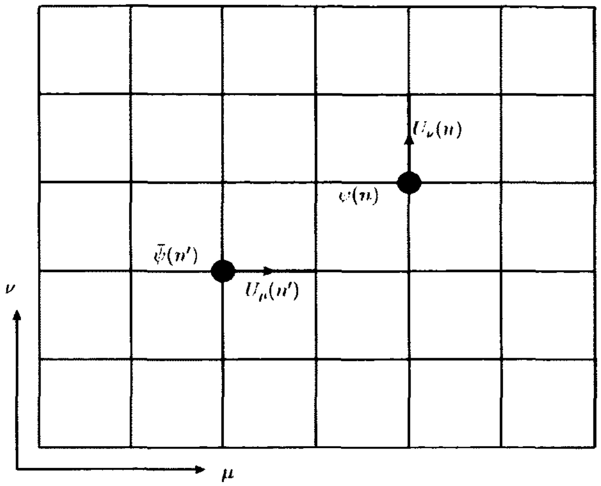

FIG. 1.1: Setup of the LQCD. $\bar{\psi}(n)$ ($\psi(n)$) denotes anti-quark (quark), which are both Grassmann numbers, and $U_\mu(n)$ denotes gauge links, which are SU(3) matrices.

which is the discretization of $-(a/2)\bar{\psi}\partial_\mu\partial_\mu\psi$ and vanishes in the continuum limit, are added into the naive action defined in Equation (1.15). With this additional term, the Wilson fermion action for a single flavor quark is defined as

$$S = a^4 \sum_{n\in\Gamma} \bar{\psi}(n) D(n|m) \psi(m), \tag{1.19}$$

where

$$D(n|m)_{\alpha\beta,ab} = (m + \frac{4}{a})\delta_{\alpha\beta}\delta_{ab}\delta_{n,m} - \frac{1}{2a}\sum_{\mu=\pm1}^{\pm4}(1-\gamma_\mu)_{\alpha\beta}U_\mu(n)_{ab}\delta_{n+\hat{\mu},m}, \tag{1.20}$$

where $\gamma_{-\mu} = -\gamma_\mu$. For each additional flavor, additional Wilson fermions with different masses, m, need to be included. The discretization error of the above action is $\mathcal{O}(a)$, and Symanzik improvement can be applied to reduce the discretization error to $\mathcal{O}(a^2)$. For example in the clover Wilson action [13, 14], the following clover term

$$c_{sw}a^5 \sum_{n\in\Gamma}\sum_{\mu<\nu} \bar{\psi}(n)\frac{1}{2}\sigma_{\mu\nu}\hat{F}_{\mu\nu}\psi(n), \tag{1.21}$$

is added into the Wilson action, Equation (1.20). In Equation (1.21), $\sigma_{\mu\nu} = [\gamma_\mu, \gamma_\nu]/2i$, the parameter c_{sw} needs to be determined perturbatively or non-perturbatively by canceling $\mathcal{O}(a)$ terms in order to get $\mathcal{O}(a^2)$ improvement, and $\hat{F}_{\mu\nu}(n) = \frac{-i}{8a^2}(Q_{\mu\nu}(n) - Q_{\nu\mu}(n))$. The $Q_{\mu\nu}(n)$ is the sum of plaquettes $U_{\mu,\nu}(n)$,

$$Q_{\mu\nu} = U_{\mu,\nu}(n) + U_{\nu,-\mu}(n) + U_{-\mu,-\nu}(n) + U_{-\nu,\mu}(n), \tag{1.22}$$

where $U_{\mu.\nu} = U_\mu(n)U_\nu(n+\hat{\mu})U_\nu(n+\hat{\nu}^\dagger)U_\nu(n)^\dagger$.

From correlation functions of desired quantum numbers, the energy spectrum can be extracted from its exponential decay property as a function of time. In order to get better resolution in the temporal direction, the lattice spacing in the temporal direction, a_t, can be made finer than its counterpart in the spatial direction, a_s, and such a lattice is called an anisotropic lattice with the anisotropic parameter, $\xi = a_s/a_t$. By multiplying the spatial terms in isotropic lattice actions, for example Wilson fermion, by $1/\xi$ and the terms in the temporal direction by ξ, we can get anisotropic lattice actions. By using these advanced actions, the Euclidean version of Equation (1.6) can first be integrated over fermion fields, which are Grassmann numbers, analytically, which give a determinant of the Dirac operator. After this step, the integration over gauge fields are numerically calculated from Monte Carlo importance sampling methods. Throughout this thesis, all computations are performed with the anisotropic clover improved Wilson fermion action. More details can be found in Ref. [15].

Staggered fermions, which define new degrees of freedom based on the spin and color degrees of freedom, have also been applied to alleviate doubling problems. Both Wilson, Clover and Staggered fermions explicitly break chiral symmetry, while some lattice actions satisfying the Ginsparg-Wilson equation

$$D\gamma_5 + \gamma_5 D = aD\gamma_5 D, \tag{1.23}$$

preserving the chiral symmetry on the lattice have been constructed. Example of such actions are Domain-Wall fermion, and overlap fermions. The Domain-Wall fermion action preserves the chiral symmetry in the limit of the infinite fifth dimension, and the overlap fermion conserve chiral symmetry exactly, however simulating overlap fermions is much more expensive and only very recently large volume simulations with overlap fermions become possible. See Ref. [16] for details.

1.1.4 Non-zero (isospin) chemical potential on the lattice

Systems of non-zero chemical potential, non-zero isospin chemical potential and non-zero temperature can be experimentally produced from high energy collision at the Relativistic Heavy Ion Collider (RHIC) or the Large Hadron Collider (LHC). In order to better understand results from experiments, theoretical understanding of similar systems is essential.

In the last few years, many studies have been performed on systems with zero chemical potential and non-zero temperature. As the determinant of the Dirac operator of such systems is positive, importance sampling techniques used in LQCD can be easily adapted to investigate such systems. Indeed, the introduction of non-zero temperature is equivalent to the imposition of boundary conditions in the temporal direction discussed above with $\mathcal{T} \sim \frac{1}{T}$. At low temperatures the system is confined, where quarks are bounded inside hadrons, and at a critical temperature $\sim \mathcal{O}(170)$MeV the system goes through a crossover from a confined phase to a deconfined phase, where quarks propagate freely in the hot medium with little energy cost. Such a crossover can be identified by studying the corresponding order parameters, for example the Polyakov loop, or the quark condensate. Results from different studies using different lattice actions and different volumes all suggest that there is a pseudo critical temperature, where the crossover from a confined phase to a deconfined phase happens. Although different groups find slightly different pseudo critical temperatures, the existence of the crossover is clear. The discrepancies of the quoted critical temperature by different groups results from the different choices of the observable used as the order parameter.

Although systems of non-zero temperatures at zero chemical potential have been investigated extensively, studying non-zero chemical potential systems is exponentially difficult because of the sign problem. Non-zero chemical potential is introduced into the lattice fermion action by giving different weight to the forward and backward temporal gauge links as following:

$$\begin{aligned} U_4(n) &\to \exp(a\mu)U_4(n) \\ U_{-4}(n) &\to \exp(-a\mu)U_{-4}(n), \end{aligned} \tag{1.24}$$

where μ is the chemical potential for quark flavor under consideration. Because of this transformation, the γ_5 hermiticity property of the Dirac operator, $\gamma_5 D(\mu = 0)\gamma_5 = D^\dagger(-\mu = 0)$, no longer holds for non-zero chemical potential, which makes the Dirac determinant complex. Thus systems of non-zero chemical potential suffer from the sign problem, which makes the application of importance sampling techniques used in Monte Carlo simulation very difficult. Various methods have been developed to study non-zero chemical potential systems, for example reweighing, extrapolation from pure imaginary chemical potentials, small chemical potential expansion and so on. Details about these techniques can be found in Ref. [17]. All of these methods involve certain assumptions.

Because of this difficulty, research efforts have been devoted to related, but simpler, systems. As there is no sign problem in a world with two colors because of properties of SU(2) algebra, direct simulations of systems of non-zero chemical potential in two-color QCD have been performed [18], and in this case the transition from the hadronic system to a Bose Einstein Condensate state has been identified at non-zero chemical potential.

In order to study a system more closely related to the three-color world, systems of non-zero isospin chemical potential can also be directly studied by applying current LQCD simulation techniques. In this setup, the chemical potentials of two light quarks are given by $\mu_u = \mu_I$ and $\mu_d = -\mu_I$. Because the chemical potential given to two light quarks having opposite sign, the determinant of the Dirac operator is again positive definite, and it does not suffer from a sign problem. In Ref. [19], systems with non-zero isospin chemical potential have been investigated from χPT, and it has been conjectured that there is a deconfinement phase transition at high temperature and zero isospin chemical potential, and also a phase transition from hadronic states to a Bose-Einstein Condensate state at low temperature at isospin chemical potential of order of the pion mass. From a grand canonical approach, gauge configurations of targeted isospin chemical potential can be generated from Monte Carlo method, and studies on systems with non-zero isospin chemical potential with this method has bee performed in Ref. [19]. This study suggested a transition from hadronic gas to pion condensate phase (BEC) at an isospin chemical potential slightly greater than the mass of one pion, although the calculations have significant uncertainties. Non-zero isospin chemical potential systems can also be studied from a canonical approach by studying systems of fixed isospin charge (multi-meson systems). In Ref [20], such canonical approach has been adopted to study multi-pion and multi-kaon systems, and the relationship between the isospin chemical potential and the isospin density can be computed from ground state energies of multi-particle systems. As a major part of my project, I implemented recursion relation based methods proposed in Ref [9] and studied multi-pion system of up to 24 pions, and I also developed new algorithms to further extend the study of multi-pion system to up to 72 pions. In order to better understand systems at non-zero isospin densities and numerically verify the conjectured BEC transition at non-zero isospin chemical potential, we have also studied the propagation of heavy quarkoniums in the media of different isospin densities.

CHAPTER 2

Multi-meson systems [1]

Important goals of nuclear physics are to study interactions between hadrons, identify two- and multi-body interaction parameters, and investigate the phase shift of interacting particles. As strong interactions are intrinsically non-perturbative at low energies, Lattice Quantum Chromodynamics is the only method to study multi-hadron system from first principles.

Single hadron states can be constructed on the lattice by identifying corresponding operators having the required quantum numbers. Correlation functions of two operators located at $t' = 0$ and $t' = t$ can also be computed on the lattice by contracting matching quark-antiquark propagators, and asymptotically correlation functions assume the following expression

$$\lim_{T\to\infty} \langle \mathcal{O}_2(t)\ \mathcal{O}_1(0) \rangle = \sum_n \langle 0|\hat{\mathcal{O}}_2|n\rangle\ \langle 0|\hat{\mathcal{O}}_1|n\rangle\ e^{-t\ E_n}, \tag{2.1}$$

where only operators with non-zero matrix elements survive, E_n denotes the ground state energy of a particle with the same quantum number as state n, and T is the

---

[1] This section is in collaboration with William Detmold, and results have been published in Paper. [4].

maximal temporal extent. From the asymptotic behavior the above correlation function, both the ground state energy of the hadron and the energies of a few excited states can be extracted by fitting correlation functions to multiple exponentials, or by using Prony's method to separate contributions from different states. Similarly, systems with multi-hadrons can also be constructed from lattice operators; for example various three-baryon systems have been investigated in Ref. [21]. However the number of required Wick contractions between quark and anti-quarks in computing the multi-hadron correlation functions grows factorically ($\mathcal{O}(N_u!N_d!N_s!\cdots)$), where $N_u(N_d,\ N_s)$ is the number of valance up (down, strange) quark in the multi-hadron system. Naively, computing all contractions is prohibitive even for $N = 12\ \pi^+$ systems, which requires $12!12! = 2.3 \times 10^{17}$ contractions.

Since the multi-meson system is computationally less expensive than the multi-baryon system, and it is also a first step toward studying more complex and more interesting multi-baryon systems, we construct algorithms to significantly reduce the numerical cost of computing all contractions, and we also conduct numerical simulations to study multi-meson systems. As discussed in Chapter 1, the sign problem in the non-zero baryon chemical potential systems resulting from the non-positive defined fermion determinant makes directly simulating systems with non-zero baryon chemical potential exponentially difficult. However there is no sign problem for systems with non-zero isospin chemical potential (μ_I), where the up and down quark have the same chemical potential but with opposite signs. One way to simulating non-zero isospin chemical potential systems is by sampling using the fermion determinant with non-zero isospin chemical potential, which is referred to as the grand canonical method. Another approach is the canonical method by explicitly constructing multi-pion systems of finite isospin chemical potential, and inferring the isospin chemical potential from energies of n-pion[2] systems by approximating with

---

[2] Throughout, we use the name "n-pion system" for a system with isospin charge $I_Z = n$.

the finite derivative $\mu_I(n) = \frac{\partial E}{\partial n} = E_n - E_{n-1}$, where E_n is the ground state energy of a n-pion system[3]. From the study of systems of non-zero isospin chemical potential or density at a fixed temperature, the QCD phase diagram can be investigated at varying isospin chemical potentials.

In the next section, we will discuss one way to construct systems with the quantum numbers of n mesons[4], and review the recursion relation methods constructed to perform contractions in such multi-meson systems. However even with the recursion relations, studying systems with more than 24 mesons requires new methods, which will be discussed in Chapter 3.

2.1 n-meson systems from 1 source

In this section, only n-π^+ systems are discussed, however systems containing other mesons can similarly be investigated by substituting the π^+ interpolator with the correct interpolator for the meson to study.

States with the quantum number of one π^+ can be constructed from an operator $\pi^+ = \bar{d}\gamma_5 u$ [5], but it can also be constructed from other operators, for example $\bar{d}\gamma_4\gamma_5 u$. On each lattice site, there are $N_s N_c = 12$ degrees of freedom for each flavor of quark, where N_s (N_c) is the number of spin (color) components, thus a maximum of 12 π^+s can originate from the same lattice site because of the Pauli principle.

Correlation functions of a n-π^+ systems residing in the same source location $\mathbf{y}$

---

[3] This is only an effective chemical potential since the ground state energy is used rather than the total energy

[4] For the convenience, in the following we will call such systems as n-meson system.

[5] In this operator, both u and d quarks are located in the same location, which is called a point source interpolator, the operators connecting quark fields from different locations can also constructed to better mimicking the physical wave function, which could lead to better overlap with the physical state that one is interested in.

can be computed as following,

$$C_{(n\pi^+)}(t) = \left\langle \left(\sum_{\mathbf{x}} \pi^+(\mathbf{x},t) \right)^n \left(\pi^-(\mathbf{y},0) \right)^n \right\rangle . \tag{2.2}$$

This correlation function can be calculated from the corresponding uncontracted correlation function, $Q_{n\pi^+}(t)$,

$$C_{n\pi^+} = (-1)^n n! \langle Q_{n\pi^+}(t) \rangle, \tag{2.3}$$

where $\langle\ \rangle$ stands for taking the trace both in the spin and color index. Initial conditions for $Q_{n\pi^+}$ are $Q_{0\pi^+} = 1, Q_{1\pi^+} = A$, where

$$A = \sum_{\mathbf{x}} S(\mathbf{y},\mathbf{x}) S^+(\mathbf{y},\mathbf{x}), \tag{2.4}$$

where the time dependence of $A(t)$ is omitted, and the γ_5 hemiticity of the quark propagator $S(\mathbf{x},\mathbf{y}) = \gamma_5 S^+(\mathbf{y},\mathbf{x})\gamma_5$ has been applied. The $Q_{n\pi^+}$'s for n-π^+ systems can be computed from the following recursion relation,

$$Q_n = \langle Q_{n-1} \rangle A - (n-1) Q_{n-1} A. \tag{2.5}$$

For the 2-pion correlation function,

$$Q_2 = \langle Q_1 \rangle A - Q_1 A, \qquad \langle Q_2 \rangle = \langle A \rangle^2 - \langle A^2 \rangle, \tag{2.6}$$

which agrees with Ref. [2]. The correlation function for the 3-pion system can be calculated as following

$$
\begin{aligned}
Q_3 &= \langle Q_2 \rangle \; A - 2\langle Q_2 \; A \rangle = \langle A \rangle^2 A - \langle A^2 \rangle A - 2\langle A \rangle A^2 + 2A^3 \\
\langle Q_3 \rangle &= \langle A \rangle^3 - 3\langle A^2 \rangle \langle A \rangle - 2\langle A^3 \rangle \qquad (2.7)
\end{aligned}
$$

which also agrees with Ref. [2]. Other correlation functions can be computed by repeated application of the recursion relation.

2.2 n-meson systems from M sources

In order to study system with more than 12 π^+'s, additional source locations or types are required. We will consider that π^+'s are distributed among M sources, where M is an integer, which allows maximal number of $12M$ π^+'s. One possible correlation function of a system with n_i π^+'s from the i^{th} source is

$$
\begin{aligned}
C_{(n_1\pi_1^+ \;,\ldots,\; n_M\pi_M^+)}(t) &= \Bigg\langle \left(\sum_{\mathbf{x}} \pi^+(\mathbf{x},t) \right)^{\overline{n}} \\
&\qquad \left(\pi^-(\mathbf{y_1},0) \right)^{n_1} \ldots \left(\pi^-(\mathbf{y_M},0) \right)^{n_M} \Bigg\rangle \; , \qquad (2.8)
\end{aligned}
$$

where $\bar{n} = \sum_{i=1}^{M} n_i$. As discovered in Ref. [9], recursion relation for uncontracted correlation functions, $Q_{(n_1,n_2,\ldots,n_M)}(t)$, which are $12M \times 12M$ matrix defined in Equation (2.10), can be applied to study multi-meson systems more effectively than computing all contraction naively. From the $Q_{(n_1,n_2,\ldots,n_M)}(t)$, the corresponding multi-pion correlation functions can be identified as

$$
C_{(n_1\pi_1^+ \;,\ldots,\; n_m\pi_M^+)}(t) = (-)^{\overline{n}} \left(\prod_i n_i! \right) \langle \; Q_{(n_1,n_2,\ldots,n_M)}(t) \; \rangle \quad , \qquad (2.9)
$$

where $\langle\ \rangle$ denotes taking trace over both spin and color degrees of freedom. The ascending recursion relations for the $Q_{(n_1,n_2,\ldots,n_M)}$[6] are

$$\begin{aligned} Q_{(n_1+1,n_2,\ldots,n_M)} &= \langle\, Q_{(n_1,n_2,\ldots,n_M)} \rangle\ P_1 \ -\ \overline{n}\ Q_{(n_1,n_2,\ldots,n_M)} P_1 \\ &\cdots + \langle\, Q_{(n_1+1,n_2,\ldots n_k-1,\ldots,n_M)} \rangle\ P_k \ -\ \overline{n}\ Q_{(n_1+1,n_2,\ldots n_k-1,\ldots,n_M)} P_k \\ &\cdots + \langle\, Q_{(n_1+1,n_2,\ldots,n_M-1)} \rangle\ P_M \ -\ \overline{n}\ Q_{(n_1+1,n_2,\ldots,n_M-1)} P_M \end{aligned} \tag{2.10}$$

and the initial conditions are $Q_{(1,0,\ldots,0)} = P_1, Q_{(0,1,\ldots,0)} = P_2, \cdots$, where P_k is

$$P_k \ = \ \left(\begin{array}{c|c|c|c} 0 & 0 & 0 & 0 \\ \hline \vdots & \cdots & \cdots & \cdots \\ \hline A_{k1} & A_{k2} & \cdots & A_{kM} \\ \hline \vdots & \cdots & \cdots & \cdots \\ \hline 0 & 0 & 0 & 0 \end{array} \right) . \tag{2.11}$$

The $A_{i,j}$'s are uncontracted single pion correlators defined as

$$A_{i,j} = \sum_{\mathbf{x}} S(\mathbf{x}_i, \mathbf{x}) S^{+}(\mathbf{x}_j, \mathbf{x}), \tag{2.12}$$

where the γ_5 hemiticity of the quark propagator $S(\mathbf{x}, \mathbf{x}_j) = \gamma_5 S^{+}(\mathbf{x}_j, \mathbf{x}) \gamma_5$ has been applied. The constructions of $A_{i,j}$ in the 2-source case, that is $i = 1, 2$ and $j = 1, 2$, is schematically represented in Fig.(2.1), where the summation over source location, x, is performed. Because of this summation, $N_c N_s L^3$ pions are allowed at the sink by the Pauli Principle.

Similarly, descending recursion relations for the $Q_{(n_1,n_2,\ldots,n_m)}$ can be constructed

---

[6] The dependence of Q, P and A on the coordinates are suppressed in following discussions for clarity.

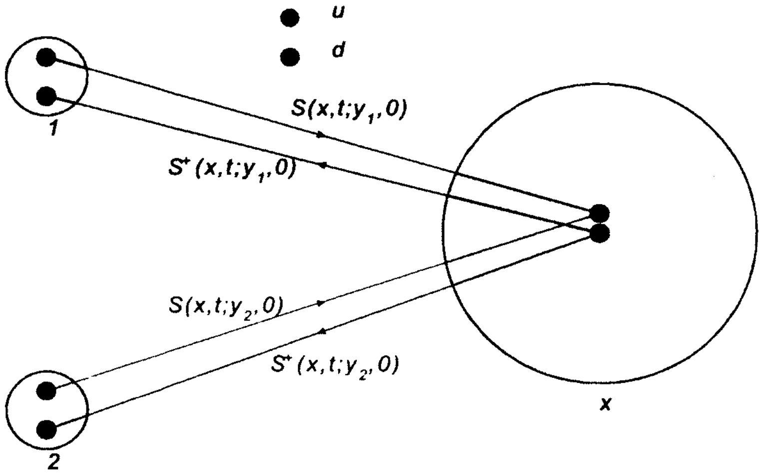

FIG. 2.1: The uncontracted single pion correlation functions from two sources, $A_{i,j}$ for $i, j = 1, 2$, are constructed in the spatial space by starting from source location i, following the line of propagator, integrating over all spatial locations in the sink x, and then returning back to the source j.

as following,

$$Q_{\mathbf{n}} = \sum_{k=1}^{M} \frac{1}{N+1-\bar{n}} \langle Q_{\mathbf{n}+\mathbf{1}_k} A^{-1}\left(P_k \cdot A^{-1}\right)\rangle \cdot I_N - Q_{\mathbf{n}+\mathbf{1}_k} A^{-1}\left(P_k \cdot A^{-1}\right) \quad (2.13)$$

where $\mathbf{n} = (n_1, n_2, \cdots, n_m)$, $\mathbf{1}_k = (0, 0, \cdots, 1, 0, \cdots)$ with only the k^{th} nonvanishing unit element, and $Q_{12,\ldots,12}$, and A are constructed as

$$Q_{12,\ldots,12} = (N-1)!\det(A) \cdot I_N \quad (2.14)$$

$$A = \left(\begin{array}{c|c|c|c} A_{11} & A_{12} & \ldots & A_{1M} \\ \hline \vdots & \ldots & \ldots & \ldots \\ \hline A_{k1} & A_{k2} & \ldots & A_{kM} \\ \hline \vdots & \ldots & \ldots & \ldots \\ \hline A_{M1} & A_{M2} & \ldots & A_{MM} \end{array}\right), \quad (2.15)$$

where $A_{i,j}$'s are single pion uncontracted correlation functions defined in Equation (2.12). Because of the way the recursion relations are constructed, correlation functions of all possible combinations of n_i's for $\sum_{i=1}^{N} n_i < m$ are required to be computed in order to compute correlation functions of m-pion systems. The number of all possible combinations, possible partitions of the integers m, grows exponentially with the number of sources as tabulated in the Table.2.1. Because of the exponential growing number $(13^n - 1)$ of uncontracted correlation functions that need to be computed, along with the size of Q , which is $12M \times 12M$, growing quadratically with the number of source locations, the $n+1$ source computation is significantly more expensive than the n source computation. With the recursion relation methods, systems containing up to 24 π^+'s can be computed within a manageable amount of time and results are presented in Section 2.4.3, however studying systems with more than 24 π^+ from the recursion relation becomes extreamely time consuming. In order to study systems containing even more mesons, new methods are constructed in Chapter. 3.

TABLE 2.1: The third row shows the total number of uncontracted correlation functions required to be computed before getting the correlation function of the maximal allowed pions.

n(# of sources)	1	2	3	4	5
Max # of pions	12	24	36	48	60
total # of combinations	12	168	2196	28560	371292

Similar to the above recursion relations for systems with only one species, recursion relations have also be constructed in Ref. [9] for systems of multi-species.

2.3 Recursion relations in momentum space

Lattice operators constructed from a point source location can not effectively describe physical pions, which have non-zero extents more than a single point. In order to have better overlaps to the physical pion state, lattice operators constructed by combing quark fields from different lattice sites can be utilized. By employing smeared quark fields in source and/or sink, such quark operators can better represent physical pion with finite width, and thus smeared operators give better overlap to pion ground state. On the other hand, we can also employ quark propagators, $S_{u/d}(\mathbf{p}, t; \mathbf{p}', 0)$, from so called gauge fixed wall sources projecting to definite momentum states. Since we consider only gauge invariant correlators, gauge fixing does not alter the result of the functional integration but allows coherent sources to be defined on each configuration. We refer to quark propagator constructed from such sources as colorwave propagators, and they are calculated as

$$S_{u/d}(\mathbf{p}, t; \mathbf{p}', 0) = \sum_{\mathbf{x}} e^{-i\mathbf{p}\mathbf{x}} S_{u/d}(\mathbf{x}, t; \mathbf{p}', 0), \tag{2.16}$$

where

$$S_{u/d}(\mathbf{x}, t; \mathbf{p}', 0) = \sum_{\mathbf{y}} e^{i\mathbf{p}'\mathbf{y}} S_{u/d}(\mathbf{x}, t; \mathbf{y}, 0) \tag{2.17}$$

is a solution of the Dirac equation:

$$\sum_{\mathbf{x},t} D(\mathbf{y}, \tilde{t}; \mathbf{x}, t) S_{u/d}(\mathbf{x}, t; \mathbf{p}', 0) = e^{i\mathbf{p}'\mathbf{y}} \delta_{\tilde{t},0}\,. \tag{2.18}$$

Working in momentum space has the advantage that we can use point source operators in momentum space, while at the same time the system has a good overlap to physical pion systems. The disadvantage is that quark propagators for each momentum have to be computed individually, which would required solving Equation.(2.18) for different momentum choices, $\mathbf{p}'$. Naively computing quark propagator with n different RHSs would required solving n independent sets of linear equations with the same left hand side, of which the computational cost grows linearly with the number n. However by using the fact these n independent linear equations have the same Dirac matrix, such linear systems with different RHSs can be effectively solved by calculating eigenvectors of the Dirac matrix during first few runs, and using the computed eigenvector to speed up the calculation of subsequent linear equations. Details of applying this method to compute quark propagators with multiple RHSs are discussed in Ref. [22].

By utilizing colorwave propagators, correlators for mesons systems, for example π^+, can similarly be constructed. A correlation function of a system having n_1-π^+s in the first source and n_2-π^+s in another source with total momentum $n_1\mathbf{p}_{f_1} + n_2\mathbf{p}_{f_2}$ is:

$$\begin{aligned} C_{n_1\pi^+,n_2\pi^+}(t) &= \left\langle \prod_{i=1}^{2} \left(\sum_{\mathbf{x}_i,\mathbf{x}'_i} e^{-i\left(\mathbf{p}_1^i\mathbf{x}_i - \mathbf{p}_2^i\mathbf{x}'_i\right)} \overline{u}(\mathbf{x}_i, t)\,\gamma_5 d(\mathbf{x}'_i, t) \right)^{n_i} \right. \\ &\cdot \left. \prod_{j=1}^{\overline{n}} \left(\sum_{\mathbf{y}_j} e^{i\mathbf{p}_{f_j}\mathbf{y}_j} \overline{d}(\mathbf{y}_j, 0)\,\gamma_5 u(\mathbf{y}_j, 0) \right) \right\rangle \end{aligned} \tag{2.19}$$

where $\overline{n} = n_1 + n_2$. Momentum conservation requires that $n_1\mathbf{p}_1^1 + n_2\mathbf{p}_1^2 - n_1\mathbf{p}_2^1 - n_2\mathbf{p}_2^2 = \sum_{j=1}^{\overline{n}} \mathbf{p}_{f_j}$ must be satisfied to get non-vanishing $C_{n_1\pi^+,n_2\pi^+}(t)$. Each choice of $\mathbf{p}_j^i, i,j = 1,2$ satisfying this relation is a dependent correlator with the same quantum numbers. By replacing propagators in position space by propagators in momentum space, a similar recursion relation to that presented above still holds as shown in Ref [4]. The only difference is the construction of uncontracted correlation functions $A_{i,j}$ in Equation (2.12). In momentum space, the $A_{i,j}$ are defined as

$$A_{i,j}(t) = \sum_{\mathbf{p}} S\left(\mathbf{p}_i^1, \mathbf{p}\right) S^+\left(\mathbf{p}_j^2, \mathbf{p} - \mathbf{p}_{f_j}\right), \tag{2.20}$$

which are constructed pictorially in Fig. 2.2, where the summation over momentum $\mathbf{p}$ is implied, and dependence on $\mathbf{p}^1, \mathbf{p}^2$ is suppressed.

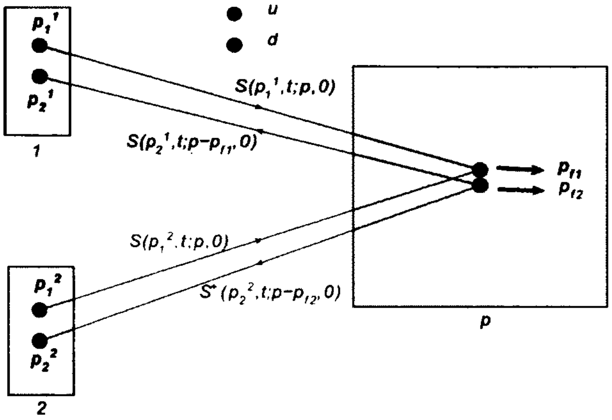

FIG. 2.2: The figure shows how to construct pion correlation function in momentum space. $A_{i,j}$ is constructed by following the line from source i to p, returning to source j, multiplying the $S(S^\dagger)$ with respect to each line and summing over p.

2.4 Simulation details

Using the recursion methods, we have studied systems with up to 24 pions. Multi-pion correlation functions have been calculated on ensembles of anisotropic gauge field configurations with clover-improved fermion actions generated by the Hadron Spectrum Collaboration and the Nuclear Physics with Lattice QCD collaboration. The gauge action is a tree-level tadpole-improved Symanzik-improved action [23], and the fermion action is a $n_f = 2+1$ anisotropic clover action with two levels of stout smearing [24] with weight $\rho = 0.14$ only in spatial directions. In order to preserve the ultra-locality of the action in the temporal direction, no smearing is performed in that direction. Furthermore, the tree-level tadpole-improved Symanzik gauge action without a 1×2 rectangle in the time direction is used.

Calculations have been performed on ensembles of gauge configurations, $L^3 \times T = \{16^3, 20^3, 24^3\} \times 128$, with the spatial lattice spacing of $a_s = 0.1227 \pm 0.0008$ fm, and the anisotropy parameter of $\xi = a_s/a_t = 3.5$ determined from the energy-momentum dispersion relationship. On these ensembles, the quark masses are such that pion has a mass of $m_\pi = 390$ MeV, and the kaon has a mass of $m_K = 540$ MeV. Ideally, one would like to work at physical quark masses, however simulating at physical masses suffers from slow convergence and singular configurations because of existence of small eigenvalues of the Dirac matrix. Larger computational resources are required to directly exploring systems at physical masses, see Ref. [25]. The quantities $m_\pi L$ and $m_\pi T$ governing the impact of the finite volume and finite temporal extent are $m_\pi L \sim 3.86, 4.82, 5.79$ and $m_\pi T \sim 8.82$ respectively.

In our work, colorwave propagators, $S_{u/d}(\mathbf{p}, t; \mathbf{p}', 0)$, are used in the recursion relations, and they are generated from Coulomb gauge fixed configurations. On the $16^3 \times 128$ ensembles, propagators with 33 different momenta satisfying $|\mathbf{p}| < 5$ have been generated with the methods constructed in Ref. [22], while on the $20^3 \times 128$ and the $24^3 \times 128$ ensemble propagators with 19 momenta satisfying $|\mathbf{p}| < 3$ are generated. Pion systems with the same total four momentum can be constructed from different combination of quark momenta[7], but some combinations can have larger contributions than others [8]. In order to get better signals, correlation functions computed from different choices of momenta are averaged on each gauge configuration.

2.4.1 Multi-pion dispersion relation

According to the Equation(2.19), only those correlation functions satisfying the momentum conservation have non-vanishing results. The momentum of individual pion is given by $\mathbf{p}_1^1 - \mathbf{p}_1^2$. Multi-pion systems with zero total momentum can be constructed from pions moving with non-zero momentum, however such construction of zero total momentum system has much smaller contribution to the ground states than by enforcing individual pion having zero momentum. The small size of the

---

[7] Quark momentum is not a well defined quantum number, and it can be recognized as an independent operator choice which facilitates the computation.

[8] Correlation functions calculated by using different quark momentum combinations on the same configuration are strongly correlated, because propagators with different momenta are generated from the same gauge field.

contributions from moving pions have also been numerically verified.

Because of the way multi-pion systems are constructed in Equation (2.19), pions located in the same source have the same momentum. Moving systems are constructed from pions with the same momentum from a single source. On discrete lattices, only the multiplets of the momentum $\delta p = \frac{2\pi}{L}$ are allowed. In units of δp, moving systems with total momentums of $\mathbf{p}_t = n \cdot \mathbf{p}$, where $\mathbf{p}$ is the momentum of an individual pion, and $\mathbf{p} = (0,0,1), (0,1,1)$, and $(0,0,2)$ have been computed. As the noise to signal ratio (N/S) of the correlation function of a moving system having a center of mass momentum of $\mathbf{p_t}$ is proportional to $e^{(E_n(\mathbf{p_t})-\mathbf{E_n}(\mathbf{p}=(\mathbf{0},\mathbf{0},\mathbf{0})))\mathbf{t}}$ [26], where $E_n(\mathbf{p} = (0,0,0)))t$ is lowest energy of the state that n-pion operator contributes, the uncertainty of correlation functions becomes larger as $\mathbf{p_t}$ becomes larger. This makes the extrapolation of the ground state energy less accurate for larger $\mathbf{p_t}$. Because of the N/S problem, only energies of one pion systems for $\mathbf{p} = (0,0,0), (0,0,1), (0,1,1)$, and $(0,0,2)$ respectively have been extracted, and the corresponding plot of $(E(\mathbf{p}_t)a_t)^2$ as a function of $(\mathbf{p}a_t)^2$ is shown in Fig. 2.3. By fitting to the dispersion relation, $(E(\mathbf{p})a_t)^2 = (E(\mathbf{0})a_t)^2 + c^2(\mathbf{p}a_t)^2$, we get $c = 1.007(12)$, which is consistent with $c = 1.0$. By choosing different combinations of quark momenta, pions with definite momentum can be effective constructed from the colorwave propagators.

2.4.2 Correlation functions of n-π^+ systems from 1 source

By contracting the colorwave propagators according to the recursion relation defined in momentum space, n-π^+ correlation functions defined in the Equation (2.19) can be effectively computed. Because of the Pauli principle, only $N_sN_c = 12$ π^+'s can be put in the same momentum while still getting non-vanishing correlation functions. In order to study systems containing more than 12 π^+'s, additional source

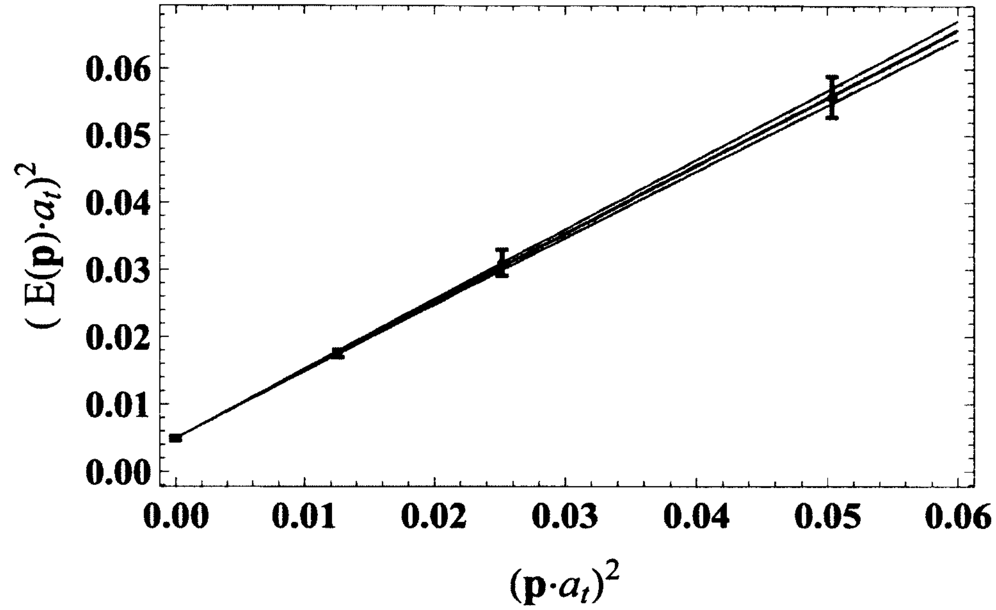

FIG. 2.3: The extracted energies of a single pion with different momenta are plotted as the function of the momenta. In this plot, $(E(\mathbf{p})a_t)^2$ are plotted against $(\mathbf{p}a_t)^2$. Together the fit to the dispersion relation is plotted, along with its 95% confidence interval.

locations are required.

On lattices with finite temporal extent, T, correlation functions of n-π systems contain thermal states, where some part of the system propagates backward across the temporal boundary to get to the sink. These contributions are particular important for multi-hadron states as they easily factorize into multiple color singlet objects that can propagate over large distance. By including the contributions from all thermals states, the n-π correlation functions on a finite lattice with temporal extent of T behaves as

$$\begin{aligned}
C_{n\pi}(t) &= \frac{1}{Z_0} tr[e^{-(T-t)\hat{H}}\ \hat{O}_2\ e^{-t\hat{H}}\ \hat{O}_1] \\
&= \frac{1}{Z_0}\sum_m \langle m|e^{-(T-t)\hat{H}}\ \hat{O}_2\ e^{-t\hat{H}}\ \hat{O}_1|m\rangle \\
&= \frac{1}{Z_0}\sum_{m,n-m} \langle m|e^{-(T-t)\hat{H}}\ \hat{O}_2|n-m\rangle\langle n-m|\ e^{-t\hat{H}}\ \hat{O}_1|m\rangle \\
&= \frac{1}{Z_0}\sum_{m,n-m} \langle m|\ \hat{O}_2|n-m\rangle\langle n-m|\ \hat{O}_1|m\rangle e^{-(T-t)E_m}\ e^{-tE_{n-m}} \\
&= \frac{1}{2}\sum_{m=0}^{\lfloor\frac{n}{2}\rfloor}\binom{n}{m} A^n_m Z^n_m e^{-E_m t} e^{-E_{n-m}(T-t)} + e^{-E_m(T-t)} e^{-E_{n-m}t} + \ldots \\
&= \sum_{m=0}^{\lfloor\frac{n}{2}\rfloor}\binom{n}{m} A^n_m Z^n_m e^{-(E_{n-m}+E_m)T/2} \\
&\cdot\ (e^{-E_m(t-T/2)} e^{E_{n-m}(t-T/2)} + e^{E_m(t-T/2)} e^{-E_{n-m}(t-T/2)})/2 + \ldots \\
&= \sum_{m=0}^{\lfloor\frac{n}{2}\rfloor}\binom{n}{m} A^n_m Z^n_m e^{-(E_{n-m}+E_m)T/2}\cosh((E_{n-m}-E_m)(t-T/2)) + \ldots
\end{aligned} \tag{2.21}$$

In the above equation,tr stands for trace, which is evaluated in the Hilbert space by summing over all quantum states, m. The matrix element $\langle n-m|e^{-(T-t)\hat{H}}\ \hat{O}_1|m\rangle$ denotes contributions from m pions propagating in an opposite direction of the rest $n-m$ pions, and in the limit $T \to \infty$ contributions form this term vanishes. In the step 5, we simplified the notations to $A^n_m = 1$ when $m = n/2$, otherwise $A^n_m = 2$, and the Z^n_m are the overlap factors for contribution with m π's propagating backward around the temporal boundary, and the ellipsis denotes contributions from excited states, which are suppressed by the energy gap. The E_m is the ground state energy of a m-π^+ system. The ground state contribution comes from the $m = 0$ term, and thermal states, which vanishes in the $T \to \infty$ limit are from the $m \neq 0$ terms in the sum.

An example of the contributions of the excited states, ground states, and thermal states can be visualized in Fig. 2.4, where the red points with error bars are the

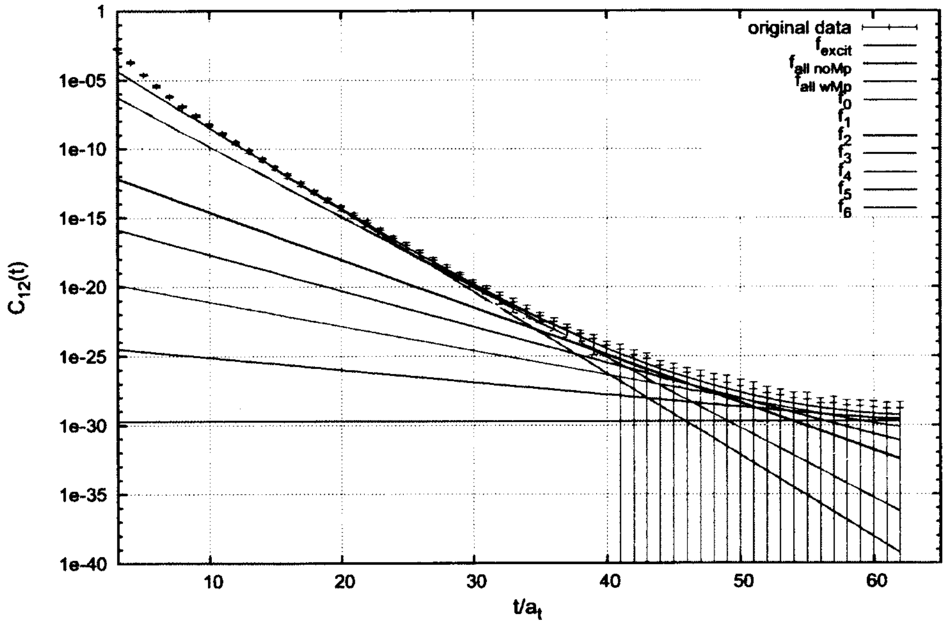

FIG. 2.4: In this figure, the correlation function of systems containing 12-π, denoted as $C_{12}(t)$, is decomposed into different contributions to get a better understanding of the difficult in extracting ground state energies resulting from the necessity to including all thermal contributions in the fit. "$f_{\text{all wMp}}$" is by summing all contributions, and "$f_{\text{all noMp}}$" denotes contributions only from the ground state and thermal states, which overlaps exactly with the "$f_{\text{all wMp}}$" at latter time slices, and lays over the ground state contribution "f_0" at earlier time slices. "f_{excit}" denotes the contribution from the first excited state, which dominates the "$f_{\text{all wMp}}$" at early time slices. "f_1" represents the contribution from the 1st thermal states, where 1 pion propagates in an opposite direction with others, and similar "f_k" denotes contributions from the kth thermals states, where k pions propagate in the opposite temporal direction to other $12 - k$ pions.

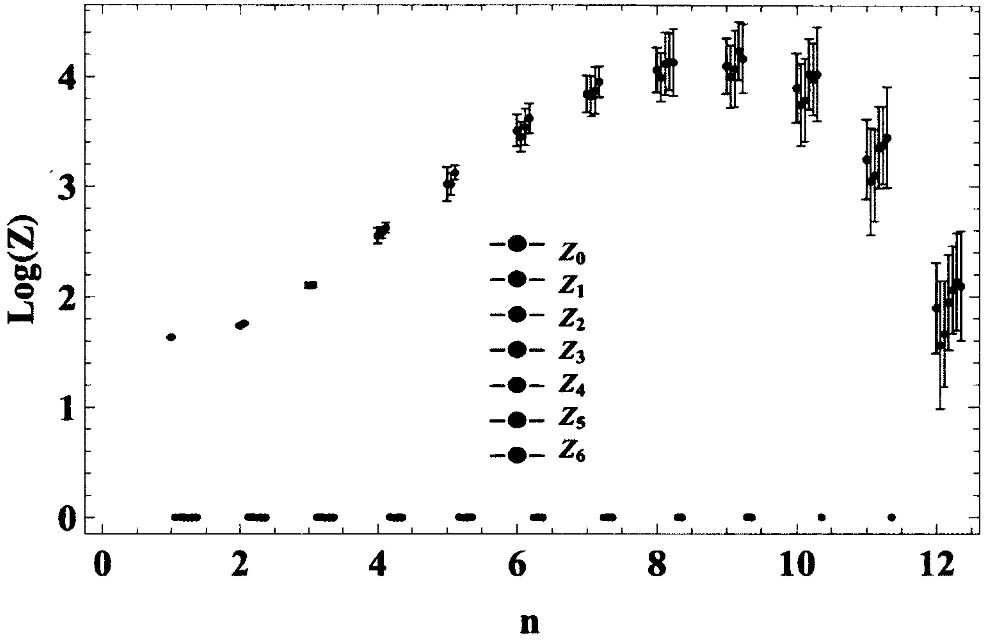

FIG. 2.5: In this plot, Z factors, Z_i for $i = 0, 1, \cdots, 6$, extracted fitting correlation functions for n pions for n up to 12 are compared. Z_0 denotes contribution from the ground state, and Z_i denotes the contribution from thermal states with i pions propagating in the opposite direction with other pions.

data of the correlation function of a rest system having 12-π^+, $C_{12}(t)$, calculated from a single source on the $16^3 \times 128$ ensemble. In order to get better overlap to the ground state, interpolating fields are constructed such that all pions in the rest system have zero momentum in the absence of interactions. In Fig. 2.4, "$f_{\text{all wMp}}$" is by summing the 1^{st} excited state, ground state, and all thermal state contributions. The "$f_{\text{all noMp}}$" denotes contributions only from the ground state and thermal states, which overlaps exactly with the "$f_{\text{all wMp}}$" at latter time slices, and lays over the ground state contribution "f_0" at earlier time slices. "f_{excit}" denotes the contribution from the first excited state, which dominates the "$f_{\text{all wMp}}$" at early time slices. "f_1" represents the contribution from the 1st thermal states, where 1 pion propagates in an opposite direction with others, and similar "f_k" denotes contributions from the kth thermals states, where k pions propagate in the opposite temporal direction to other $12 - k$ pions.

As we can see, even for systems with 12 pions, there is no region where the ground state dominates, thus in order to extract the ground state energy we need to fit the corresponding correlation functions for $n = 1, 2, \cdots$ pions to the Equation (2.21) by including all thermal states. As the energies of the states with $m < n$ pion can be extracted from correlation functions of systems having less pions, there are only one energy and multiple Z factors needed to be determined from the fit.

However, the Z factors for the ground state and thermal states are the same within uncertainty as shown in the Fig. 2.5 and we can build this simplifing assumption into the fits, which further reduce the number of parameters to be determined during each fit to two. The uncertainties of extracted ground state energies include the following three contributions. First, there is intrinsic statistical uncertainty coming from the Monte Carlo estimations, which can be effectively estimated from the bootstrap/jackknife method. Secondly, one kind of systematic uncertainty comes from the fit region we choose, where other contributions, for example excited states, are not included in our fit. Such uncertainty cam be estimated by choosing different fitting windows, and examining the deviation of the extracted ground state energy for different fitting ranges. Another systematic uncertainty comes from the fact that the energies used as a prior for the thermal states extracted with uncertainties themselves, and the contribution of this kind of systematic uncertainty is difficult to estimate. For few-pion systems, thermal state energies are relatively small and so are their uncertainties, thus their contributions to the systematic uncertainty of the ground state energy is relatively smaller than the statistical uncertainty.

However, for system with more pions, such systematic contributions are magnified, and it also becomes even more difficult to estimate such a contribution. Because of the difficultly in extracting the ground state energies, and also in estimating systematic uncertainties, extracting the ground state energies for system containing more than 12-π on the $T = 128$ lattice is very difficult, and we become less confident on the extracted ground energies for systems of more pions. Extracted ground state energies will be shown in the following section.

2.4.3 Multi-pion systems from 2 sources

Because of the Pauli principle, only $N_s N_c = 12$ pions can be constructed from a single source set up. In order to study systems having more than N pions, a minimal of ceiling($N/12$) source locations are required. From 2-source setups, a maximal of 24-pion system can be studied. Complications of 2-source studies comes from both the fact that the uncontracted correlation matrices are 24×24 complex matrices rather than 12×12 for the one source calculation, and that the number of possible ways to distribute pions between two source locations is 10 times larger than the one source case. These two factors make the study of 2-source systems $\mathcal{O}(100)$ more expensive than the 1-source study. Similar argument makes the study of 3-source system $\mathcal{O}(100)$ more expensive than the 2-source study.

Correlation functions for systems having $n_1(n_2)$ π's from the 1st and 2nd source, $C_{n_1,n_2}(t)$, can be calculated in the momentum space by using Equation (2.19). By implementing the recursion relation, correlation functions of all possible ways of distributing pions between two sources can be calculated. By fitting $C_{n_1,n_2}(t)$ according to the Equation. (2.21), ground state energies, E_{n_1,n_2}, are extracted from $C_{n_1,n_2}(t)$ for individual combinations of n_1 and n_2. Extracted E_{n_1,n_2}'s are compared in Fig. 2.6, which confirms that the ground state energy of a multi-pion system is independent of the distribution of pions between all sources.

Comparing to the 1-source system, fitting 2-source system requires more free parameters to be fitted, thus in addition to the large computational cost of the correlation function, extracting ground state energies from correlators also become more difficult. This is why we only extracted E_{n_1,n_2} for systems with up to 10 pions.

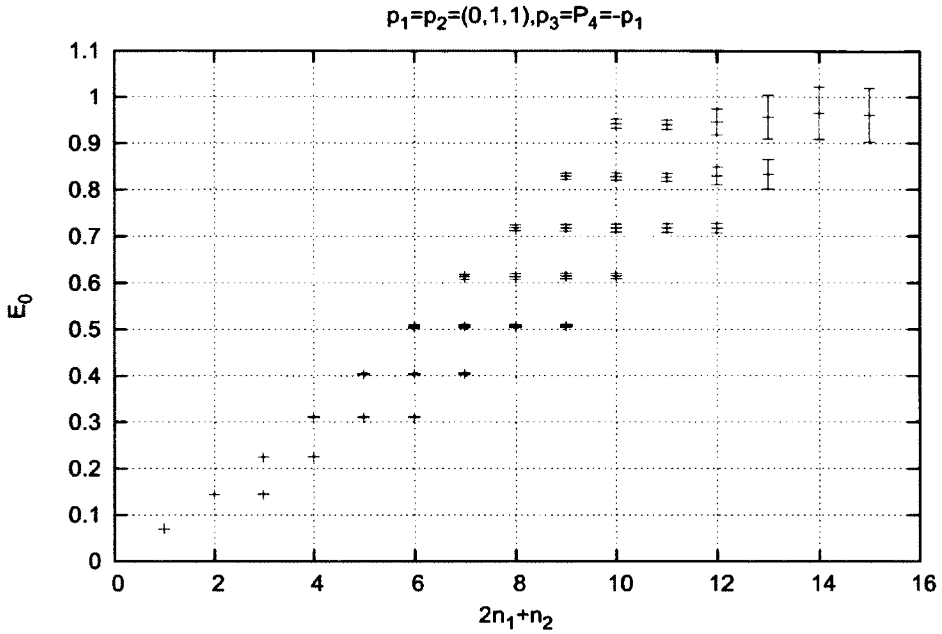

FIG. 2.6: The ground state energies, E_{n_1,n_2}, extracted from $C_{n_1,n_2}(t)$ for different n_1 and n_2 are compared. The x-axis are chosen to be $2n_1 + n_2$ in order to separate E_{n_1,n_2} with the same $n_1 + n_2$. The nth row corresponds to the ground state energy of an n-pion system.

Even though we are able to compute $C_{n_1,n_2}(t)$ for $n_1 + n_2$ up to 24, ground state energies are hard to extract reliably for large number of pions. In order to get better signal for ground state, longer temporal extent are needed to suppress contributions from thermal states propagating around the temporal boundary. Studying systems containing more than 24 pions would require a third source, as discussed before, the 3-source computation is $\mathcal{O}(100)$ times more expensive than the 2-source calculation, which make the computation of correlation functions of systems of more than 24 pions extremely time consuming. In order to study systems with more pions, new methodologies are developed in the following section.

CHAPTER 3

Improved methods to study many-meson systems [1]

As discussed in the previous chapter, a recursion relation for the $C_{n_1,\ldots,n_N}(t)$ can be derived and it has been applied in the last section to study systems containing up to 24 pions. Since the spectrum is independent of the choice of interpolating operators used to probe it, the $C_{n_1,\ldots,n_N}(t)$'s have the same energy spectrum for all possible combinations of n_i's as long as $\overline{n}$ is fixed, so separately computing correlation functions of all combinations of n_i's is redundant. This has been verified numerically for the case of 2 sources in Section. 2.4.3. As we are primarily interested in the energy spectrum of multi-pion systems, we can thus identify a combined correlator $C_{\overline{n}\pi}(t)$ as the term having prefactor λ^n from the expansion of $\det[1 + \lambda A]$,

---

[1] This section is in collaboration with William Detmold and Kostas Orignos, and results have been published in Paper. [5].

with

$$A = P_1 + P_2 + \ldots + P_N = \left(\begin{array}{c|c|c|c} P_{1,1} & P_{1,2} & \ldots & P_{1,N} \\ \hline \vdots & \ldots & \ldots & \ldots \\ \hline P_{k,1} & P_{k,2} & \ldots & P_{k,N} \\ \hline \vdots & \ldots & \ldots & \ldots \\ \hline P_{N,1} & P_{N,2} & \ldots & P_{N,N} \end{array}\right), \tag{3.1}$$

where P_k's are defined in Equation (2.11).

$C_{\overline{n}\pi}(t)$ computed in such a manner is a complicated combination of the various $C_{n_1,n_2,\ldots,n_N}(t)$ with fixed $\overline{n}$, in which we do not identify which pions originate from which source as this is not physically useful information. For multiple source contractions, even terms representing more than 12 π^+'s located in a single source are included, however such terms vanish identically and so do not produce additional noise in numerical calculations. As many fewer correlation functions are needed for a given $\overline{n}$, computing $C_{\overline{n}\pi}(t)$ is a computationally simpler task than recursively computing all $C_{n_1,n_2,\ldots,n_N}(t)$. In the following sections, we will construct four algorithms to further speed up the calculation of $C_{\overline{n}\pi}(t)$ and compare each algorithm in terms of precision requirement and numerical cost. By applying these new algorithms, we will investigate systems containing up to 72 pions in Chapter 4.

3.1 Vandermonde Matrix method (VMm)

As described above, the correlation function of an n-π^+ system ($C_{n\pi}$) can be identified as the coefficient of λ^n from the power series expansion of $\det[1 + \lambda A]$

$$\det[1 + \lambda A] = 1 + \lambda C_{1\pi} + \lambda^2 C_{2\pi} + \ldots + \lambda^{12N} C_{12N\pi}, \tag{3.2}$$

where A is a $12N \times 12N$ matrix[2] constructed from uncontracted correlators following Eq. (3.1). A simple way to get $C_{n\pi}$ is by computing Eq. (3.2) for $12N$ different choices of λ $(\lambda_1, \ldots, \lambda_{12N})$. The resulting system of equations can be written in the following matrix form

$$\begin{pmatrix} \frac{\det[1+\lambda_1 A]-1}{\lambda_1} \\ \frac{\det[1+\lambda_2 A]-1}{\lambda_2} \\ \vdots \\ \frac{\det[1+\lambda_{12N} A]-1}{\lambda_{12N}} \end{pmatrix} = \begin{pmatrix} 1 & \lambda_1 & \lambda_1^2 & \ldots & \lambda_1^{12N-1} \\ 1 & \lambda_2 & \lambda_2^2 & \ldots & \lambda_2^{12N-1} \\ \vdots & & & & \\ 1 & \lambda_n & \lambda_n^2 & \ldots & \lambda_n^{12N-1} \end{pmatrix} \cdot \begin{pmatrix} C_{1\pi} \\ C_{2\pi} \\ \vdots \\ C_{12N\pi} \end{pmatrix} . \tag{3.3}$$

The matrix on the RHS of Eq. (3.3) is a $12N \times 12N$ Vandermonde matrix, for which there exist analytical forms for the determinant and inverse (see for example Ref. [27]). The inverse matrix then allows us to determine the $C_{n\pi}$'s from the numerical calculation of the determinant vector. However, when the number of sources becomes large, elements of this matrix can become very small or very large because of the factors of $\lambda_i^{1,2,\ldots,12N-1}$, which makes the computation of the inverse very demanding in precision and eventually resulting in significant numerical errors unless very high precision is used.

3.2 FFT method (FFTm)

By choosing $\lambda = \exp(i2\pi f_0 \cdot \tau)$ in Eq. (3.2), the expansion becomes

$$\det[1 + \lambda A] = 1 + e^{2i\pi f_0 \cdot \tau} C_{1\pi} + e^{4i\pi f_0 \cdot \tau} C_{2\pi} + \ldots + e^{24i\pi N f_0 \cdot \tau} C_{12N\pi}, \tag{3.4}$$

which contains contributions from signals of frequencies kf_0, $k = 1, 2, \ldots 12N$, which can be thought of as a Fourier series. Because of this feature, the magnitude of

---

[2] In pervious chapter M denotes the number of source, while in this chapter N is used to denote the number of source.

each frequency component can easily be extracted using a Fast Fourier Transform (FFT). The magnitude corresponding to frequency kf_0 is equivalent to $C_{k\pi}$ times a normalization constant, which depends on f_0 and τ. In order to get better signals, data from multiple τ's are beneficial, which results in the need to calculate many determinants, and makes this method expensive. On the other hand, specific choices of f_0 and τ can minimize the number of required determinants. We set $\tau_n = n\ dt$, for $n = 1, 2, \ldots, T$ where dt is the minimal time step and T is the closest prime number larger than $12N$, and $f_0 = \frac{1}{dt \cdot T}$ and then compute $\det[1 + \lambda_n A]$ with $\lambda_n = \exp(i2\pi f_0 \cdot \tau_n)$. After applying the FFT to this series, the amplitude of the frequency kf_0 is $TC_{k\pi}$. With such choices of f_0, τ_n and T, the number of determinants needed to compute is the same as the Improved Combination method (ICm) discussed below.

3.3 Combination method (Cm)

The FFTm discussed above is constructed from a certain choice of λ's so that the expansion of the determinant can be recognized as contributions from different frequencies. Similarly, by studying the properties of Eq. (3.2), another choice of λ's can be utilized to eventually separate $\det[1+\lambda A]$ into groups of functions individually depending only on 3 correlation functions. This method requires us to determine the inverse of a 3×3 matrix, rather than of a $12N \times 12N$ Vandermande matrix, to solve for the individual correlators and is thus more numerically stable. This method is applied by the following steps:

Step 1: Choose $f_1 = 1$ and compute

$$\begin{aligned} D_1^{(1)}(f_1\lambda) &= \det[1 + f_1\lambda A] - 1 \\ &= f_1\lambda C_{1\pi} + (f_1\lambda)^2 C_{2\pi} + \cdots + (f_1\lambda)^{12N} C_{12N\pi} \end{aligned} \tag{3.5}$$

Notice that $D_1^{(1)}(f_1\lambda)$ depends on all correlators $C_{1\pi}, C_{2\pi}, \ldots, C_{12N\pi}$.

Step 2: Choose $f_2 = \exp(i\pi)$, and construct the following contractions of the functions $D_1^{(1)}(f_n\lambda)$ to generate the following two new quantities:

$$\begin{aligned} D_1^{(2)}(\lambda) &= D_1^{(1)}(f_1\lambda) + f_1 D_1^{(1)}(f_2\lambda), \\ D_2^{(2)}(\lambda) &= D_1^{(1)}(f_1\lambda) + f_2 D_1^{(1)}(f_2\lambda). \end{aligned} \tag{3.6}$$

By inserting the values of $f_1 = 1$, $f_2 = -1$, it is clear that the $D_i^{(2)}(\lambda)$ only depend on $C_{(3-i)\pi}, C_{(5-i)\pi}, \ldots$, and so the correlation functions have been separated into two groups. Specifically, we have

$$\begin{aligned} D_1^{(2)} &= \lambda^2 C_{2\pi} + \lambda^4 C_{4\pi} + \cdots \\ D_2^{(2)} &= \lambda^1 C_{1\pi} + \lambda^3 C_{3\pi} + \cdots \end{aligned} \tag{3.7}$$

Step 3: Choose $f_3 = \exp(i\frac{\pi}{2})$, and construct the following combinations of the functions $D_1^{(2)}(f_n\lambda)$ and $D_2^{(2)}(f_n\lambda)$:

$$\begin{aligned} D_1^{(3)}(\lambda) &= D_1^{(2)}(\lambda) + f_1 D_1^{(2)}(f_3\lambda), \qquad (3.8) \\ D_2^{(3)}(\lambda) &= D_1^{(2)}(\lambda) + f_2 D_1^{(2)}(f_3\lambda), \\ D_3^{(3)}(\lambda) &= D_2^{(2)}(\lambda) + f_1 f_3 D_2^{(2)}(f_3\lambda), \\ D_4^{(3)}(\lambda) &= D_2^{(2)}(\lambda) + f_2 f_3 D_2^{(2)}(f_3\lambda), \end{aligned}$$

and we see that the $D_i^{(3)}(\lambda)$ for $i = 1, 2$ depends on $C_{(0+2i)\pi}, C_{(4+2i)\pi}, \ldots$, and $D_i^{(3)}(\lambda)$ for $i = 3, 4$ depends on $C_{(9-2i)\pi}, C_{(13-2i)\pi}, \ldots$. In each step, one function depending on a block of $C_{k\pi}$'s is separated into two functions each depending only on half of the $C_{k\pi}$'s from the previous function. We iterate this procedure until blocks of only

3 $C_{k\pi}$'s are reached.

To summarize this method, in "step n", $f_n = \exp(i\frac{\pi}{2^{n-2}})$ is chosen, and after this step $D_i^{(n-1)}(\lambda)$, $i = 1, \ldots, 2^{n-2}$, will be separated into 2^{n-1} functions, $D_i^{(n)}(\lambda)$, each depending on $12N/2^{n-1}$ $C_{k\pi}$'s. At a given stage, $D_m^{(n-1)}(\lambda)$ is a function depending on a block of $C_{k\pi}$'s. Two functions, $D_{2m-1}^{(n)}$ and $D_{2m}^{(n)}$, each depending on a half of the original block of $C_{k\pi}$'s are constructed from $D_m^{(n-1)}(\lambda) + q_{2m-1} \cdot D_m^{(n-1)}(f_n \cdot \lambda)$ and $D_m^{(n-1)}(\lambda) + q_{2m} \cdot D_m^{(n-1)}(f_n \cdot \lambda)$, where the q_k's, $k = 1, 2, \ldots, 2^{n-1}$, are prefactors used to construct new functions depending only on half of the $C_{k\pi}$'s, which $D_m^{(n-1)}(\lambda)$ depends on. The prefactor q_k in step n is constructed in the following way.

$$\begin{array}{lrcl} \text{Group 1:} & q_1 & = & f_1, \\ \text{Group 2:} & q_2 & = & f_2 \cdot q_1, \\ \text{Group 3:} & q_k & = & f_3 \cdot q_{k-2}, k = 3, 4, \\ & \vdots & & \\ \text{Group n:} & q_k & = & f_n \cdot q_{k-2^{n-2}}, k = 2^{n-2}+1, 2^{n-2}+2, ..., 2^{n-1}, \end{array} \quad (3.9)$$

where "Group m" contains 2^{m-2} functions for $m = 2, 3, \ldots, n$. This process is repeated until functions, $D_k^{(\tilde{n})}(\lambda)$, each depending only on 3 $C_{i\pi}$'s are reached. Eventually $\det[1 + \lambda A]$ is separated into functions, $D_k^{(\tilde{n})}(\lambda)$, depending on following blocks

(B_k):

$$\begin{array}{ll}
\text{Group 1:} & B_1 = [C_{4N\pi}, C_{8N\pi}, C_{12N\pi}] \\
\text{Group 2:} & B_2 = [C_{2N\pi}, C_{6N\pi}, C_{10N\pi}] \equiv C_{\text{Sub}(B_1)-2N} \\
\text{Group 3:} & \left\{ \begin{array}{lcl} B_3 & = & [C_{3N\pi}, C_{7N\pi}, C_{11N\pi}] \equiv C_{\text{Sub}(B_1)-N} \\ B_4 & = & [C_{N\pi}, C_{5N\pi}, C_{9N\pi}] \equiv C_{\text{Sub}(B_2)-N} \end{array} \right. \\
\vdots & \\
\text{Group n:} & B_k = C_{\text{Sub}(B_{k-2^{n-2}})-\frac{4N}{2^{n-2}}}, k = 2^{n-2}+1, 2^{n-2}+2, \dots, 2^{n-1}
\end{array} \tag{3.10}$$

where $\text{Sub}(B_k)$ are the sub indexes of the C's in B_k, for example $\text{Sub}(B_1) = \{4N, 8N, 12N\}$ and $C_{\text{Sub}(B_1)-2N} = \{C_{2N\pi}, C_{6N\pi}, C_{10N\pi}\}$. The dependence of B_k on the corresponding C's can be determined from the above recursion relation.

In order to get the individual $C_{i\pi}$'s, $D_k^{(\tilde{n})}(\lambda_j)$ must be calculated for three different λ_j's. Different choices of λ_j's have no effect on the extracted $C_{i\pi}$'s (we have confirmed this numerically). From the $D_k^{(\tilde{n})}(\lambda_j)$'s, the $C_{k\pi}$'s are extracted by solving the following equation, taking the block $[C_{4N\pi}, C_{8N\pi}, C_{12N\pi}]$ for example,

$$\begin{pmatrix} D_1^{(\tilde{n})}(\lambda_1) \\ D_1^{(\tilde{n})}(\lambda_2) \\ D_1^{(\tilde{n})}(\lambda_3) \end{pmatrix} = \begin{pmatrix} \lambda_1^{4N} & \lambda_1^{8N} & \lambda_1^{12N} \\ \lambda_2^{4N} & \lambda_2^{8N} & \lambda_2^{12N} \\ \lambda_3^{4N} & \lambda_3^{8N} & \lambda_3^{12N} \end{pmatrix} \cdot \begin{pmatrix} C_{4N\pi} \\ C_{8N\pi} \\ C_{12N\pi} \end{pmatrix}. \tag{3.11}$$

Inverting this matrix does not suffer from the numerical instabilities seen in the VMm, however as $12N$ becomes large, even computing the inverse of these 3×3 matrices requires high precision, since λ^{12N} can be out of double precision limit for very large N. Fig. 3.1 shows a comparison of the correlation functions computed from 2 sources by applying the Combination method and Improved Combination method to be discussed below. For the $N = 2$, $C_{1\pi}(t)$, $C_{9\pi}(t)$ and $C_{17\pi}(t)$ are computed simultaneously by inverting a 3 × 3 matrix, similarly for $(C_{2\pi}(t)$, $C_{10\pi}$, $C_{18\pi}(t))$, and $(C_{3\pi}(t)$, $C_{11\pi}(t)$, $C_{19\pi}(t))$. Because of the large magnitude difference between $C_{1\pi}$ $(C_{2\pi}$, $C_{3\pi})$ and $C_{17\pi}$ $(C_{18\pi}$, $C_{19\pi})$, which becomes smaller for $C_{4\pi}$ $(C_{5\pi}$, $\cdots)$ and $C_{20\pi}$ $(C_{21\pi}$, $\cdots)$, at 64 digit precision, $C_{1\pi}(t)$, $C_{2\pi}(t)$ and $C_{3\pi}(t)$ show signs of numerical break down at earlier time slices, which goes away at higher precision (100 digit), indicating that even calculating the inverse of the 3 × 3 matrix needs high precision to get the correct results.

As constructed, this method is only applicable to a 2^n source problem. In order to solve problems having an arbitrary number of sources, we extended this to an Improved Combination method in the next section.

3.4 Improved Combination method (ICm)

As there are $12N$ terms having λ in the expansion of $\det[1+\lambda A]$ for a $12N \times 12N$ matrix, Equation (3.2), the Combination method does not allow us to determine functions depending on less than 3 $C_{k\pi}$'s. A similar problem appears in the application of the FFT. In order to use FFT, 2^n data points are required. If the number of points in a series is not equal to 2^n, points with value zero must be appended to the original series to produce a series of length 2^n. Similarly, we can append additional $C_{k\pi}$'s to the expansion of $\det[1+\lambda A]$, as:

$$\det[1+\lambda A] = 1 + \lambda C_{1\pi} + \lambda^2 C_{2\pi} + \ldots + \lambda^{12N} C_{12N\pi} + \lambda^{12N+1} C_{(12N+1)\pi} + \ldots + \lambda^{2^m} C_{2^m\pi} \tag{3.12}$$

where $C_{p\pi} = 0$ for all $p > 12N$. The power m is chosen such that $2^{m-1} < 12N < 2^m$. With this new arrangement, exactly the same prescription discussed for the Combination Method can be applied, but in the last step the $D_k^{(\tilde{n})}(\lambda)$ individually

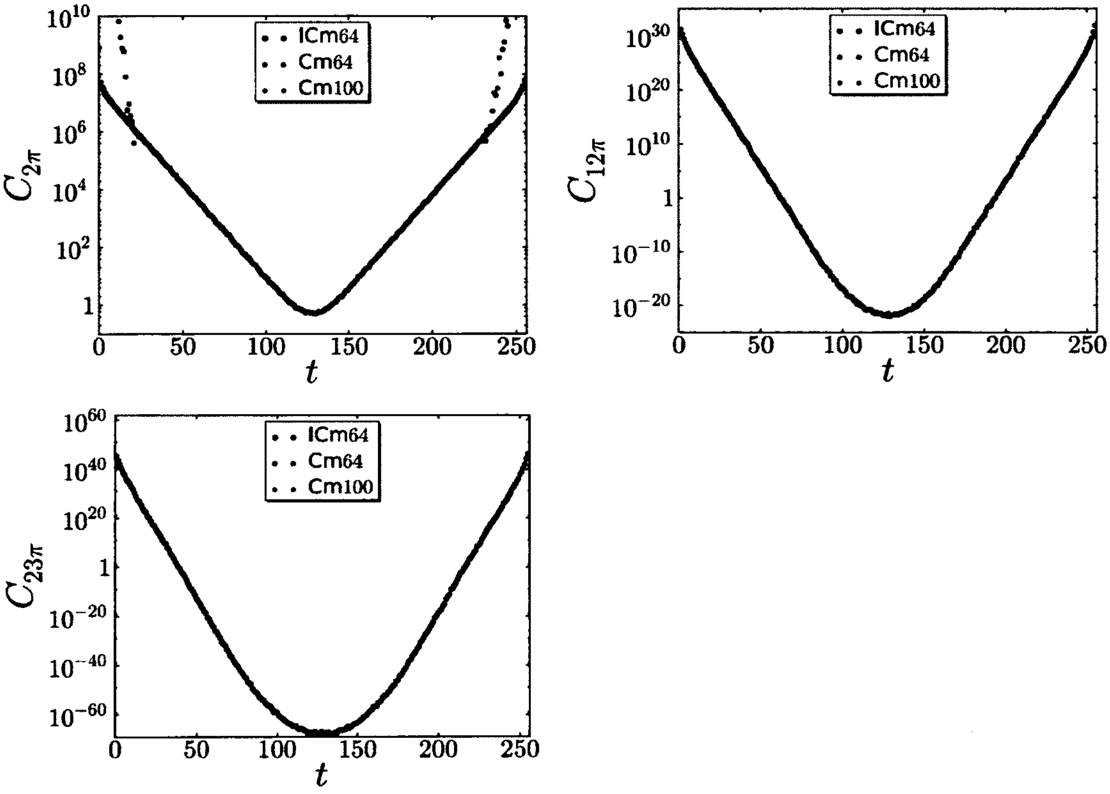

FIG. 3.1: $C_{2\pi}(t)$, $C_{12\pi}(t)$ and $C_{23\pi}(t)$ calculated from $N = 2$ sources by ICm with 64-decimal digital precision, denoted as ICm64, and Cm with 64(100)-decimal digital precision, denoted as Cm64(Cm100), on a single configuration are compared. Correlation functions from Cm100 agree with those from ICm64, however for the same precision, the ICm gives more accurate result than Cm. For $C_{2\pi}(t)$, Cm64 fails because of numerical inaccuracy as discussed in the text.

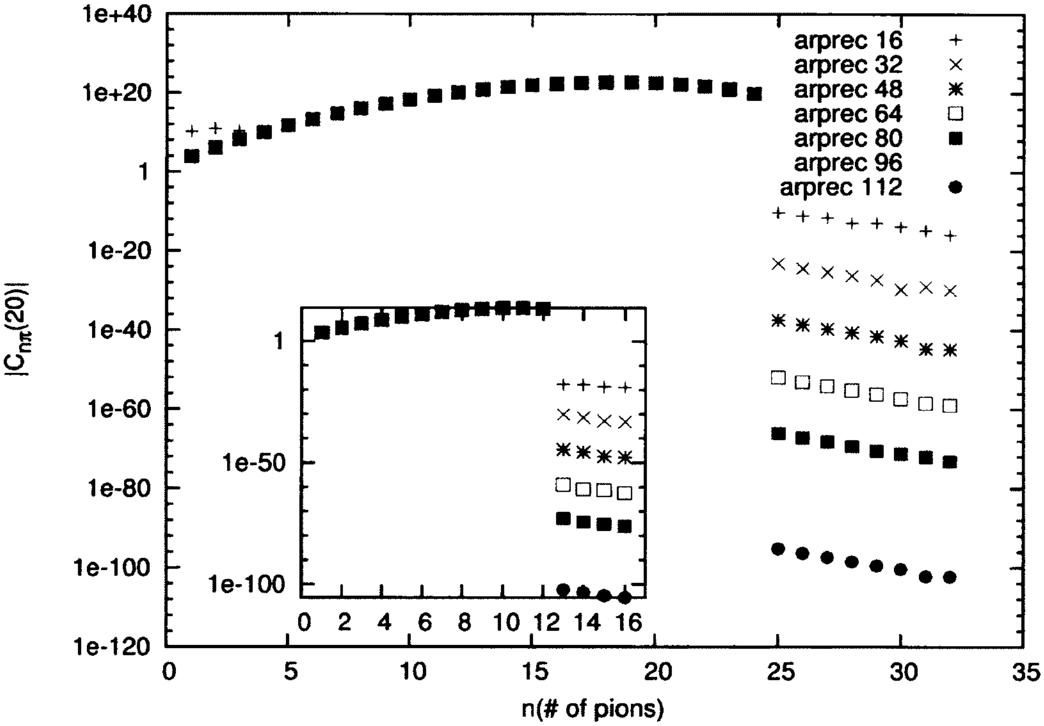

FIG. 3.2: Correlation functions on a single configuration at $t = 20$ from 2 sources computed with the Improved Combination method using the arprec library [8] at various precisions: 'arprec X' denotes that the calculation is done with X-decimal digit precision. The $C_{n\pi}(20)$ for $n = 1, 2, \ldots 24$ all agree for the different precision calculations just as they should, except for the calculation from 16-digit precision. However $C_{n\pi}(20)$ for $n = 25, 26, \ldots, 32$ are all machine zero at each precision. The disagreement of 16-digit precision indicates higher precision is needed. A similar comparison is shown for the single source correlation functions in the insert.

depends only on a single correlation function.

A significant advantage of this method compared with the Combinatin method is that no matrix inversion is required, so it is consequently less demanding in numerical precision, see Fig. 3.1, and in addition, problems with arbitrary numbers of sources can be solved with this method. Correlation functions appended to the series are solved for simultaneously with the other $C_{k\pi}$'s, providing a numerical check of the validity of this method. In Fig. 3.2, correlation functions calculated from 1-source and 2-sources on a single configuration are shown for different precision (we use the "arprec" library [8] to perform arbitrary precision calculations). As expected, all $C_{p\pi}$'s for $p > 12N$ are indeed numerically equivalent to zero, decreasing exponentially as the the numerical precision is increased. Since this method is more numerically stable than the Combination method, and can also solve problems of arbitrary number of sources, it is used in our further studies.

3.5 Generalization to 2 species from N sources

The methods discussed above can easily be generalized to two species of mesons by studying properties of the expansion of $\det[1 + \lambda_1 A + \lambda_2 B]$, where A and B are uncontracted correlation functions of two distinct species, for example π^+ and ρ^+. We can write

$$\det[1 + \lambda_1 A + \lambda_2 B] = 1 + \lambda_2^0 T_0 + \lambda_2^1 T_1 + \ldots + \lambda_2^k T_k + \ldots , \tag{3.13}$$

where

$$T_k(\lambda_1) = \lambda_1^0 C_{0A,kB} + \binom{k+1}{k} \lambda_1 C_{1A,kB} + \ldots + \binom{M}{k} \lambda_1^{M-k} C_{(M-k)A,kB}, \tag{3.14}$$

where $M = 12N$ is the dimension of the matrices A and B, and the correlation functions, $C_{mA,nB}$, are complicated combinations of correlation functions of a system having m-A's and n-B's distributed among different sources in all possible ways.

The $T_j(\lambda_1)$, for $j = 0, 1, \ldots, M$ for one λ_1 can be separated out by applying the methods discussed above with different choices of λ_2's, and then by applying the method again for different choices λ_1's for all $T_j(\lambda_1)$'s, the $C_{mA,nB}$'s can be separated out. This can be further generalized to correlators of arbitrary number of species as necessary.

3.6 Eigenvalue method [3]

All methods discussed above can be easily extended to study multi-species systems. If we are only interested in systems containing one species, we can explore the following relationship between determinant and eigenvalues to further speed up the computation of n-meson correlation functions.

$$\det[1 + \lambda A] = \prod_{i=1}^{12N}(1 + \lambda a_i) = \sum_{k=0}^{12N} C_k \lambda^k, \tag{3.15}$$

where a_i is the i^{th} eigenvalue of the matrix A. The C_k can be obtained by equating coefficients of λ^k one both sides. The main cost of the method is computing the eigenvalues of the matrix A, and it scales as $(12N)^3$. Thus the computational cost of this method is $\mathcal{O}(N^3)$.

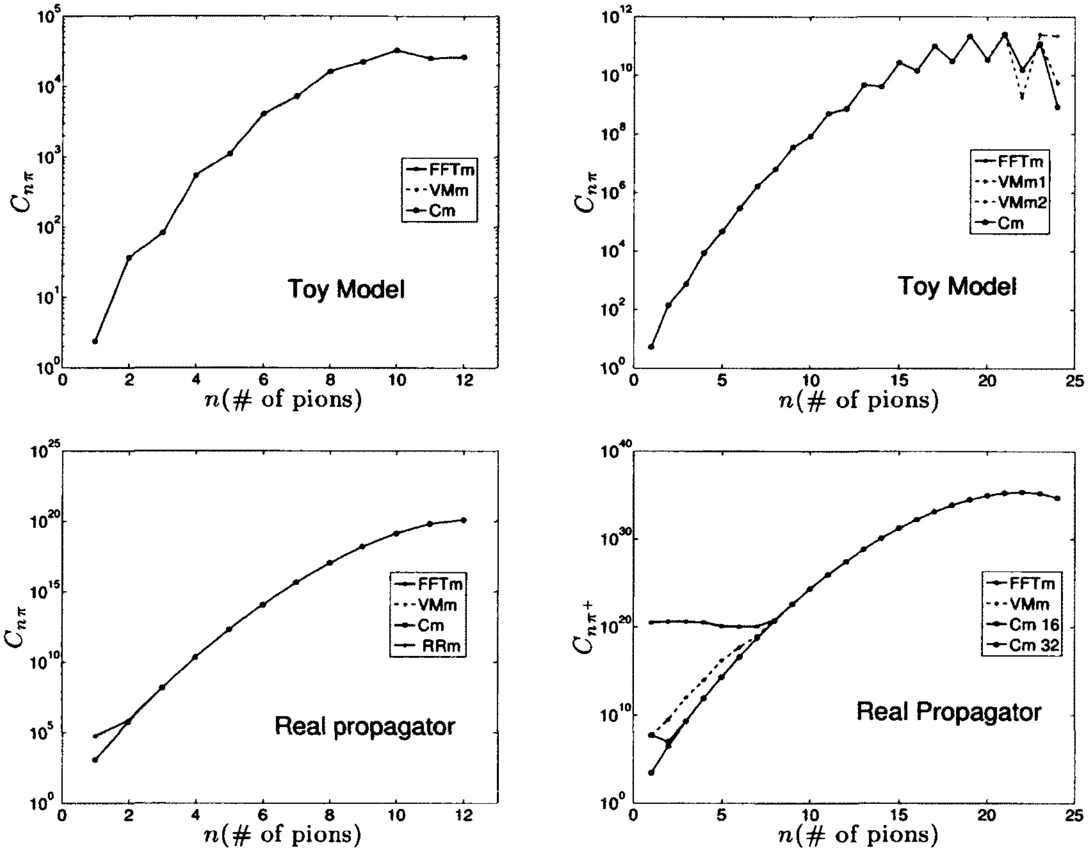

FIG. 3.3: The left panels compare 1-source calculations from the VMm, FFTm and Cm, and the right panels compare $C_{n\pi}$ calculated from 2 sources by the three methods. The real propagator is taken from one time slice, $t = 20$. The Recursion Relation method (RRm) [9] is also compared with other methods in the lower left plot as a check on the validity of the Cm. For the 2-source calculation in the toy model (top right) with VMm, two different sets of λ_ns have been used, denoted as VMm1 and VMm2. For VMm applied to the real propagator calculations, only one choice of λ's is shown. "Cm 16 (32)" denotes that calculation is done using Cm with 16(32) decimal digit precision.

3.7 Performance of different methods

In order to test the accuracy of different methods at a fixed precision, we compared correlation functions calculated from the VMm (implemented in MATLAB), the FFTm (implemented in MATLAB), and the Cm (implemented in C++ using the "arprec" high precision library [8]). We first considered a toy model with matrix elements $A_{n,m} = \sin((m-1)(n-1)+2) + i\cos(2(n-1))$ for 1 and 2 sources in the top half of Fig. 3.3. For this test, the λ's used in the VMm and Cm are randomly chosen between -0.25 and 0.25, however $C_{n\pi}(t)$ is shown to be independent of these choices. Results from VMm on 1-source agree with those from the FFTm and Cm for any set of λ. However for 2 sources, the FFTm and the Cm give the same results, but the VMm gives inconsistent results and changes with different choices of λ's, signaling a breakdown of the VMm and the requirement of higher precision. Similar tests have also been performed with the matrix elements $A_{n,m}$ extracted from real quark propagators and the results are shown in the lower half of Fig. 3.3. In this test, the Recursion Relation method (RRm) has also been used to compute the $C_{n\pi}$'s in order to validate the new methods. For the $N > 1$-source calculation no direct comparison with the RRm is made, since the $C_{\overline{n}\pi}$ computed from the new methods are complicated combinations of all $C_{n_1,\ldots,n_N}$'s with $\sum_{i=1}^{N} n_i = \overline{n}$. We verified however that the energies extracted for these correlators with either method, RRm and Cm, are in agreement. In contrast to the toy model, for the real $A_{n,m}$, the VMm gives more accurate results than the FFTm. However both tests show that the Cm gives the most accurate results for a fixed precision. Tests with real propagators on 2-source shows a break down of Cm on $C_{1\pi}$ and $C_{2\pi}$, however this breakdown can easily be corrected by working at higher precision.

The main purpose of constructing these new methods is to expedite the con-

---

[3] This method is suggested by Anyi Li [6]

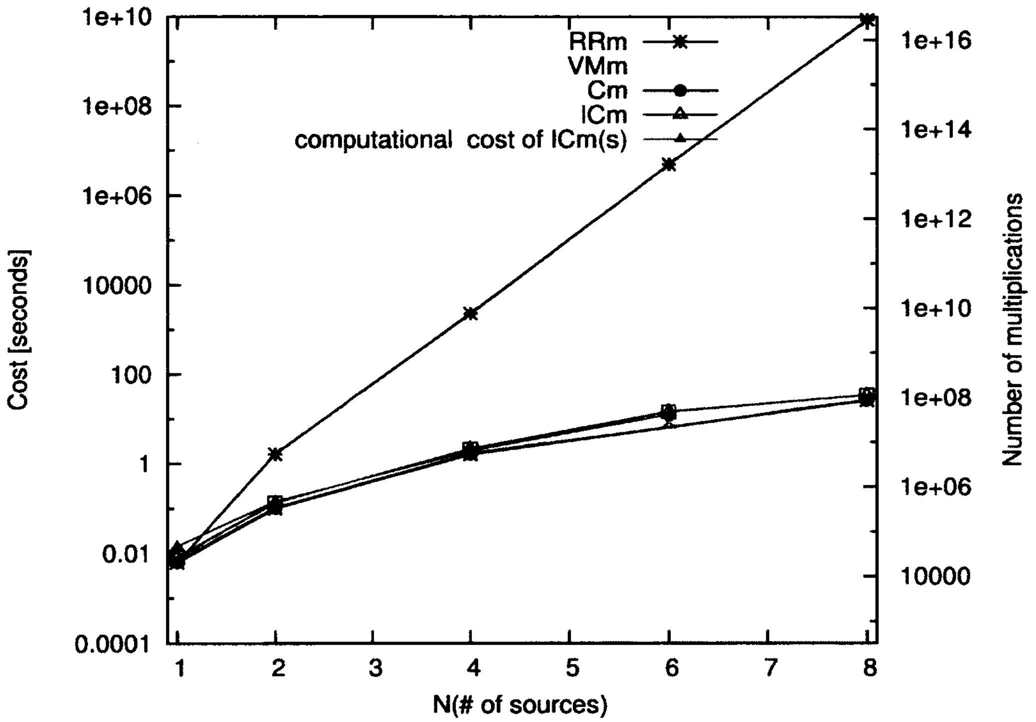

FIG. 3.4: Comparison of the number of multiplications required for each method (RH axis), and the corresponding expected computation time of $C_{n\pi}(t)$ for $n = 1, 2, \ldots 12N$ on a single time slice, corresponding to one application of the specified contraction method in seconds using a single 2.4 GHz Xeon core (LH axis). The computational cost of the ICm is taken from the actual running time, and it is used to normalize the time scale so that the projected running time of other methods can be read out from the LH axis.

TABLE 3.1: Scaling of different methods in terms of number of multiplications for an N source calculation.

	scaling
RRm	$12^4 N^4 \exp(2.8(N-1))$
VMm	$(12N+2)(12N)^3$
Cm	$3 \cdot 2^{\log 2(4N)}(12N)^3$
ICm	$2^{\text{floor}(\log_2(12N))+2}(12N)^3$

tractions required in computing correlation functions for systems comprised of large number of mesons. The numerical scaling of the Recursion Relation method, Vandermonde Matrix method, Combination method and Improved Combination method (the FFT method costs the same amount of time as the ICm if f_0, τ and T are chosen appropriately) are compared in Table 3.1. For each method, we determine how many multiplications are required. From Ref. [9], the computational cost of the recursion relation method is proportional to $12^4 N^4 \exp(2.8(N-1))$, where N is the number of sources. The VMm requires a calculation of $12N$ determinants, one inversion of $12N \times 12N$ matrix and the multiplication of a $12N \times 12N$ matrix and $12N \times 1$ vector. The dominant contribution to the computational cost of the other two methods comes from calculating a large number of determinants. For the Improved Combination method, a step-n calculation requires the computation of 2^n determinants, while the Combination method requires $3 \cdot 2^n$ for a step-n calculation. To solve an N-source problem, the Combination method requires $\log 2(4N)$ steps for $N = 2^m$, where m is an integer, and the Improved Combination method requires $\text{floor}(\log_2(12N)) + 2$ steps. Taking account of all the determinant calculations that are needed, and the computational cost of each determinant ($\sim (12N)^3$ using LU decomposition), the numerical cost of each method is tabulated in Table. 3.1, and compared in Fig. 3.4. Although the recursion relation method significantly reduces the cost of contractions over the original $(12N!)^2$ scaling, the computational cost of the recursion relation method is much larger than other methods, all of which scale similarly. Using the ICm, we turn to numerical investigations of systems of large number of mesons in the next chapter.

CHAPTER 4

QCD at Finite Isospin Density

4.1 Lattice details

In this Chapter, we apply improved multi-meson methods constructed in Chapter (3), and study systems containing up to 72 pions. Calculations in this chapter are performed on ensembles of anisotropic gauge field configurations with clover-improved fermions [14] that have been generated by the Hadron Spectrum Collaboration and the Nuclear Physics with Lattice QCD collaboration. The gauge action is a tree-level tadpole-improved Symanzik-improved action, and the fermion action [28, 29] is a $n_f = 2 + 1$ anisotropic clover action [30] with two levels of stout smearing [24] with weight $\rho = 0.14$ only in spatial directions (see [15] for more details). In order to preserve the ultra-locality of the action in the temporal direction, no smearing is applied in that direction. Furthermore, the tree-level tadpole-improved Symanzik gauge action without a 1×2 rectangle in the time direction is used.

Four ensembles of gauge fields are used in this study with volumes $L^3 \times T$ of $\{16^3 \times 128$, $20^3 \times 128$, $24^3 \times 128$ and $20^3 \times 256\}$, and with a renormalized anisotropy

TABLE 4.1: Details of the four gauge ensembles with the same lattice space $a = 0.1227 \pm 0.0008$ fm used in this chapter. N_{cfg} denotes the number of configurations used in the current calculation. In the last two columns, N_{src} is the number of source times used on each configuration and N_{mom} is the number of momentum sources used for each source time.

	$L^3 \times T$ (a^{-1})	L (fm)	$m_\pi L$	$m_\pi T$	N_{cfg}	N_{src}	N_{mom}
B1	$16^3 \times 128$	2.0	3.9	8.8	180	8	33
B2	$20^3 \times 128$	2.5	4.8	8.8	51	8	19
B3	$24^3 \times 128$	3.0	5.8	8.8	98	8	19
B4	$20^3 \times 256$	2.5	4.8	17.6	147	16	7

$\xi = a_s/a_t = 3.5$, where a_s (a_t) is the spatial (temporal) lattice spacing. The lattice spacing is the same for each ensemble, $a_s = 0.1227 \pm 0.0008$ fm [15], which gives spatial extents $L \sim 2.0, 2.5, 3.0$ fm for $L = 16, 20, 24$ respectively. The same bare inputs of light quark mass $a_t m_l = -0.0840$ and strange quark mass $a_t m_s = -0.0743$ are used in generating each ensemble, giving a pion mass of $m_\pi \sim 390$ MeV and a kaon mass of $m_K \sim 540$ MeV. The quantities $m_\pi L$ and $m_\pi T$, which determine the impact of the finite volume and temporal extent, are $m_\pi L \sim 3.86, 4.82, 5.79$ for $L = 16, 20, 24$ lattices and $m_\pi T \sim 8.82, 17.64$ for $T = 128, 256$, respectively. Details of the four ensembles are summarized in Table 4.1.

In our work, a momentum space representation of the contractions is used and quark propagators in time-momentum space, which we refer to as "colorwave propagators", $S_{u/d}(\mathbf{p}, \tau; \mathbf{p}', 0)$, are calculated on Coulomb gauge fixed configurations[1]. Details about how to compute colorwave propagators are discussed in Section. 2.3.

A correlation function of one pion with momentum $\mathbf{p}_f$ can be constructed by

---

[1] As we compute gauge invariant quantities, our results are independent of the gauge fixing procedure.

projecting both sink and source to the same momentum $\mathbf{p}_f$ as:

$$\begin{aligned} C_{1\pi}(\mathbf{p}_f, t) &= \left\langle \sum_{\mathbf{x}.\mathbf{x}'} e^{-i(\mathbf{p}_1\mathbf{x}-\mathbf{p}_2\mathbf{x}')}\overline{d}(\mathbf{x}', t)\gamma_5\; u(\mathbf{x}, t) \sum_{\mathbf{y}\mathbf{y}'} e^{i\mathbf{p}\mathbf{y}} e^{-i(\mathbf{p}-\mathbf{p}_f)\mathbf{y}'}\; \overline{u}(\mathbf{y}, 0)\gamma_5 d(\mathbf{y}', 0) \right\rangle \\ &= \sum_{\mathbf{x},\mathbf{x}',\mathbf{y},\mathbf{y}'} \left\langle e^{-i\mathbf{p}_1\mathbf{x}} e^{i\mathbf{p}\mathbf{y}}\; \gamma_5 S_u(\mathbf{x}, t; \mathbf{y}, 0)\; \gamma_5 e^{i\mathbf{p}_2\mathbf{x}'}\;\; e^{-i(\mathbf{p}-\mathbf{p}_f)\mathbf{y}'}\; (\gamma_5 S_d^\dagger(\mathbf{x}', t; \mathbf{y}', 0)\gamma_5) \right\rangle \\ &= \left\langle \sum_{\mathbf{x},\mathbf{y}} \gamma_5 (e^{-i\mathbf{p}_1\mathbf{x}} e^{i\mathbf{p}\mathbf{y}} S_u(\mathbf{x}, t; \mathbf{y}, 0)) \sum_{\mathbf{x}',\mathbf{y}'} e^{-i(\mathbf{p}-\mathbf{p}_f)\mathbf{y}'} e^{i\mathbf{p}_2\mathbf{x}'} \gamma_5 (\gamma_5 S_d^\dagger(\mathbf{x}', t; \mathbf{y}', 0)\gamma_5) \right\rangle \\ &= \left\langle \gamma_5 S_u(\mathbf{p}_1, t; \mathbf{p}, 0) \cdot \gamma_5 (\gamma_5 S_d^\dagger(-\mathbf{p}_2, t; \mathbf{p}_f - \mathbf{p}, 0)\gamma_5) \right\rangle, \end{aligned} \tag{4.1}$$

where $\mathbf{p}_1 - \mathbf{p}_2 = \mathbf{p}_f$. Each choice of $\{\mathbf{p}_1, \mathbf{p}_2\}$ and $\mathbf{p}$ satisfying momentum conservation is a separate correlation function with distinct creation and annihilation interpolating fields, and we have suppressed the dependence of $C_{1\pi}$ on $\mathbf{p}_1$, $\mathbf{p}_2$ and $\mathbf{p}$. During the calculation, we held $\mathbf{p}_1$, $\mathbf{p}_2$ and $\mathbf{p}_f$ fixed and summed over all $\mathbf{p}$'s for which we have computed colorwave propagators (see Table. 4.1) in order to get more statistics. In the second step, the definition of propagator $S_{u/d}(\mathbf{x}', t; \mathbf{y}, 0)$ and the γ_5 hermiticity of the propagator is used. The definition of the colorwave propagator, Eq. (2.16), is applied in the last step.

The correlation functions of a system having n π^+'s in a single source, with total momentum $\mathbf{P}_f = n\ \mathbf{p}_f$ can be constructed similarly:

$$\begin{aligned} C_{n\pi}(t, \mathbf{P}_f) &= \left\langle \left(\sum_{\mathbf{x},\mathbf{x}'} e^{-i(\mathbf{p}_1\mathbf{x}-\mathbf{p}_2\mathbf{x}')}\overline{d}(\mathbf{x}', t)\gamma_5 u(\mathbf{x}, t) \right)^n \right. \\ &\quad \left. \cdot \left(\sum_{\mathbf{y},\mathbf{y}'} e^{i\mathbf{p}\mathbf{y}} e^{-i(\mathbf{p}-\mathbf{p}_f)\mathbf{y}'} \overline{u}(\mathbf{y}, 0)\gamma_5 d(\mathbf{y}', 0) \right)^n \right\rangle, \end{aligned} \tag{4.2}$$

where the dependence of $C_{n\pi}$ on $\mathbf{p}_1$, $\mathbf{p}_2$ and $\mathbf{p}$ has also been suppressed in Eq. (4.2).

Because of the Pauli exclusion principle, systems constructed from a single source in momentum space can only reach a maximum of 12 π^+'s. In order to put more pions into a system, additional sources are required. Correlation functions of a N-source system having $\overline{n} = \sum_{i=1}^{N} n_i \pi^+$'s with total momentum $\mathbf{P}_f = \sum_{i=1}^{\overline{n}} \mathbf{p}_{f_i}$ are given by

$$\begin{aligned} C_{n_1\pi,\ldots,n_N\pi}(t, \mathbf{P}_f) &= \left\langle \prod_{i=1}^{N} \left(\sum_{\mathbf{x}_i, \mathbf{x}'_i} e^{-i(\mathbf{p}_1^i \mathbf{x}_i - \mathbf{p}_2^i \mathbf{x}'_i)} \overline{d}(\mathbf{x}'_i, t) \gamma_5 u(\mathbf{x}_i, t) \right)^{n_i} \right. \\ &\quad \times \left. \prod_{j=1}^{\overline{n}} \left(\sum_{\mathbf{y}_j, \mathbf{y}'_j} e^{i\mathbf{p}_j \mathbf{y}_j} e^{-i(\mathbf{p}_j - \mathbf{p}_{f_j})\mathbf{y}'_j} \overline{u}(\mathbf{y}_j, 0) \gamma_5 d(\mathbf{y}'_j, 0) \right) \right\rangle, \end{aligned} \quad (4.3)$$

where n_i is the number of pions in the i^{th} source, and momentum conservation $\sum_{i=1}^{N} n_i (\mathbf{p}_1^i - \mathbf{p}_2^i) = \sum_{j=1}^{\overline{n}} \mathbf{p}_{f_j}$, must be satisfied in order for the correlation functions to be non-vanishing. Here, only systems with total zero momentum, $\mathbf{P}_f = (0, 0, 0)$, are investigated, and $\mathbf{p}_{f_j}$'s for each source are also fixed to $\mathbf{p}_{f_j} = (0, 0, 0)^2$. The improved multi-meson methods constructed in the last chapter apply equally well in momentum space and are used in our work. The uncontracted correlation functions in momentum space are calculated according to Equation (2.20).

For the $T = 128$ (256) ensembles, 8 (16) colorwave propagators are generated on each configuration located 16 time slices apart to minimize correlations between propagators. For ensembles $\{B1, B2, B3, B4\}$, $\{180, 51, 147, 98\}$ configurations and $\{33, 19, 19, 7\}$ momenta are used respectively. In order to reduce contamination from thermal states, a temporal extent of $T = 256$ is desirable for systems of large numbers of pions. On the B1 and B3 ensembles, the $A \pm P$ (antiperiodic ± periodic propagator) method [31, 32, 33] is applied to effectively double the temporal extent, see Appendix A. The validity of this method is investigated by comparing results from ensemble B4 ($20^3 \times 256$) and with those from ensemble B2 ($20^3 \times 128$) with the $A \pm P$ method and it is found to be sound at the precision we achieve for the

---

[2] Using non-zero momentum sources, for example $\mathbf{p}_{f_1} = (0, 0, -1)$ and $\mathbf{p}_{f_2} = (0, 0, 1)$, to construct a zero momentum system has also been investigated, and we find that higher momenta sources have smaller contribution to the correlation function of a system at rest than zero momentum sources. Technically, different weights can be chosen in Eq. (4.3) for each combination of $\mathbf{p}_{f_i}$ to get better overlap to the ground state.

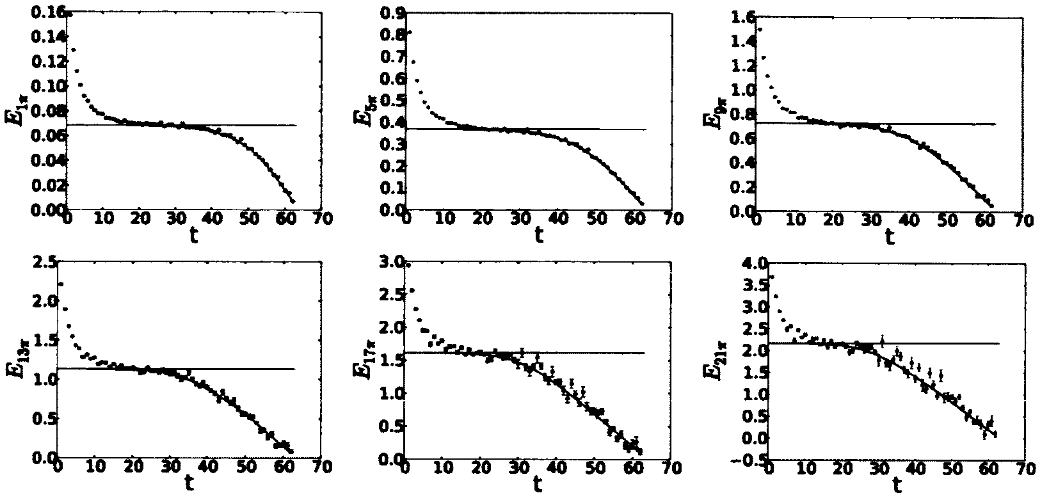

FIG. 4.1: The black data is the effective mass calculated from the original data from ensemble B2, and blue line through the data points is reconstructed from the ground state energies extracted from the ensemble B4 as discussed in the main text. The red straight line is the fitted value of $E_{n\pi}$ extracted from the correlators of ensemble B4.

systems under consideration as discussed below.

4.2 Ground state energies

Previous studies of the energies and isospin chemical potentials [34, 4] on ensemble B2 showed that thermal states contribute significantly to correlation functions and, even for $C_{12\pi}(t)$, the ground state does not dominate in any region of Euclidean time. The expected form of correlation functions of an n-π^+ system with temporal extent T is expressed in Equation (2.21).

For the $T = 128$ B2 ensemble, effective mass plots are shown in Fig. 4.1 for various n, and it is clear that correlation functions receive significant contributions from thermal states. Their analysis requires a fit including all thermal states, Eq. (2.21), in order to extract the ground state energy. Since the number of free parameters in the fit grows with n, the systematic uncertainty of $E_{n\pi}$ becomes large and we are unable to extract any accurate information at large n. In order to minimize contributions from thermal states, a longer temporal extent is required.

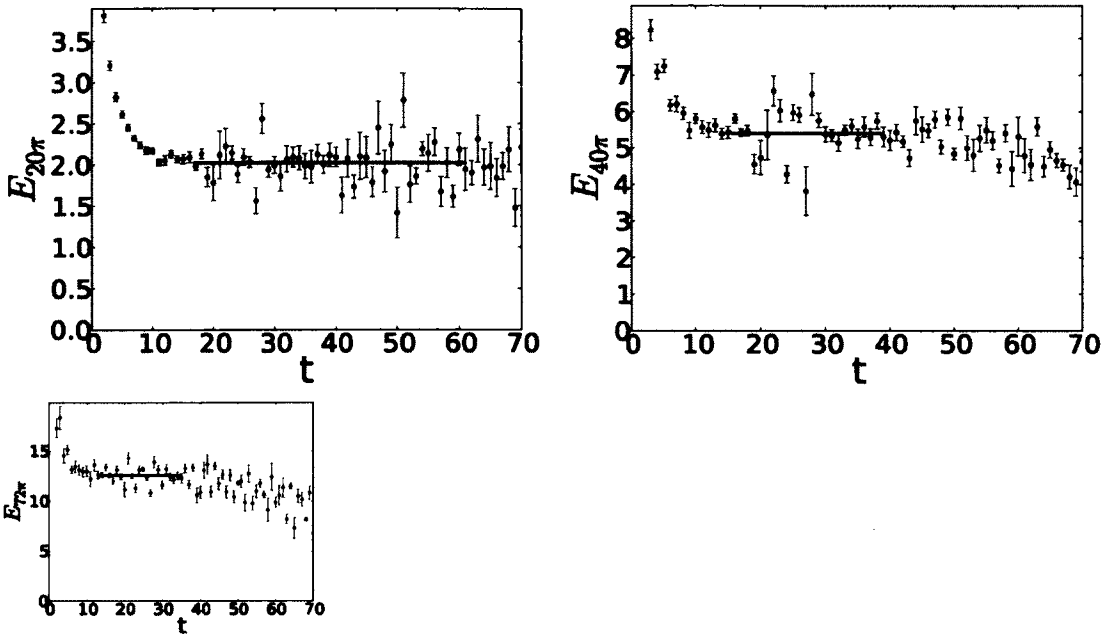

FIG. 4.2: The effective mass of $C_{20\pi}(t)$ from the 2-source calculation on the ensemble B4 is shown on the left along with the extracted ground state energy represented as a black band. Similarly, the effective mass of $C_{40\pi}(t)$ ($C_{72\pi}(t)$) from the 4 (6) source calculation on the same ensemble and the corresponding extracted ground state energy is shown in the middle (on the right).

Thermal effects are exponentially suppressed by the larger temporal extent and the ensemble with $T = 256$ has greatly reduced contamination, and a simple single exponential fit at intermediate times is sufficient to extract ground state energies, even for $E_{72\pi}$, as shown in Fig. 4.2. Effective mass plots of $C_{20\pi}$, $C_{40\pi}$ and $C_{72\pi}$ for this ensemble all show a plateau region, and a single exponential fit, only including the term in Eq. (2.21) with $m = 0$, is enough to extract the ground state energy $E_{n\pi}$. However, for significantly larger numbers of pions, a still larger temporal extents would again be necessary.

4.3 Energies from $20^3 \times 256$ ensemble

Correlation functions, defined in Eq. (4.3), for systems with the quantum numbers of up to 72 π^+'s have been computed on the B4 ensemble. In this chapter, only systems having zero center of mass momentum are investigated. For a discussion of results for different total momenta, see Ref [4]. Because of precision issues, we have computed correlation functions from 2, 4, and 6 sources, from which $E_{1\pi\rightarrow 24\pi}$, $E_{25\pi\rightarrow 48\pi}$ and $E_{49\pi\rightarrow 72\pi}$ have been extracted respectively, where $E_{n\pi}$ is the ground state energy of a n-π^+ system at rest. Fig. 4.3 shows $C_{20\pi}(t)$, $C_{40\pi}(t)$ and $C_{70\pi}(t)$ from 6-source contractions. The breakdown at earlier time slices of $C_{20\pi}(t)$ indicates that computations with higher precision are required in order to use 6 sources. Computations with arbitrary precisions are accessible with the "arprec" library [8], however at the same precision, they are $\sim$ 5 times more expensive than with the fixed quad-double precision (implemented using the "qd" library [35]). In our main studies, we perform all contractions in quad-double precision, and multiply the uncontracted propagators by a prefactor before performing the contractions such that the particular $C_{n\pi}(t)$'s that we focus on do not suffer from the limit of the floating point dynamical range of quad-double precision (this prefactor is removed at the end of the calculation).

As the correlation functions of systems containing many pions span a large numerical range, $10^{250} \sim 10^{-250}$ for $C_{70\pi}(t)$ for example, inverting the correlation matrix during a correlated fit brings in significant instabilities, thus $E_{n\pi}$ for $n = 1, 2, \ldots 72$ are extracted from uncorrelated fits in this study. The fitting window is chosen between time slices where a clear plateau region of the effective mass plot can be seen. Statistical uncertainties are constructed from fits to multiple bootstrap resamplings of the ensemble (we use $N_s = 88$ samples), and systematic uncertainties are estimated by shifting the fitting window forward and backward two time slices.

Since the ground state energy of a system containing many pions becomes large, even fitting correlation functions with only one exponential becomes problematic because of precision. Taking the 25-π^+ system for example, the ground state energy of this system is $E_{25\pi} = 2.76$ in temporal lattice units, and the fit is performed

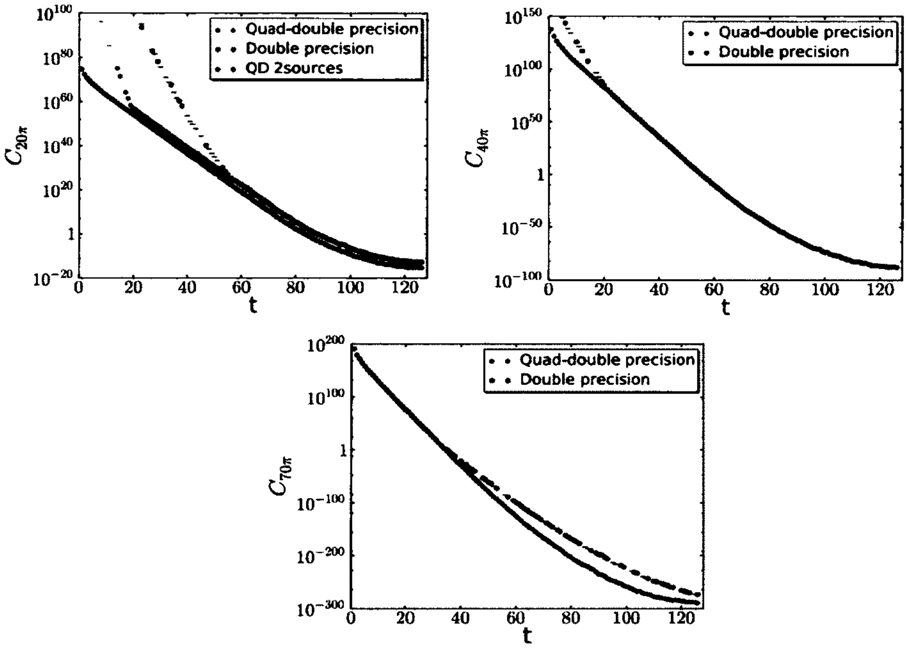

FIG. 4.3: The correlation functions, $C_{20\pi}(t)$, $C_{40\pi}(t)$ and $C_{70\pi}(t)$, calculated from 6-sources with quad-double precision and double precision are compared in the left, center, and right plots respectively. The same calculations done with double precision shows even more severely breakdown, indicating that high precision is needed in order to study many pion systems. Although $C_{20\pi}$ from 6-sources with quad-double precision breaks down at earlier time slices, the rescaled $C_{20\pi}$ from 2-source computations, which is shown also in the left plot, is free from precision issues and is used in extracting the $E_{20\pi}$.

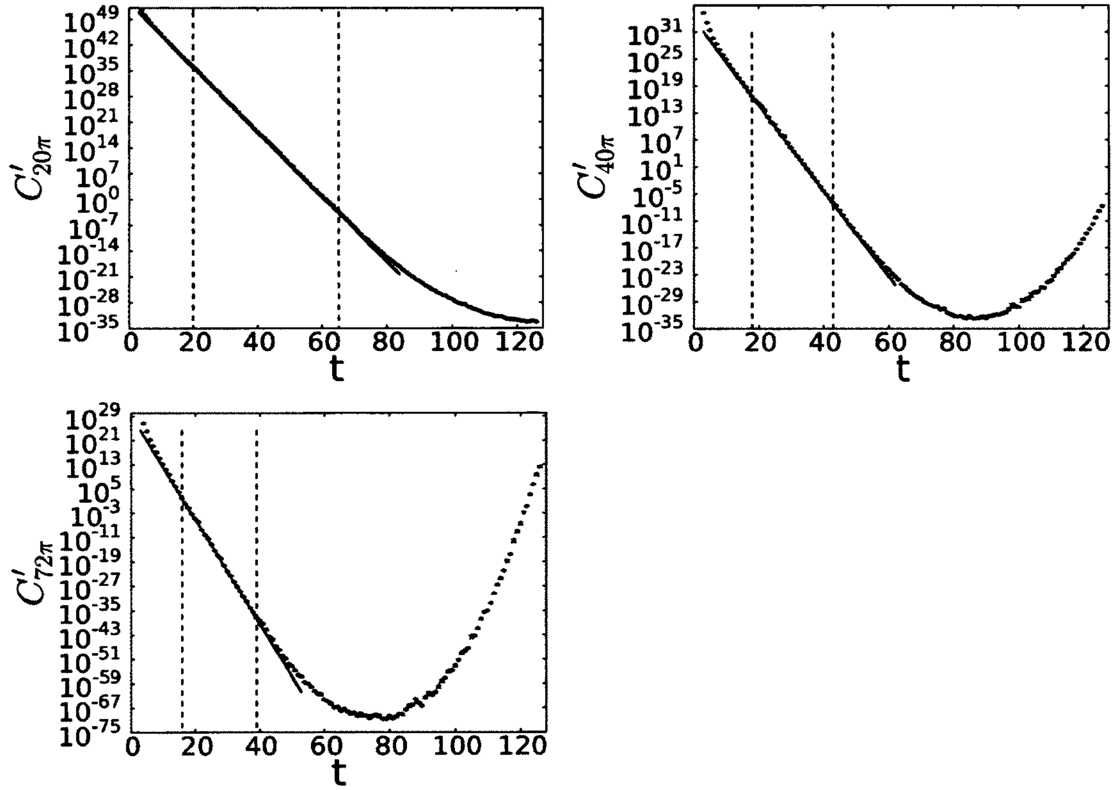

FIG. 4.4: $C'_{20\pi}(t)$ is shown on the left, where the blue points are data, the red line is constructed from the fit, and two vertical dashed lines indicate the fitting window. Similar plots of preconditioned $C'_{40\pi}(t)$ and $C'_{72\pi}(t)$ are also shown.

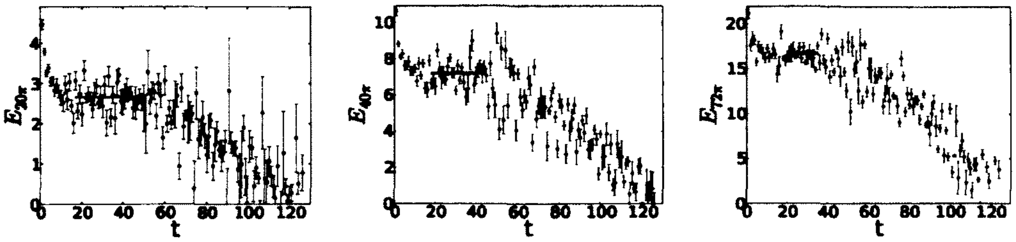

FIG. 4.5: Effective mass plots with $A \pm P$ method on ensemble B1 are shown here. The effective mass of $C_{20\pi}(t)$ from the 2-source calculation is shown on the left along with the ground state energy represented as a black band. Similarly effective mass plots of $C_{40\pi}$ from 4-sources and $C_{72\pi}(t)$ from 6-sources calculations and the extracted ground state energies are shown in the middle and right respectively.

between $t/a_t = [15, 58] \pm 2$. The correlation function varies over 140 orders of magnitude from $t = 15$ to $t = 58$. Such a large change in magnitude requires care with precision and in order to ameliorate this problem, instead of fitting correlation functions directly, we fit the following preconditioned correlation functions:

$$C'_{n\pi}(t) = Z'_n \exp(\delta E_n t) C_{n\pi}(t), \tag{4.4}$$

where $C_{n\pi}(t)$ is the original correlation function, and Z'_n, and δE_n are fixed numbers, chosen so that $C'_{n\pi}(t)$ changes less dramatically inside the fitting window. Since the original correlation function behaves like a single exponential inside the plateau region where the ground state dominates, multiplying another exponential will not change this feature. Furthermore, the extracted ground state energy should have no dependence on Z'_n and δE_n, which is numerically confirmed. The preconditioned correlation functions and the corresponding single exponential fits for $n = 20, 40$ and 72 are shown in Fig. 4.4.

4.4 Energies from $16^3 \times 128$ and $24^3 \times 128$ ensembles

As the $A \pm P$ method has been validated on the B2 ensemble see, systems having up to 72 π^+'s has also been studied on ensembles B1 and B3 using this

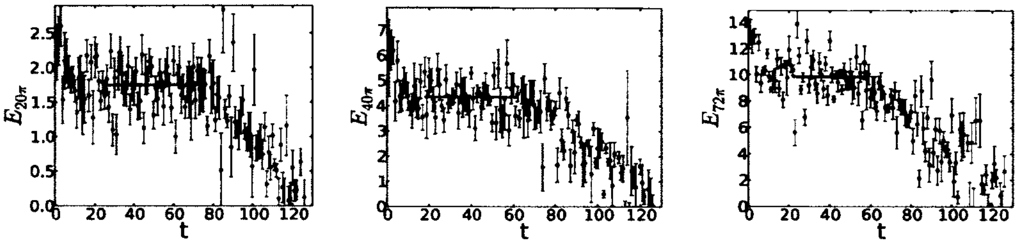

FIG. 4.6: Effective mass plots with $A \pm P$ method on ensemble B3 are shown.

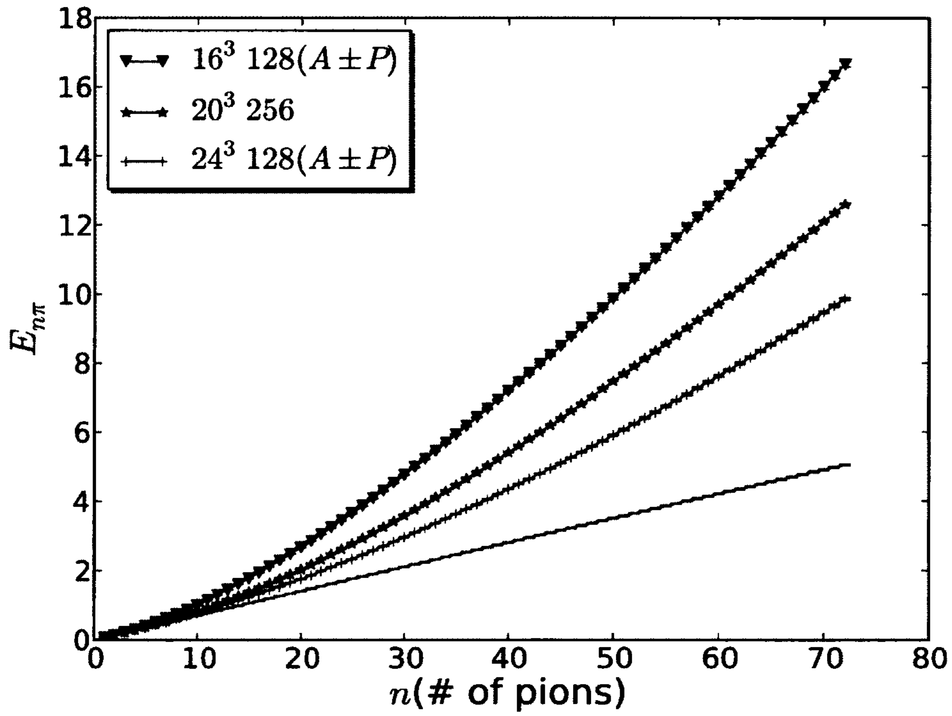

FIG. 4.7: The ground state energies of a system of n-π^+ ($E_{n\pi}$) extracted from ensembles B1 (red), B3 (blue) and B4 (green) are shown. The black line represents the total energy of n non-interacting pions.

method. Effective mass plots with extracted ground state energies from ensemble B1 are shown in Fig. 4.5 and those from ensemble B3 are shown in Fig. 4.6. All calculations are done with the ICm, and ground state energies are extracted with the same statistical method as those in the Section 4.3. The extracted ground state energies from all three volumes are shown in Fig. 4.7.

4.5 Interaction parameters

By considering the energy shifts of two particle states in a finite volume, $\Delta E \equiv E_2 - 2E_1 = 2\sqrt{\mathbf{p}^2 + E_1^2} - 2E_1$ and $E_1 = m_\pi$ here, Lüscher derived a relationship between the phase shift, $\delta(p)$, and the interacting momentum, $p = |\mathbf{p}|$, given by [36, 37] (see also [38]),

$$p \cot \delta(p) \;=\; \frac{1}{\pi L}\,\mathbf{S}\left(\left(\frac{pL}{2\pi}\right)^2\right) \quad , \tag{4.5}$$

which is valid for momenta below the inelastic threshold. The regulated three-dimensional sum, $\mathbf{S}(x)$, is

$$\mathbf{S}\,(\,x\,) \;\equiv \lim^{\Lambda\to\infty} \left(\sum_{\mathbf{j}}^{|\mathbf{j}|<\Lambda} \frac{1}{|\mathbf{j}|^2 - x} \;-\; 4\pi\Lambda \right) \quad , \tag{4.6}$$

where the summation is over all triplets of integers $\mathbf{j}$ such that $|\mathbf{j}| < \Lambda$.

By performing an expansion in small $1/L$, the energy shift of n identical bosons in a finite volume, $\Delta E_n = E_n - nE_1$, has also been studied up to $\mathcal{O}(L^{-7})$ in recent work [39, 40, 41, 42]. The resulting shift of energies due to both two-body and three-body interactions is given by [41]:

$$\begin{aligned}
\Delta E_n \; = \; & \frac{4\pi\,\bar{a}}{M\,L^3}\,{}^nC_2\Bigg\{1-\left(\frac{\bar{a}}{\pi\,L}\right)\mathcal{I}+\left(\frac{\bar{a}}{\pi\,L}\right)^2\left[\mathcal{I}^2+(2n-5)\mathcal{J}\right] \\
& \quad -\left(\frac{\bar{a}}{\pi\,L}\right)^3\left[\mathcal{I}^3+(2n-7)\mathcal{I}\mathcal{J}+\left(5n^2-41n+63\right)\mathcal{K}\right] \\
& \quad +\left(\frac{\bar{a}}{\pi\,L}\right)^4\Big[\mathcal{I}^4-6\mathcal{I}^2\mathcal{J}+(4+n-n^2)\mathcal{J}^2+4(27-15n+n^2)\mathcal{I}\,\mathcal{K} \\
& \qquad +(14n^3-227n^2+919n-1043)\mathcal{L}\,\Big]\Bigg\} \\
& + {}^nC_3\left[\frac{192\,\bar{a}^5}{M\pi^3L^7}\left(\mathcal{T}_0\;+\;\mathcal{T}_1\,n\right)\;+\;\frac{6\pi\bar{a}^3}{M^3L^7}\,(n+3)\,\mathcal{I}\right] \\
& + {}^nC_3\,\frac{1}{L^6}\,\bar{\eta}_3^L\;+\;\mathcal{O}\left(L^{-8}\right)\quad , \qquad (4.7)
\end{aligned}$$

where ${}^mC_n = m!/(n!(m-n)!)$, and the parameter $\bar{a}$ is the inverse phase shift at the binding momentum of the two body system (below we will refer to this as the effective scattering length). This is related to the scattering length, a, and the effective range, r, by

$$a \;=\; \bar{a}\;-\;\frac{2\pi}{L^3}\bar{a}^3r\left(1\;-\;\left(\frac{\bar{a}}{\pi L}\right)\mathcal{I}\right)\;, \qquad (4.8)$$

where a and r are parameters in the effective range expansion

$$p\cot\delta = -\frac{1}{a}+\frac{r}{2}p^2+\mathcal{O}(p^4). \qquad (4.9)$$

The geometric constants entering Eq. (4.7) are:

$$\begin{aligned}
\mathcal{I} &= -8.9136329\,, & \mathcal{J} &= 16.532316\,, & \mathcal{K} &= 8.4019240\,, \\
\mathcal{L} &= 6.9458079\,, & \mathcal{T}_0 &= -4116.2338\,, & \mathcal{T}_1 &= 450.6392\,. \qquad (4.10)
\end{aligned}$$

The three body parameter $\overline{\overline{\eta}}_3^L$ is constructed from the volume dependent but renormalization group invariant three body interaction parameter, $\overline{\eta}_3^L$, the inverse phase shift, $\overline{a}$, and the effective range, r, as

$$\overline{\overline{\eta}}_3^L \;=\; \overline{\eta}_3^L \left(1 \;-\; 6 \left(\frac{\overline{a}}{\pi L} \right) \mathcal{I} \right) \;+\; \frac{72\pi \overline{a}^4 r}{ML} \, \mathcal{I} \quad , \tag{4.11}$$

where

$$\overline{\eta}_3^L = \eta_3(\mu) \;+\; \frac{64\pi a^4}{M} \left(3\sqrt{3} - 4\pi \right) \; \log\left(\mu L\right) \;-\; \frac{96 a^4}{\pi^2 M} \mathcal{S}_{\mathrm{MS}} \quad . \tag{4.12}$$

and the renormalized scale dependent coupling $\eta_3(\mu)$ is responsible for the three-body interactions. The renormalization scheme dependent quantity $\mathcal{S}$ defined in the Minimal Subtraction scheme is given by $\mathcal{S}_{\mathrm{MS}} = -185.12506$.

4.6 Two-body interactions from Lüscher's method

From the energy difference in the 2-π^+ system, $\Delta E_{2\pi} = E_{2\pi} - 2m_\pi$, the relative momentum of each π^+, $\mathbf{p}$, in the center of mass frame (COM) can be calculated from the dispersion relation. We determine the effective scattering length[3], $\overline{a}$, by calculating the interacting momenta $\{\mathbf{p}_i\}$, on each bootstrap ensemble and applying Eq. (4.5), and we average over all ensembles to get the mean value of $\overline{a}$, and the statistical uncertainty. The systematic uncertainty is determined by averaging the systematic uncertainty of $\overline{a}$ on each bootstrap ensemble resulting from the systematic uncertainty of the extracted energies from the choice of different fitting intervals. The extracted effective scattering length for each volume is shown in Table 4.2. Our results are in agreement with the extractions in Ref. [10] from two-body systems

---

[3] As discussed above, $\bar{a}$ is the inverse phase shift at the binding momentum of the two body system, and the scattering length in Eq. (4.5) uses the Particle Physics sign convention, and it is negative for repulsive interactions.

studied on the same ensembles.

TABLE 4.2: The effective scattering length ($\overline{a}$) from Lüscher's method. The first uncertainty is statistical uncertainty and the second uncertainty is systematic.

$V^3 \times T$	p^2/m_π^2	$\overline{a}$(fm)	$m_\pi \overline{a}$
$16^3 \times 128$	0.0668(45)(1)	0.134(7)(5)	0.263(15)(9)
$20^3 \times 256$	0.0301(9)(0)	0.122(3)(1)	0.238(6)(1)
$24^3 \times 128$	0.0143(9)(1)	0.106(6)(4)	0.203(12)(7)
$32^3 \times 256^4$	0.00678(54)(81)	0.114(9)(13)	0.223(17)(26)

TABLE 4.3: The effective scattering length ($\overline{a}$) and $m_\pi f_\pi^4 \overline{\eta}_3^L$ extracted from fits to different ranges of n. For a fixed n_{max}, the χ^2/d.o.f. is larger in smaller volumes, indicating that Eq. (4.7) fails to describe systems of high densities.

	$n = [3,5]$			$n = [3,6]$		
$V^3 \times T$	$m_\pi \overline{a}$	$m_\pi f_\pi^4 \overline{\eta}_3^L$	χ^2/dof	$m\overline{a}$	$m_\pi f_\pi^4 \overline{\eta}_3^L$	χ^2/dof
$16^3 \times 128$	0.260(14)(2)	0.70(10)(4)	1.0	0.261(14)(1)	0.67(9)(3)	1.5
$20^3 \times 256$	0.234(6)(1)	0.80(8)(3)	0.25	0.235(6)(1)	0.79(7)(1)	0.5
$24^3 \times 128$	0.209(11)(4)	1.61(20)(20)	0.26	0.209(11)(3)	1.59(18)(12)	0.25
	$n = [3,7]$			$n = [3,8]$		
$V^3 \times T$	$m_\pi \overline{a}$	$m_\pi f_\pi^4 \overline{\eta}_3^L$	χ^2/dof	$m_\pi \overline{a}$	$m_\pi f_\pi^4 \overline{\eta}_3^L$	χ^2/dof
$16^3 \times 128$	0.262(14)(1)	0.64(9)(1)	3.5	0.263(14)(1)	0.62(8)(1)	5.5
$20^3 \times 256$	0.235(6)(5)	0.79(7)(1)	1.1	0.235(6)(1)	0.76(7)(1)	2.8
$24^3 \times 128$	0.211(11)(2)	1.56(17)(8)	0.4	0.210(11)(2)	1.50(16)(5)	1.0

4.7 Interaction parameters from small $\overline{a}/L$ expansion

The dimensionless qualities $m_\pi \overline{a}$ and $m_\pi f_\pi^4 \overline{\eta}_3^L$ can be extracted by fitting ΔE_n to the large volume expansion of Eq. (4.7). The fitting strategy is similar to that used in Lüscher's method by first fitting to each bootstrap ensemble and then computing the distribution of fitted parameters in order to get statistical and systematic uncertainties. There are two ways to extract $m\overline{a}$. One is by fitting only to ΔE_2 using Eq. (4.7) with the last two lines set to zero, and the other way is by fitting multiple ΔE_n's, with $n \geq 3$, and extracting $m_\pi f_\pi^4 \overline{\eta}_3^L$ at the same time as is shown in Table. 4.3 and Fig. 4.8. The final $\overline{a}$ and $m f_\pi^4 \overline{\eta}_3^L$ extracted from the later method

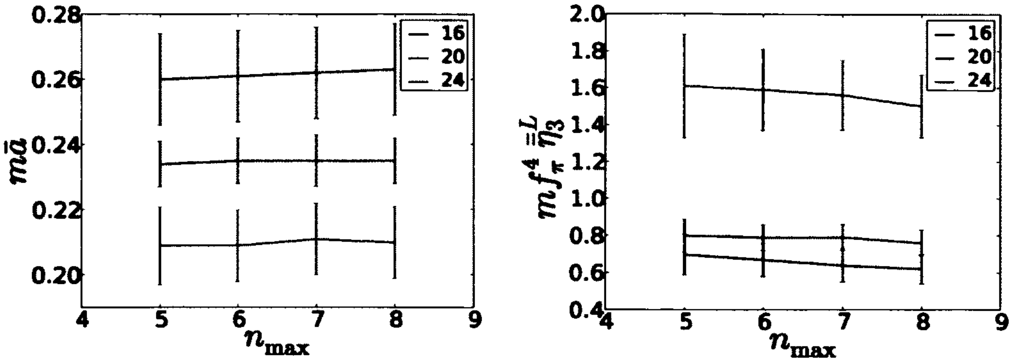

FIG. 4.8: The $m\bar{a}$ and $mf_\pi^4\bar{\eta}_3^L$ extracted from different fitting windows $[n_{\min}, n_{\max}]$ with $n_{\min} = 3$ fixed and varying $n_{\max}$.

are chosen from fits with $\chi^2 \sim 1$. We are forced to to use only few body systems as the quality of fit rapidly decreases for large numbers of pions. This suggests that the weakly interacting pion model of the system that Eq. (4.7) encodes is becoming less valid, particularly in small volumes. Results for the two-body interaction extracted in both ways agree within uncertainties with those extracted using Lüscher's method, and are shown in Table 4.4. The original data for the ΔE_n's and the results from the fits are shown in Fig. 4.9.

TABLE 4.4: The effective scattering length ($\bar{a}$) from small $\bar{a}/L$ expansion. The symbol "[2]" indicates that only ΔE_2 is used in the fitting, and "[3,6]" means that all ΔE_3 to ΔE_6 are used.

$V^3 \times T$	$m_\pi\bar{a}[2]$	$m_\pi\bar{a}[3,6]$	$k\cot\delta/m_\pi$	$m_\pi f_\pi^4\bar{\eta}_3^L$[3,6]
$16^3 \times 128$	0.259(14)(5)	0.260(14)(2)	−3.85(21)(3)	0.70(10)(4)
$20^3 \times 256$	0.234(6)(1)	0.235(6)(5)	−4.26(11)(10)	0.79(7)(1)
$24^3 \times 128$	0.205(12)(5)	0.210(11)(2)	−4.78(25)(7)	1.50(16)(15)

The effective scattering length, $\bar{a}$, extracted from the three volumes depends on the volume as the scattering momenta are not the same. With multiple volumes, Eq. (4.8) can be inverted to extract both the scattering length, a, and the effective range, r. During the fit, we have also used $k\cot\delta/m_\pi$ determined on a matching $32^3 \times 256$ and $24^3 \times 128$ ensembles from Ref. [10] with all lattice parameters the same. We are using the simplest form, $k\cot\delta/m_\pi = -\frac{1}{m_\pi a} + \frac{m_\pi r}{2}(\frac{k^2}{m_\pi^2})$, and neglecting

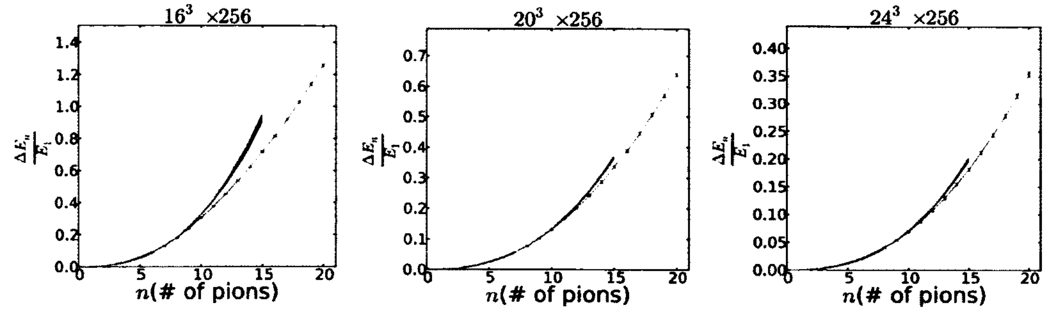

FIG. 4.9: The energy differences, ΔE_n, are plot as a function of the number of pions, n, where the blue points are the original data, the red bands are the fits, and the black bands are the regions where the fits are performed. From the left to right, ΔE_n from 16^3, 20^3, 24^3 are shown.

higher order shape parameters as our interacting momenta are small. The infinite volume results are $1/m_\pi a = 4.73(15)(13)$ and $m_\pi r = 27.4(7.9)(4.7)$, which agree with the determinations of Ref. [10]. The first error is the statistical error, and the difference between the infinite volume results by fitting with the data from the two ensembles in Ref. [10] and without them is taken as an additional systematic error. Both fits are shown in Fig. 4.10.

By utilizing the extracted effective range, r, and the effective scattering length, $\overline{a}(L)$, from the three different volumes, from Eq. (4.11), the volume dependent parameter $\overline{\eta}_3^L$, responsible for the three-body interactions can be determined for each volume. The extracted values of $\overline{\eta}_3^L$ are shown in Fig. 4.11. The dependence of $\overline{\eta}_3$ on the volume can be rewritten from Eq. (4.12) into a simpler form

$$\overline{\eta}_3^L(L) = C + \frac{\alpha a^4}{M}\log(L), \tag{4.13}$$

where C contains contributions independent of L, and $\alpha = 64\pi(3\sqrt{3}-4\pi) = -1.48 \times 10^3$. We fit $\overline{\eta}_3^L$ to our data to determine C and the best fit is shown in Fig. 4.11. However the χ^2 of the fit is poor and it appears that Eq (4.13) does not effectively explain the volume dependence of our data. This might come from competing higher order terms $\mathcal{O}(\frac{1}{L^3})$, but it also may be a statistical effect. The large value of $\overline{\eta}_3^L$ for

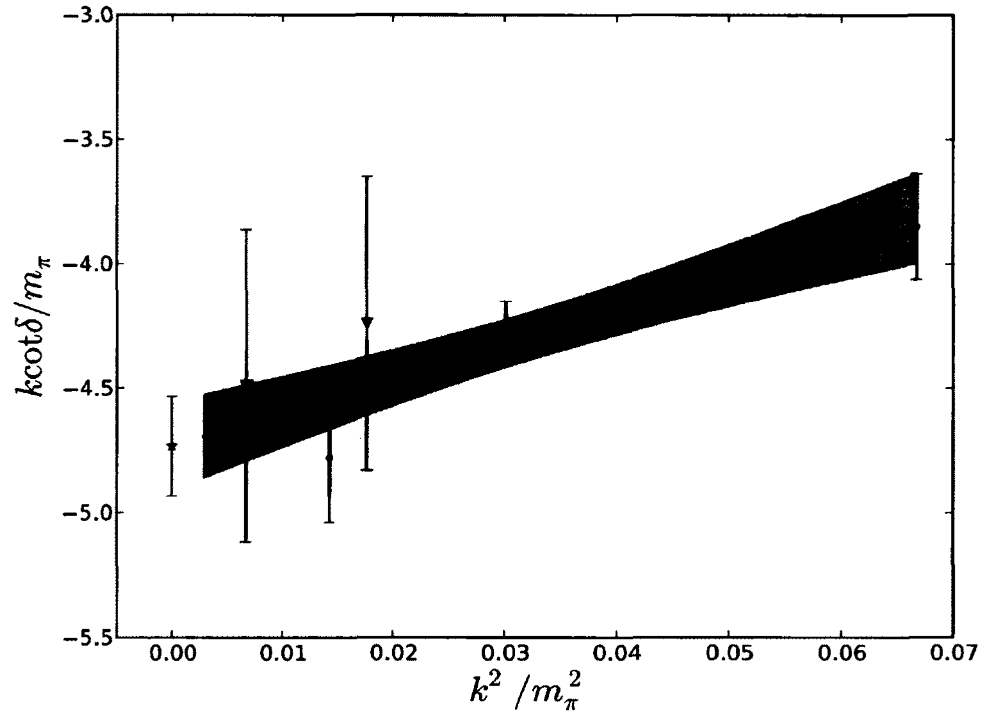

FIG. 4.10: The scattering phase shifts from 16^3, 20^3, and 24^3 ensembles in this study, are shown as the black dot data points from right to left respectively. The blue triangle data points are the 24^3 and 32^3 ensemble results from Ref. [10] from right to left respectively. The inner shaded region is the fit to all data, and the outer shaded region is the fit only to the data in this chapter, and the star is the infinite volume result.

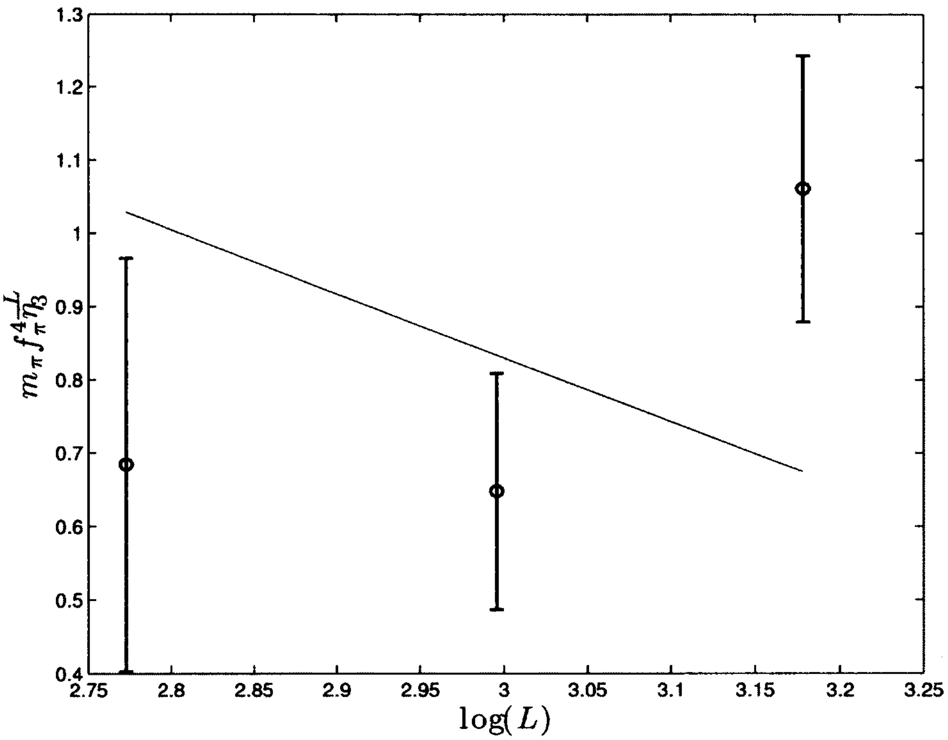

FIG. 4.11: The extracted three-body interaction parameter, $\overline{\eta}_3^L(L)$, is plotted as a function of the spatial extent of the lattice, L, (black points). The red line shows the expected dependence of $\overline{\eta}_3^L$ on L from Eq. (4.13) with $C = 4.3$, which clearly does not provide a good description of the data.

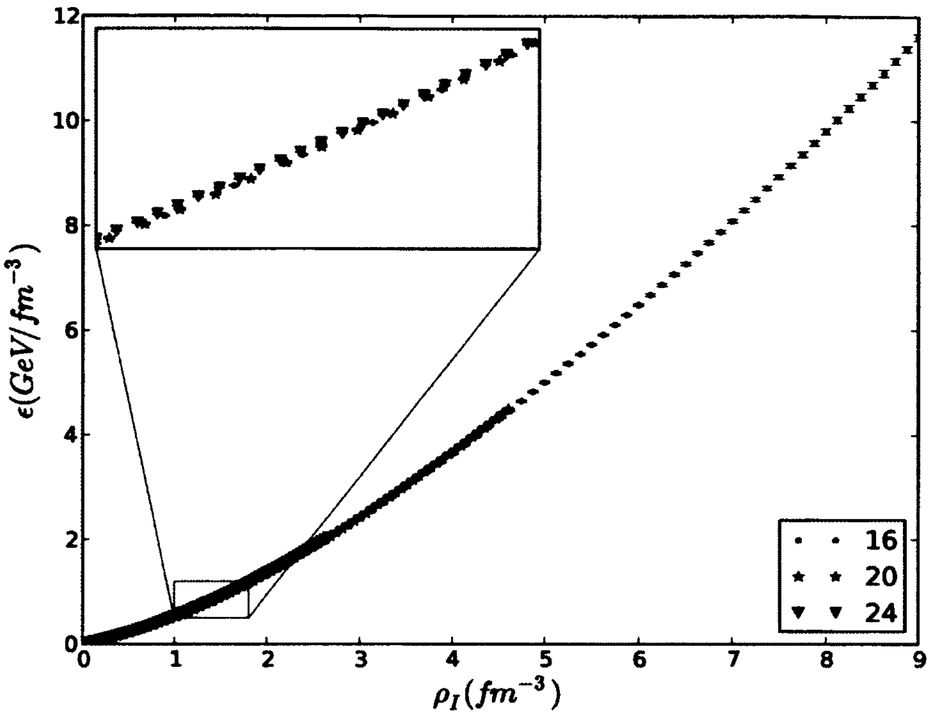

FIG. 4.12: Energy densities (ϵ) calculated on 3 different volumes are shown as a function of isospin density. The blue dot points are from the 16^3 ensemble, the black star ones are from the 20^3 ensemble and the pink triangle one are from the 24^3 ensemble. The inset show the slight difference in energy density on three ensembles.

$L = 24$ is correlated with a down shift of the scattering length $\bar{a}$. In Ref. [10], a value of $m\bar{a} = 0.236(18)(27)$ was found for $L = 24$, which agrees with the value $m\bar{a} = 0.210(16)(5)$ found above, but with a larger central value, perhaps indicating a statistical fluctuation.

4.8 QCD phase diagram at non-zero μ_I

In Fig. 4.12, we show the energy density, $\epsilon = \frac{E}{V}$, determined from the ground state energies, $E_{n\pi}$ that have been computed on each of the three volumes. For a fixed n, the pions are forced to be closer to each other in a smaller volume, and the repulsive interactions between them become stronger. This drives up the energy

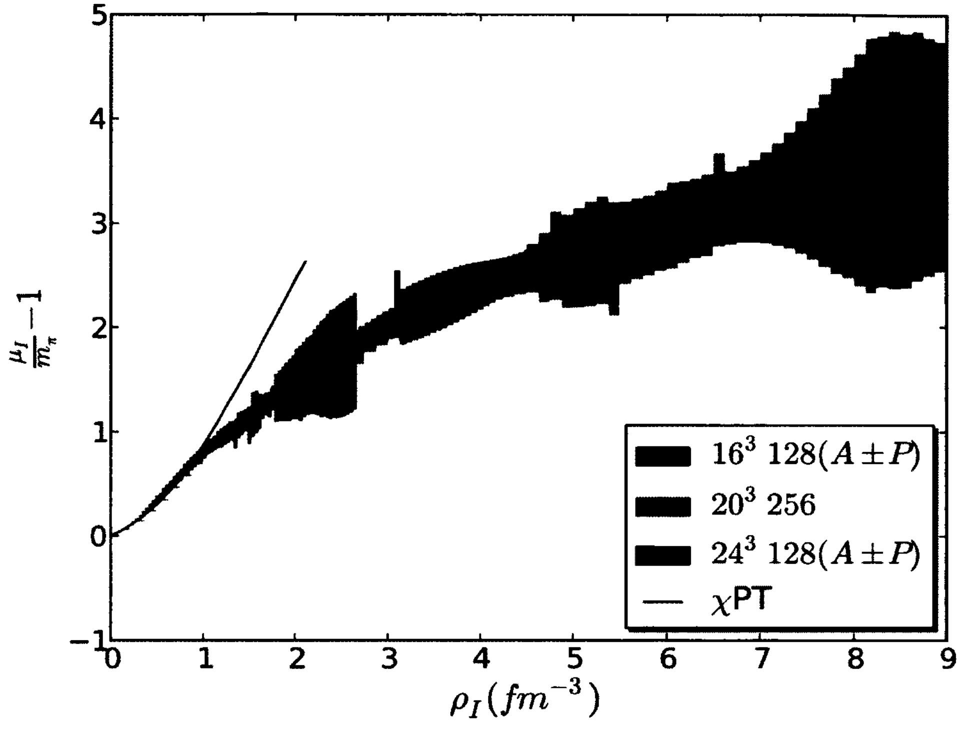

FIG. 4.13: The isospin chemical potential, μ_I, is plotted as a function of the isospin density, ρ_I, from three lattice ensembles, B1 (red, $\rho_I = [0, 9]$), B3 (blue, $\rho_I = [0, 2.8]$) and B4 (green, $\rho_I = [0, 4.7]$). The solid black line is from expectations of χPT [1]

of the whole system. The energy densities are weakly dependent on the volume, however there are slightly differences as shown in the inset of Fig. 4.12.

From the extracted ground state energies, the isospin chemical potential[5] can also be determined by a backward finite difference, $\mu_I(n) = \frac{dE}{dn} \sim E_n - E_{n-1}$. We calculate $\mu_I(n)$ on each bootstrap ensemble, which accommodates correlations between $E_{n\pi}$'s extracted on the same ensemble, and the systematic uncertainty of the $\mu_I(n)$ from each ensemble is evaluated by adding systematic uncertainty from varying the fit ranges used to determine E_n and E_{n-1} in quadrature. The final systematic uncertainty on $\mu_I(n)$ is from averaging the systematic uncertainties of all the bootstrap ensembles, and the statistical uncertainty is the standard deviation

---

[5] This is really an "effective" isospin chemical potential as it is defined from the ground state energy rather than the free energy

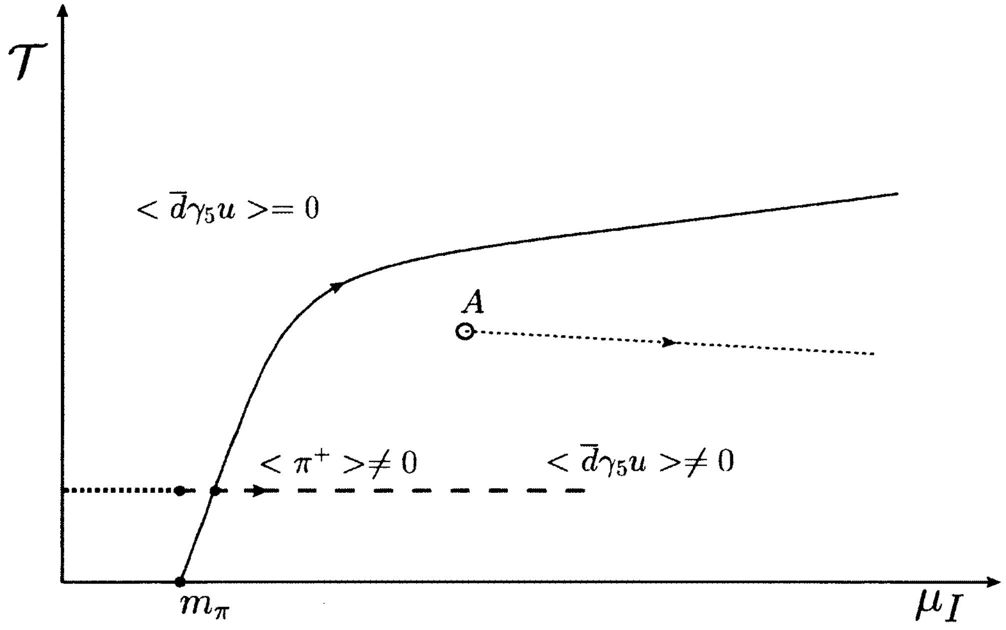

FIG. 4.14: Expected QCD phase diagram following Ref. [1]. At high temperature no bounded state of the quantum number of pion exist, thus $< \bar{d}\gamma_5 u >= 0$. At extremely high isospin chemical potential, although such state still has the same quantum number as pions, but quarks are not bounded inside hadrons, and they are starting to form Cooper pairs. Our calculations at a fixed temperature, $\mathcal{T} \sim 20$ MeV probe the phase structure along the red dashed line from $\mu_I = m_\pi$ to $\mu_I = 4.5\ m_\pi$. The position of phase transition A is unknown.

of the values of $\mu_I(n)$ on the individual bootstrap ensembles.

In Fig. 4.13, the dependence of $\mu_I/m_\pi - 1$ on the isospin density ρ_I is shown for the three volumes. The isospin chemical potential exhibits similar behaviour in all three volumes, where they overlap. At small ρ_I, μ_I increases at an accelerating rate, in agreement with the prediction from chiral perturbation theory (χPT) [1], however at around $\rho_I \approx 0.5$ fm^{-3} the behaviour of μ_I starts to change, and the accelerating rate gradually decreases, and at even higher isospin density the μ_I starts to flatten off. This change of behaviour of μ_I indicates that the physical state of the system may be altering.

The expected phase structure of QCD at non-zero isospin chemical potential has been discussed in Ref. [1]. At zero temperature, when $\mu_I < m_\pi$, there is not enough energy to excite a pion out of the vacuum. As soon as μ_I reaches m_π,

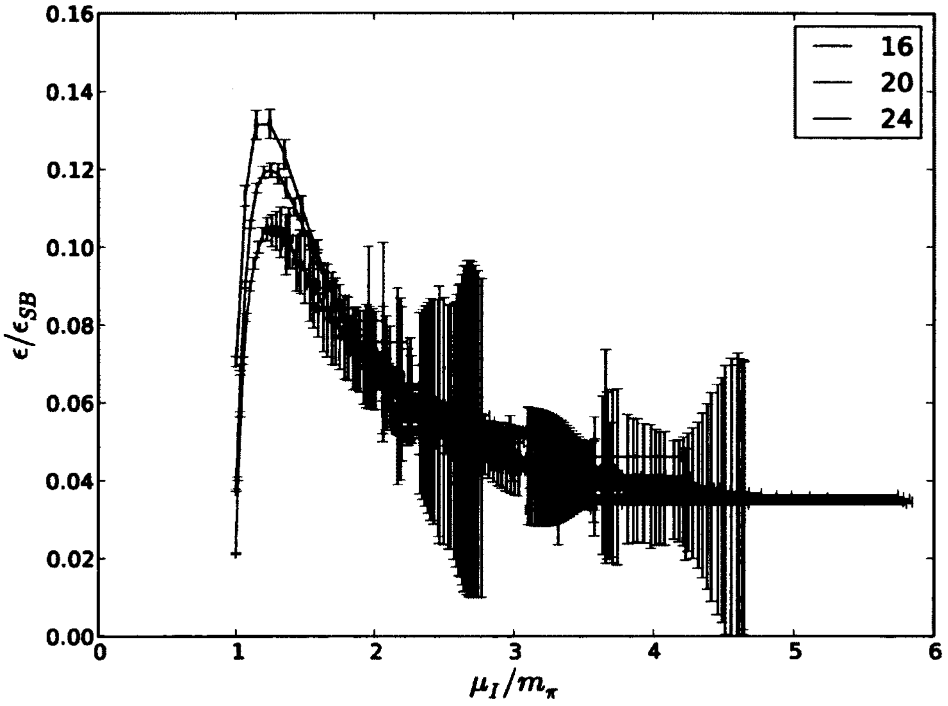

FIG. 4.15: The ϵ/ϵ_{SB} is plotted as a function of μ_I/m_π.

pions can be produced and the system is expected to enter a phase with a pion condensate (BEC). At asymptotically large values of μ_I, the attractive nature of one gluon exchange guarantees the existence of a BCS-like state in which quark–anti-quark Cooper pairs are formed. At an intermediate value of μ_I a BEC-BCS crossover is conjectured [1].

In this chapter, our calculations are performed at a small but nonzero temperature, $T \sim 20$ MeV. With the canonical method used in the current calculation, the lowest isospin chemical potential that we probe is $\mu_I = m_\pi$ by definition as we directly add π^+'s into the system. In the smallest volume, for $n = 72$ π^+'s (the largest value we consider), an isospin density of $\rho_I \sim 9$ fm^{-3} is achieved, and the phase diagram is explored from $\mu_I = m_\pi$ up to $\mu_I \approx 4.5\, m_\pi$ in this chapter as shown by the red dashed line in Fig. 4.14.

In order to investigate the possible phase transition suggested by the behaviour of the isospin chemical potential in more detail, we have also compared the extracted energy density with the energy density of a cold degenerate system described by a model of weakly interacting quarks filling their Fermi sphere up to a maximum momentum $k_F \approx E_F = \mu_I$ [18]. This Stefan-Boltzmann energy density is given by

$$\epsilon_{SB} = \frac{N_f N_c}{4\pi^2}\mu_I^4 \tag{4.14}$$

where $N_f = 3$ and $N_c = 3$. The ratio of ϵ/ϵ_{SB} is plotted in Fig. 4.8, and exhibits similar behaviours in all three volumes. The ratio increases from $\mu_I = m_\pi$ to a peak around $\mu_I \approx 1.3\ m_\pi$, and then drops and eventually begins to plateau at around $\mu_I \approx 3\ m_\pi$. The peak positions, μ^I_{peak}, for each volume identified from Fig. 4.8 are $\mu^I_{peak} = \{1.20(5), 1.25(5), 1.27(5)\}\ m_\pi$ for $L = \{16, 20, 24\}$ respectively. With an extrapolation linear in $1/L^3$, the peak position in infinite volume is $\mu^I_{peak} = 1.30(7)\ m_\pi$. The system for $\mu_I < 1.3\ m_\pi$, can be identified as a pion gas. When $\mu_I \sim \mu^I_{peak}$, pions start to condense and the system resides in the BEC state. The plateau beginning to form beyond $\mu_I \approx 3\ m_\pi$, may indicate a crossover from the BEC to BCS state, however higher precision and larger μ_I is required to make a definite statement. Discretization effects also remain to be investigated.

Two flavour QCD with finite μ_I at large temperature has been investigated in Ref. [43], where a finite temperature deconfinement phase transition was identified at $\mu_I < m_\pi$, however for $\mu_I > m_\pi$ no results were presented. In Ref. [19], the phase diagram of $N_f = 4 + 4$ QCD was investigated at different temperatures and values of μ_I using the grand canonical approach, and a phase transition from a pion gas to a BEC state has also been suggested at μ_I slightly higher than m_π, in agreement with the results found here. Two color QCD has been studied in Ref. [18], where the authors identified the transition from vacuum to BEC state and the BEC/BCS transition. Somewhat interestingly, the ratio of the energy density and its Stefan-Boltzmann limit has also been studied (inset of Fig. 1 in Ref. [18]), showing qualitatively similar behaviour to that found in the current study.

4.9 Summary

In this chapter, we have studied lattice QCD at non-zero isospin chemical potential using a canonical approach in which we have investigated systems with the quantum numbers of up to 72 π^+'s in three lattice volumes, $L^3 \sim$ (2.0, 2.5 and 3.0 fm)^3 at a pion mass of $m_\pi \sim 390$ MeV at a single lattice spacing.

In our analysis, we have determined the ground state energies of multi-pion systems in three different volumes and have used this to extract the isospin chemical potential and isospin energy density of the states that are produced. In the smallest volumes, systems with isospin chemical potentials of up to $\mu_I \sim 1600$ MeV are created. By considering the energy density as a function of the isospin chemical potential, we provide strong evidence for the transition of the system from a weakly interacting pion gas to a Bose-Einstein condensed (BEC) phase at $\mu \sim m_\pi$ as expected from χPT. At higher values of the chemical potential the system is expected to transition to a BCS state and we have sought numerical evidence for this but do not have conclusive results. It is interesting to note that the behaviour of the energy density as a function of the isospin chemical potential is very similar to that recently found in two-colour QCD with a baryon chemical potential by Hands et al. [18].

By focusing on few pion systems, we have extracted the two and three pion interactions, determining the scattering length, effective range and the renormalisation group invariant effective three-body interaction. The scattering parameters were found to be in good agreement with other recent determinations and we have attempted to investigate the intrinsic volume dependence of the renormalisation group invariant three-pion interaction. We have also found that as the density increases and the system transitions to a BEC, it can no longer be well described in terms of weak few-body interactions.

CHAPTER 5

Energy shift of heavy quarkonia [1]

5.1 Introduction

An important probe of exotic phases of QCD matter is the way in which heavy quarkonium propagation is modified by the presence of that matter. The heavy quarks can in some sense be viewed as separable from the medium which is predominantly composed of light quark and gluonic degrees of freedom. At non-zero temperature, the suppression of the propagation of J/ψ particles is a key signature for the formation of a quark-gluon plasma [44]. This suppression has been observed for charmonium in various experiments at SPS and RHIC and recently in the Υ spectrum at the LHC [3]. Quarkonium propagation is naturally also expected to be a sensitive probe of other changes of phase such as those that occur at high density or large isospin density.

Since the effects of QCD matter on quarkonia are essentially non-perturbative in origin, a systematic evaluation requires input from lattice QCD. At some level, these effects can be distilled to a change in the potential between the quark–anti-

---

[1] This section is in collaboration with William Detmold and Stefan Meinel, and results for bottomonium studies can be found in Ref. [7].

quark ($Q\overline{Q}$) pair that binds them into quarkonium. At non-zero temperature but zero density, this has been studied extensively using lattice QCD (see Ref. [45] for a recent overview) where strong screening effects are seen near the deconfinement scale. Significant effects are also seen in investigations of the properties of charmonium and bottomonium spectral functions at non-zero temperature (see [45, 46]).

Modifications of the potential or of quarkonium properties will also occur for non-zero density. Ref. [47] has investigated the static potential in the presence of a gas of pions. As the main focus of this chapter, however, we explore the effects of isospin charge density on quarkonium bound state energies more directly by using lattice NRQCD (non-relativistic QCD) to compute quarkonium correlation functions in the presence of a medium of varying isospin chemical potential. At low isospin densities, and correspondingly low chemical potentials, we find that the ground state energy of the quarkonium systems decreases with increasing isospin density, showing qualitative agreement between the potential model calculation and the QCD calculation. However, at an effective isospin chemical potential $\mu_I \sim \mu_{I,\text{peak}} = 1.3\ m_\pi$ (where the calculations presented in the previous chapter suggested a transition to a Bose-Einstein condensed state in line with theoretical expectations [48]), the effect of the medium on the quarkonium energy appears to saturate to a constant shift. At still larger chemical potentials, the determination of the energy shift becomes statistically noisy. The marked change in behaviour provides additional support to the notion of the change in phase of the system.

5.2 Lattice methodologies

In this study, we make use of same gauge ensembles as those in previous chapters. We investigate three different ensembles, corresponding to different physical volumes and temporal extents as shown in Table 5.1. The different physical volumes allow us to access a large range of isospin densities in our study, and the different temporal extents provide control of thermal effects as discussed in Ref. [11]. On these gauge configurations we calculate correlation functions involving light quarks and use the colourwave propagator basis introduced earlier, fixing to Coulomb gauge and using plane-wave sources and sinks for a range of low momenta (N_{mom} in total on each ensemble, see Table 5.1). For each case, we calculate light-quark propagators on N_{cfg} configurations from N_{src} time-slices, equally spaced throughout the temporal extent by applying new methodologies constructed in the last section.

	$L^3 \times T$	L[fm]	$m_\pi L$	$m_\pi T$	u_{0s}	N_{cfg}	N_{src}	N_{mom}
B1	$16^3 \times 128$	2.0	3.86	8.82	0.7618	334	8	33
B3	$20^3 \times 256$	2.5	4.82	17.64	0.7617	170	16	7
B4	$24^3 \times 128$	3.0	5.79	8.82	0.7617	170	8	19

TABLE 5.1: Details of the ensembles and measurements used in this work. u_{0s} is defined as the fourth root of the spatial plaquette.

5.3 Bottomonium in media of non-zero isospin chemical potential

5.3.1 Multi-pion and bottomonium lattice correlators

In order to produce the medium that will modify the propagation of the quarkonium states, we use the canonical approach of constructing many-pion correlation functions that is described in detail in Chapter 3, using methods developed there and in earlier works [49, 2, 20, 9, 50]. As discussed in Chapter 4, correlators of a fixed isospin charge, $n = \sum_{i=1}^{N} n_i$, and total momentum, $\mathbf{P}_f$, making use of N sources, are given by Equation (4.1).

NRQCD is applied to calculate bottom quark propagators, In the main calculations of this work, we use zero-momentum smeared quarkonium interpolating fields

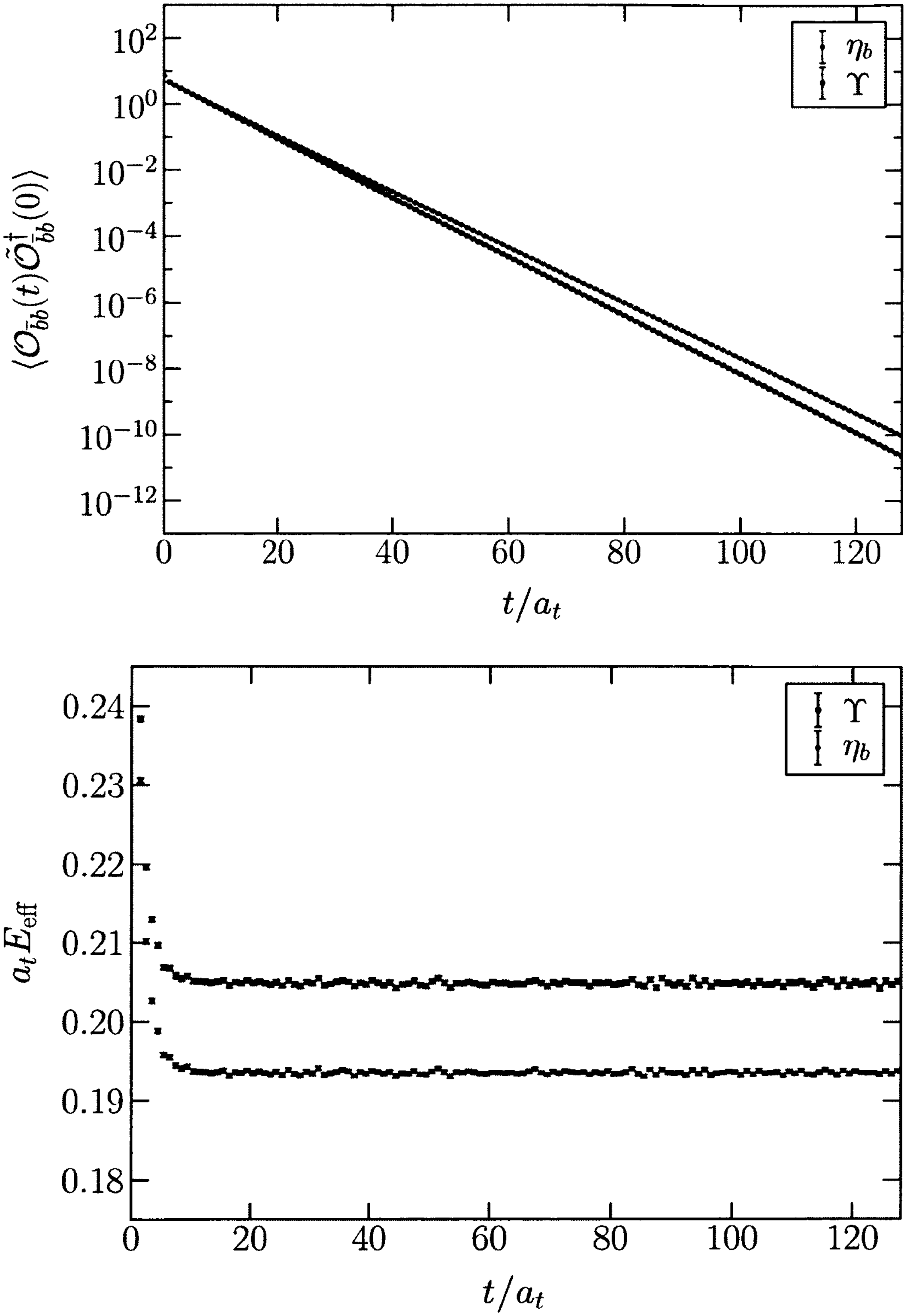

FIG. 5.1: η_b and Υ correlators (upper) and effective energies (lower) on the $20^3 \times 256$ ensemble, for $a_s m = 2.75$.

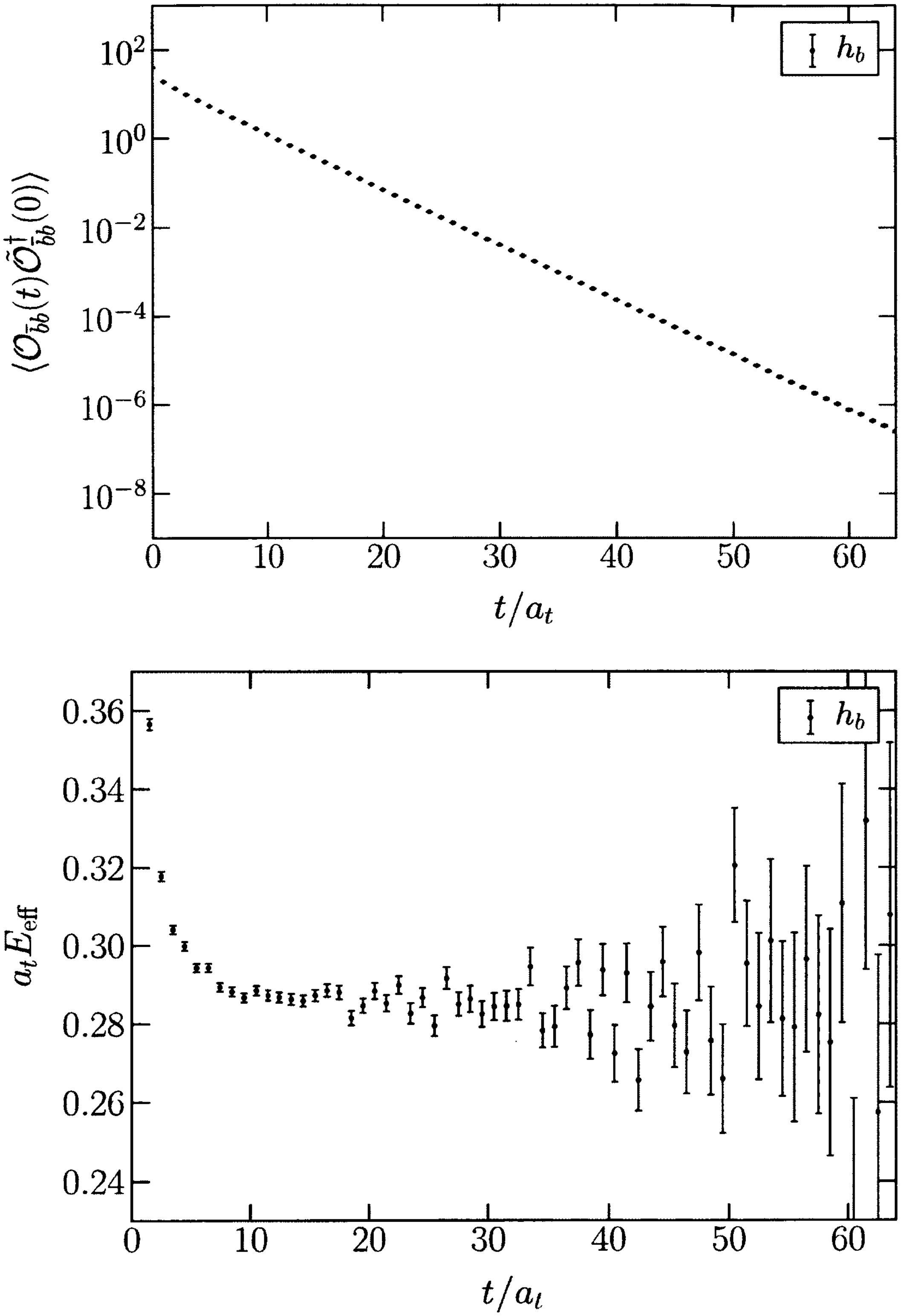

FIG. 5.2: h_b correlator (upper) and effective energy (lower) on the $16^3 \times 128$ ensemble, for $a_sm = 2.75$.

of the form

$$\mathcal{O}_{\bar{b}b}(t) = \sum_{\mathbf{y}'}\sum_{\mathbf{y}} \chi^{\dagger}(\mathbf{y}',t)\Gamma(\mathbf{y}-\mathbf{y}')\psi(\mathbf{y},t) \tag{5.1}$$

at the sink and

$$\tilde{\mathcal{O}}_{\bar{b}b}(0) = \sum_{\mathbf{x}} \chi^{\dagger}(\mathbf{0},0)\Gamma(\mathbf{x})\psi(\mathbf{x},0) \tag{5.2}$$

at the source. Here, χ is the heavy anti-quark field and $\Gamma(\mathbf{r})$ is the smearing function, which is a 2×2 matrix in spinor space. The quantum numbers of the quarkonium interpolating fields considered in this work are listed in Table 5.2. More details about the NRQCD heavy quark propagator calculations are discussed in Ref. [7]. Correlation functions and effective masses of η_b and Υ_b computed on the $20^3 \times 256$ and $16^3 \times 128$ ensembles are shown in Fig. 5.1 and Fig. 5.2 respectively. In order to investigate how bottomonium energy shifts depend on the mass of the bottom quark, bottom quark propagators for different quark masses are computed and corresponding spin-averaged values of the $1S$ kinetic masses, $\overline{M_{\text{kin}}} = (3M_{\text{kin}}^{\Upsilon} + M_{\text{kin}}^{\eta_b})/4$ computed on the $16^3 \times 128$ ensemble (at $\rho_I = 0$), are given in Table 5.3.

Name	$\mathcal{R}^{PC}$	$\Gamma(\mathbf{r})$
η_b	A_1^{-+}	$\phi_{1S}(\mathbf{r})$
Υ	T_1^{--}	$\phi_{1S}(\mathbf{r})\,\sigma_j$
h_b	T_1^{+-}	$\phi_{1P}(\mathbf{r},j)$
χ_{b0}	A_1^{++}	$\sum_j \phi_{1P}(\mathbf{r},j)\,\sigma_j$
χ_{b1}	T_1^{++}	$\sum_{k,l} \epsilon_{jkl}\,\phi_{1P}(\mathbf{r},k)\,\sigma_l$
χ_{b2}	T_2^{++}	$\phi_{1P}(\mathbf{r},j)\,\sigma_k + \phi_{1P}(\mathbf{r},k)\,\sigma_j$ (with $j \neq k$)

TABLE 5.2: Smearing functions $\Gamma(\mathbf{r})$ used in the quarkonium interpolating fields for the given representation of the cubic group, $\mathcal{R}$ and values of parity, P, and charge-conjugation, C. The functions $\phi_{1S}(\mathbf{r})$ and $\phi_{1P}(\mathbf{r},j)$ are eigenfunctions from a lattice potential model.

$a_s m$	$a_t M_{\rm kin}$	$M_{\rm kin}$ (GeV)
1.2	0.7698(81)	4.333(54)
1.5	0.9377(16)	5.277(36)
2.0	1.2259(12)	6.900(46)
2.75	1.6667(12)	9.380(62)

TABLE 5.3: Spin-averaged quarkonium kinetic masses on the $16^3 \times 128$ ensemble.

5.3.2 Correlator ratios for energy shifts

To investigate the effect of the medium on quarkonium propagation, we consider the correlators

$$C(n;\bar{b}b;t) \;=\; \langle \mathcal{O}_{\bar{b}b}(t)\mathcal{O}_{n\pi^+}(t)\tilde{\mathcal{O}}^\dagger_{\bar{b}b}(0)\mathcal{O}^\dagger_{n\pi^+}(0)\rangle\,, \tag{5.3}$$

where $\langle\ldots\rangle$ denotes path integration via the average over our ensembles of gauge configurations, and the interpolators $\mathcal{O}^\dagger_{n\pi^+}$ and $\mathcal{O}^\dagger_{\bar{b}b}$ produce the quantum numbers of n-pion and $\bar{b}b$ states as discussed in the preceding subsection. States with the combined quantum numbers of the given quarkonium state ($\bar{b}b$ is either η_b, Υ, h_b, χ_{b0}, χ_{b1} or χ_{b2}) and the n-pion system propagate in this correlator and naturally, the spectrum of this system is different from the sum of the spectra of n pions and of quarkonium because of interactions. At Euclidean times where only the ground state of the system is resolved (after excited states have decayed and before thermal states are manifest), this correlator will decay exponentially as

$$C(n;\bar{b}b;t) \longrightarrow \tilde{Z}_{n;\bar{b}b}\exp(-E_{n;\bar{b}b}t)\,, \tag{5.4}$$

where $E_{n;\bar{b}b}$ is the ground-state energy of the combined system.

To access the change in the quarkonium energy as a function of isospin density or chemical potential, we further construct the ratios

$$R(n,\bar{b}b;t) \;=\; \frac{\langle \mathcal{O}_{\bar{b}b}(t)\mathcal{O}_{n\pi^+}(t)\tilde{\mathcal{O}}^{\dagger}_{\bar{b}b}(0)\mathcal{O}^{\dagger}_{n\pi^+}(0)\rangle}{\langle \mathcal{O}_{\bar{b}b}(t)\tilde{\mathcal{O}}^{\dagger}_{\bar{b}b}(0)\rangle\langle \mathcal{O}_{n\pi^+}(t)\mathcal{O}^{\dagger}_{n\pi^+}(0)\rangle}\,. \tag{5.5}$$

Since the two terms in the denominator decay exponentially at large times as $\exp(-E_{\bar{b}b}t)$ and $\exp(-E_{n\pi^+}t)$ respectively, the ratio will behave as

$$R(n;\bar{b}b;t) \longrightarrow Z_{n;\bar{b}b}\exp(-\Delta E_{n;\bar{b}b}t) + \ldots\,, \tag{5.6}$$

where $\Delta E_{n;\bar{b}b} = E_{n;\bar{b}b} - E_{n\pi^+} - E_{\bar{b}b}$ is the quantity of central interest in our investigation.

5.3.3 Quarkonium–pion scattering

The quarkonium state in the presence of a single pion allows us to study the scattering phase shift of this two-body system using the finite-volume formalism developed by Lüscher [36, 37]. The S-wave quarkonium states that we consider have angular momentum $J = 0, 1$ and define the total angular momentum of the entire system since the pion is spin-zero. Since the pion and $\bar{b}b$ states have different masses, the appropriate generalisation of the Lüscher relation to asymmetric systems [51] is required. We can define a scattering momentum $p = |\mathbf{p}|$ through the relation

$$\begin{aligned}\sqrt{|a_s\mathbf{p}|^2/\xi^2 + \mathbf{a_t^2 M_{\bar{b}b}^2}} + \sqrt{|a_s\mathbf{p}|^2/\xi^2 + \mathbf{a_t^2 M_\pi^2}}& \\ = a_t\Delta E_{\bar{b}b,\pi} + a_t M_{\bar{b}b} + a_t M_\pi\,,&\end{aligned} \tag{5.7}$$

where $M_{\bar{b}b} \equiv M_{\rm kin}^{\bar{b}b}$ is the kinetic mass of the $\bar{b}b$ state. The scattering momentum then determines the eigenvalue equation

$$\begin{aligned} p\cot\delta_{\bar{b}b,\pi}(p) &= \frac{1}{\pi L}\mathbf{S}\left(\frac{p^2L^2}{4\pi^2}\right), &(5.8)\\ \mathbf{S}(x) &= \lim_{\Lambda\to\infty}\left[\sum_{\mathbf{n}\neq 0}^{|\mathbf{n}|<\Lambda}\frac{1}{|\mathbf{n}|^2+x}-4\pi\Lambda\right], &(5.9)\end{aligned}$$

that is satisfied by the $\bar{b}b$–π scattering phase shift, $\delta_{\bar{b}b,\pi}(p)$, at the scattering momentum.

Since we have three different lattice volumes, we can extract the phase shift at multiple momenta. In Figure 5.3, we show the phase shifts that we extract for the η_b–π and Υ–π scattering channels. These interactions necessarily vanish at zero momentum in the chiral limit as the quarkonium states are chiral singlet objects. We therefore expect only small scattering phase shifts at the quark masses considered in our study. At the level of statistical precision we have achieved, we are able to resolve the phase shifts from zero, and they are indeed found to be small. The measured values of the S-wave phase shifts are given in Tables 5.4 and 5.5, while for the P-wave states we are unable to extract statistically meaningful results. Since the measured scattering momenta are small, it is possible to perform a fit to the effective-range expansion

$$p\cot\delta(p)/m_\pi = -\frac{1}{m_\pi a}+\frac{m_\pi r}{2}\frac{p^2}{m_\pi^2}+\dots, \qquad (5.10)$$

to extract the scattering length and effective range for these interactions. This extrapolation is shown in Fig. 5.3 and results in $m_\pi a_{\eta_b,\pi} = 0.039(13)$ and $m_\pi r_{\eta_b,\pi} = 4.7(3.7)$ for the η_b state, and $m_\pi a_{\Upsilon,\pi} = 0.047(14)$ and $m_\pi r_{\Upsilon,\pi} = 5.8(3.3)$ in the case of the Υ, both channels corresponding to a weak attractive interaction.

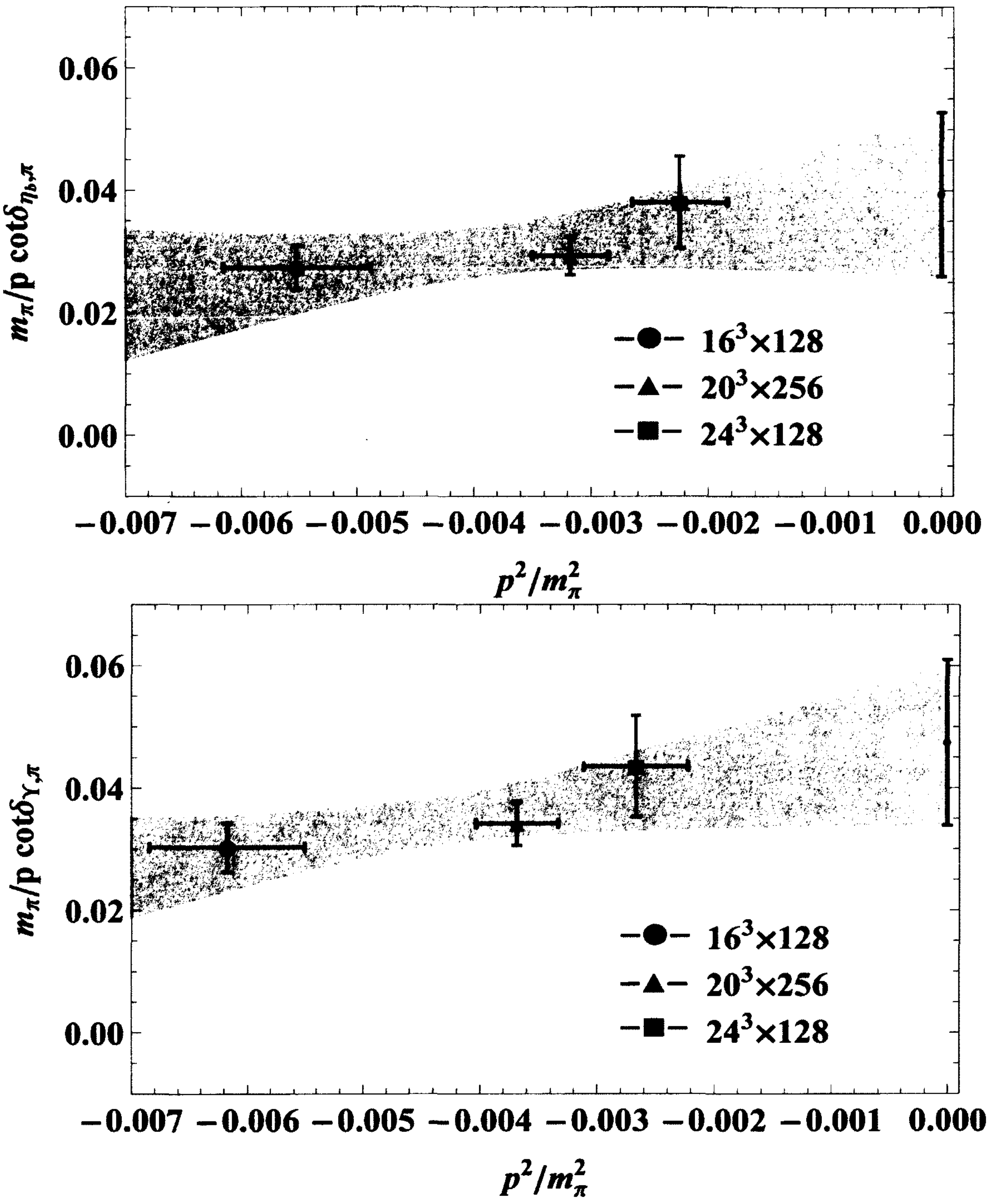

FIG. 5.3: Extracted inverse phase shifts for η_b–π and Υ–π scattering. Fitting the phase shift to $p\cot\delta(p)/m_\pi = -\frac{1}{m_\pi a} + \frac{m_\pi r}{2}\frac{p^2}{m_\pi^2}$, as shown by the shaded band, we can extract the scattering length shown by the point at $p^2/m_\pi^2 = 0$.

The pion-quarkonium scattering length depends approximately quadratically on the pion mass [52, 53, 54], and hence we can estimate the scattering length at the physical pion mass as

$$a^{(\mathrm{phys.})}_{\overline{b}b,\pi} \approx \left(m_\pi^{(\mathrm{phys.})}/m_\pi\right)^2 a_{\overline{b}b,\pi}, \tag{5.11}$$

where $a_{\overline{b}b,\pi}$ is our lattice result for the scattering length at $m_\pi = 390$ MeV. This gives

$$a^{(\mathrm{phys.})}_{\eta_b,\pi} = 0.0025(8)(6)\ \mathrm{fm}, \quad a^{(\mathrm{phys.})}_{\Upsilon,\pi} = 0.0030(9)(7)\ \mathrm{fm}, \tag{5.12}$$

where the first uncertainty is statistical and the second uncertainty is an estimate of missing higher-order corrections to Eq. (5.11), which we estimate to be smaller than the leading-order term by a factor of $m_\pi/(4\pi f_\pi) \approx 0.24$. The values (5.12) are comparable to, and considerably more precise than estimates from phenomenological models [55, 56, 57, 58].

TABLE 5.4: The η_b–π phase shifts extracted using the Lüscher method as described in the main text.

$V^3 \times T$	p^2/m_π^2	$(p\cot\delta(p))^{-1}$[fm]	$m_\pi/(p\cot\delta(p))$
$16^3 \times 128$	−0.0055(6)	0.0138(18)	0.0274(36)
$20^3 \times 256$	−0.0032(3)	0.0148(15)	0.0294(31)
$24^3 \times 128$	−0.0022(4)	0.0192(38)	0.0381(75)

TABLE 5.5: The Υ–π phase shifts extracted using the Lüscher method as described in the main text.

$V^3 \times T$	p^2/m_π^2	$(p\cot\delta(p))^{-1}$[fm]	$m_\pi/(p\cot\delta(p))$
$16^3 \times 128$	−0.0062(7)	0.0153(20)	0.0303(40)
$20^3 \times 256$	−0.0037(4)	0.0172(18)	0.0341(36)
$24^3 \times 128$	−0.0027(4)	0.0220(42)	0.0435(83)

5.3.4 Isospin density dependence of quarkonium

For larger isospin charge, we interpret the system of pions in terms of a medium of varying isospin charge density once the ground state is reached. In the correlators $C(n; \bar{b}b; t)$, the quarkonium state exists in this medium, interacting with it. We consider first the S-wave quarkonium states as they are statistically better resolved than P-wave states.

5.3.5 S-wave states

The correlators $C(n, \bar{b}b, t)$ are shown in Fig. 5.4 for $\bar{b}b = \Upsilon$ at representative values of the isospin charge and for $a_s m = 2.75$ on the $20^3 \times 256$ and $16^3 \times 128$ ensembles. The in-medium correlators on the $20^3 \times 256$ ensemble exhibit a long region of Euclidean time in which they decay as a single exponential. This region overlaps with the regions in which the multi-pion correlators and the individual quarkonium correlators are saturated by their respective ground states. This gives us confidence that by considering the correlator ratios of Eq. (5.5) we can legitimately extract the quarkonium energy shifts in medium. On the ensembles with $T = 128$, thermal contamination is more significant and restricts the range of useful time-slices, particularly for large isospin charge.

The correlator ratios, $R(n, \bar{b}b; t)$, discussed above, are shown for both Υ and η_b at a heavy quark mass $a_s m = 2.75$ on the $20^3 \times 256$ ensemble for a range of different isospin charges, n = 6, 12, and 18, in Figs. 5.5 and 5.6 along with fits to time dependence using Eq. (5.6). Fits are performed over a range of times where both the individual multi-pion correlation functions and quarkonium correlation functions exhibit ground-state saturation and are free from thermal (backward propagating) state contamination. This is ensured by choosing the central fit range $[t_{\text{min}}, t_{\text{max}}]$ such that a fit over the range $[t_{\text{min}} - 5, t_{\text{max}} + 5]$ has an acceptable quality of fit.

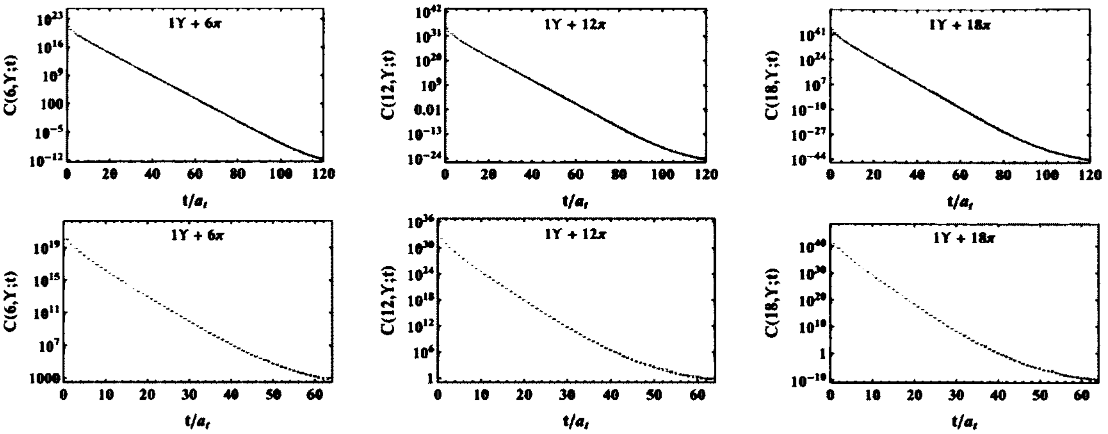

FIG. 5.4: The correlators for the Υ in a medium corresponding to isospin charge n for $n = 6$, 12, and 18 are shown. Data are presented for $a_s m = 2.75$ on the $20^3 \times 256$ (upper) and $16^3 \times 128$ (lower) ensembles. Correlators for the η_b in medium behave similarly.

On the $20^3 \times 256$ ensemble, we choose $t_{\text{min}} = 20$ and $t_{\text{max}} = 60$, beyond which thermal contributions are apparent. Because thermal contributions are more significant for the ensembles with $T = 128$, we choose $t_{\text{max}} = 40$ for these cases. Statistical uncertainties are estimated using the bootstrap procedure. To estimate the systematic uncertainties of the fits, we calculate the standard deviation between the three energies extracted from fits with the ranges $[t_{\text{min}} - 5, t_{\text{max}} - 5]$, $[t_{\text{min}}, t_{\text{max}}]$, and $[t_{\text{min}} + 5, t_{\text{max}} + 5]$ for $T = 128$ ensembles, and $[t_{\text{min}} - 5, t_{\text{max}} - 20]$, $[t_{\text{min}}, t_{\text{max}}]$, and $[t_{\text{min}} + 5, t_{\text{max}} + 20]$ for the $T = 256$ ensemble, on each bootstrap sample. The systematic uncertainty is then obtained as the average of this standard deviation over the bootstrap samples.

The extracted energy shifts and uncertainties are shown in Table 5.6 for Υ and Table 5.7 for η_b. For larger values of n, the energy shifts become noisier and we limit our analysis to the range of isospin densities where a successful fit could be performed for a given ensemble.

As a check of the methods of our study, we construct ratios in which we artificially remove the correlations between the $\bar{b}b$ system and the many-pion state by

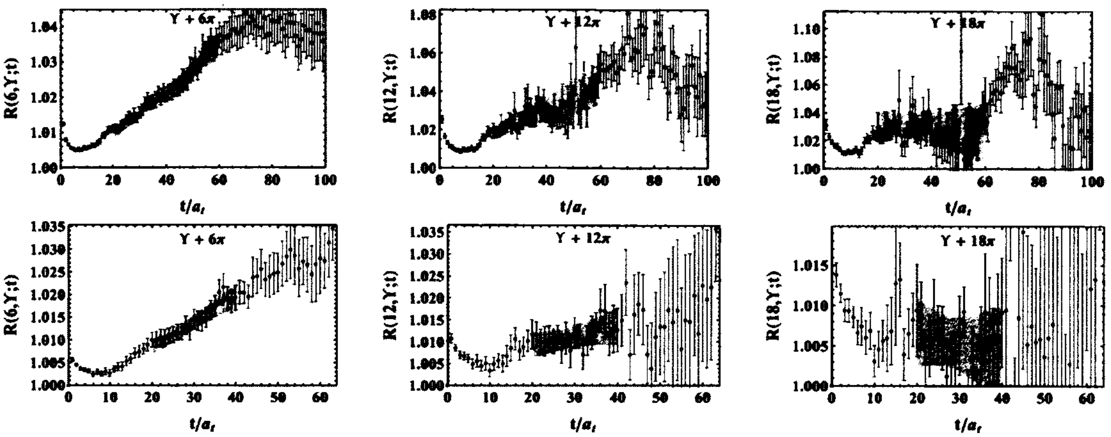

FIG. 5.5: The correlator ratios for the Υ in a medium corresponding to isospin charges $n = 6$, 12, 18. The shaded bands show the statistical uncertainties of fits of the form given in Eq. (5.6). Data are shown for $a_s m = 2.75$ on the $20^3 \times 256$ (upper) and $16^3 \times 128$ (lower) ensembles.

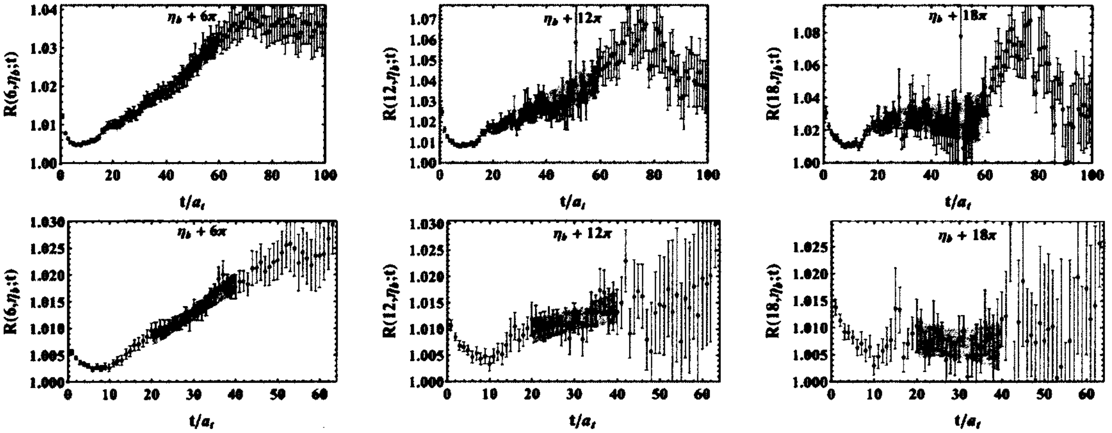

FIG. 5.6: The correlator ratios for the η_b in a medium corresponding to isospin charges $n = 6$, 12, 18. The shaded bands show the statistical uncertainties of fits of the form given in Eq. (5.6). Data are shown for $a_s m = 2.75$ on the $20^3 \times 256$ (upper) and $16^3 \times 128$ (lower) ensembles.

n	$\Delta E_{n;\Upsilon}$		
	$16^3 \times 128$	$20^3 \times 256$	$24^3 \times 128$
1	−1.23(12)(09)	−0.72(07)(03)	−0.53(07)(06)
2	−2.15(23)(15)	−1.38(14)(07)	−1.01(15)(11)
3	−2.75(34)(20)	−1.99(22)(13)	−1.44(23)(14)
4	−3.08(45)(23)	−2.54(31)(21)	−1.80(31)(16)
5	−3.23(58)(29)	−3.04(40)(28)	−2.08(41)(18)
6	−3.23(70)(37)	−3.47(51)(36)	−2.27(51)(20)
7	−3.10(81)(45)	−3.81(61)(45)	−2.37(63)(24)
8	−2.86(92)(51)	−4.03(73)(53)	−2.38(77)(31)
9	−2.51(1.00)(56)	−4.12(86)(62)	−2.31(93)(41)
10	−2.10(1.2)(0.6)	−4.1(1.0)(0.7)	−2.2(1.1)(0.5)
11	−1.7(1.3)(0.7)	−3.8(1.2)(0.9)	−1.9(1.3)(0.7)
12	−1.2(1.4)(0.8)	−3.4(1.4)(1.1)	−1.6(1.5)(0.8)
13	−0.8(1.6)(1.0)	−2.8(1.7)(1.3)	−1.3(1.8)(1.0)
14	−0.4(1.8)(1.2)	−2.1(2.0)(1.6)	−1.0(2.0)(1.2)
15	−0.0(2.0)(1.4)	−1.3(2.4)(1.9)	−0.6(2.3)(1.4)
16	0.3(2.1)(1.7)	−0.5(2.8)(2.2)	−0.2(2.6)(1.6)
17	0.6(2.3)(1.9)	0.2(3.1)(2.4)	0.2(2.9)(1.8)
18	0.8(2.4)(2.2)	0.9(3.5)(2.6)	0.5(3.2)(2.0)
19	1.1(2.5)(2.4)	1.5(3.8)(2.8)	0.8(3.5)(2.2)
20	1.3(2.5)(2.6)	2.1(4.0)(2.9)	1.0(3.8)(2.4)

TABLE 5.6: Fits to the Υ correlator ratios on the various ensembles for $a_s m = 2.75$. For each combination, we report: the mean and the statistical and systematic uncertainties.

n	$\Delta E_{n;\eta_b}$		
	$16^3 \times 128$	$20^3 \times 256$	$24^3 \times 128$
1	$-1.12(11)(08)$	$-0.62(06)(02)$	$-0.46(06)(06)$
2	$-1.95(21)(14)$	$-1.20(12)(06)$	$-0.89(13)(10)$
3	$-2.51(30)(18)$	$-1.74(19)(12)$	$-1.26(21)(13)$
4	$-2.83(40)(21)$	$-2.25(28)(19)$	$-1.57(29)(14)$
5	$-2.97(51)(26)$	$-2.73(37)(28)$	$-1.81(37)(16)$
6	$-2.99(61)(31)$	$-3.17(47)(37)$	$-1.97(47)(18)$
7	$-2.89(71)(37)$	$-3.53(58)(46)$	$-2.05(58)(22)$
8	$-2.69(81)(41)$	$-3.80(70)(54)$	$-2.05(71)(29)$
9	$-2.40(89)(44)$	$-3.95(83)(62)$	$-1.97(86)(38)$
10	$-2.05(97)(47)$	$-3.95(96)(72)$	$-1.8(1.0)(0.5)$
11	$-1.7(1.1)(0.5)$	$-3.8(1.1)(0.8)$	$-1.6(1.2)(0.6)$
12	$-1.3(1.2)(0.7)$	$-3.5(1.2)(1.0)$	$-1.3(1.4)(0.8)$
13	$-0.9(1.3)(0.8)$	$-3.1(1.4)(1.2)$	$-1.0(1.6)(1.0)$
14	$-0.6(1.4)(1.0)$	$-2.5(1.6)(1.5)$	$-0.6(1.9)(1.1)$
15	$-0.3(1.5)(1.3)$	$-1.9(1.8)(1.8)$	$-0.3(2.1)(1.3)$
16	$-0.0(1.6)(1.5)$	$-1.2(2.1)(2.1)$	$0.1(2.4)(1.5)$
17	$0.2(1.7)(1.8)$	$-0.6(2.3)(2.4)$	$0.4(2.7)(1.7)$
18	$0.5(1.8)(2.0)$	$0.0(2.6)(2.7)$	$0.7(3.0)(1.8)$
19	$0.7(1.9)(2.3)$	$0.6(2.8)(2.9)$	$0.9(3.3)(2.0)$
20	$0.9(1.9)(2.5)$	$1.1(3.0)(3.0)$	$1.1(3.6)(2.2)$

TABLE 5.7: Fits to the η_b correlator ratios on the various ensembles for $a_s m = 2.75$. For each combination, we report: the mean and the statistical and systematic uncertainties.

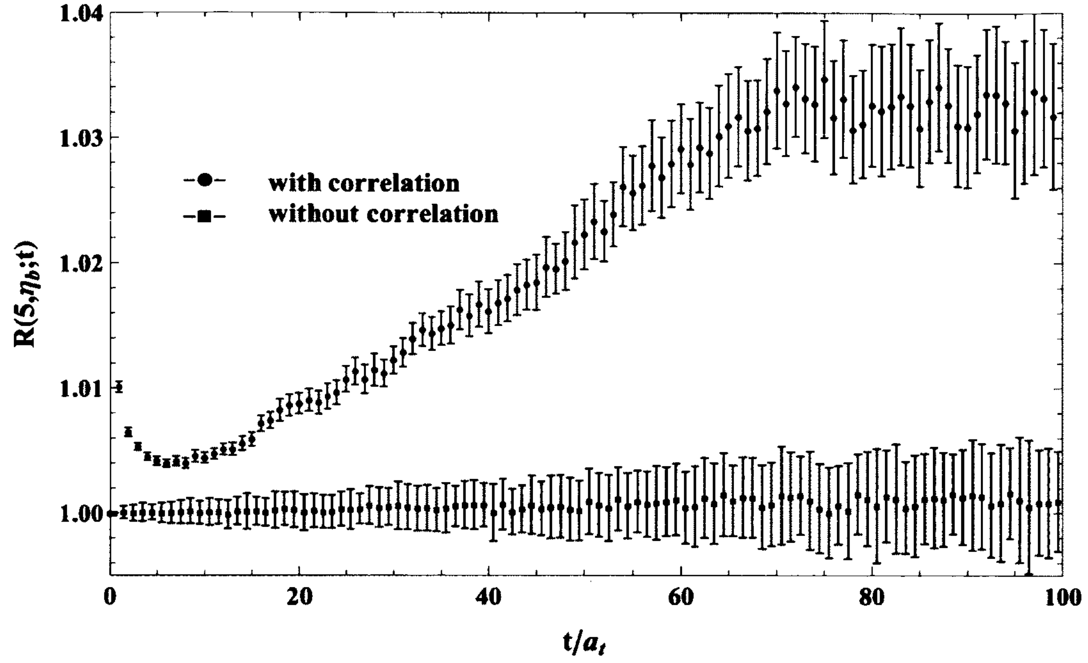

FIG. 5.7: The ratio $R(5, \eta_b; t)$ computed with and without the correct correlation between the η_b and many-pion system on the $20^3 \times 256$ ensemble, as discussed in the main text. The shift (difference from unity) is only apparent when correlations are included.

evaluating $\frac{\sum_c C_{\bar{b}b}(c) C_{n\pi}(c+\delta c)}{[\sum_c C_{\bar{b}b}(c)][\sum_c C_{n\pi}(c+\delta c)]}$, where $C_X(c)$ represents the correlation function for the quantity X measured on configuration c, and δc is either a constant displacement or a random shift. In both cases, the removal of the correlation eliminates the signal for an energy shift. This is shown for the η_b with $n = 5$ in Fig. 5.7 for random shifts, and the same qualitative effect is seen for all choices of the density and quarkonium state that are considered.

To summarise the analysis of the correlator ratios for the S-wave quarkonium states, Fig. 5.8 shows the isospin density dependence of the energy shifts, $\Delta E_{n;\bar{b}b}$, for both the Υ and η_b channels. Figure 5.9 additionally shows the derivative $\mathrm{d}(\Delta E)/\mathrm{d}\rho_I$, approximated by the finite difference $(\Delta E_{n;\bar{b}b} - \Delta E_{(n-1);\bar{b}b})L^3$, taking into account the strong correlations between the energies at different n. Results are presented for the ranges of isospin charge density where a statistically meaningful extraction of the energy shift can be made. As can be seen in Fig. 5.8, there is a statistically significant negative energy shift for much of the range of isospin density that we have investigated. The magnitude of this shift first increases as the isospin density is increased, before flattening off at a value of about 3 MeV and possibly decreasing for large ρ_I, albeit with increasing uncertainty. A consistent picture is found from the derivatives shown in Fig. 5.9. It is interesting to note that the saturation occurs at the point at which a marked change in the energy density of the many-pion system was observed in Ref. [11], and is likely caused by the changing nature of the screening medium at this point. The increase of the energy shift at low densities is in line with the expectations of the potential model in Ref. [5], but the energy shift is numerically larger than in the model (note that the potential model was based on lattice results for the screening of the static potential at $m_\pi \sim 320$ MeV [47], whereas the present NRQCD calculations were done with $m_\pi \sim 390$ MeV). The saturation effect was not predicted by the model; since the model was developed using the measured shifts in the potential in the low density region, so this is not surprising.

We have performed these calculations for all three ensembles of configurations but have only been able to access a limited range of densities with the current statistical precision. The results from all of the ensembles are consistent in the region in which they overlap. The $16^3 \times 128$ ensemble provides the largest density range.

We also consider the shifts in the splitting between the η_b and Υ energies in medium as a function of the density. We extract these shifts by calculating the correlated differences between the individual energies using the bootstrap method. A summary of the isospin charge dependence of this splitting is shown in Fig.5.10. It can be seen that the Υ energy is shifted slightly more than the η_b energy by the presence of the medium.

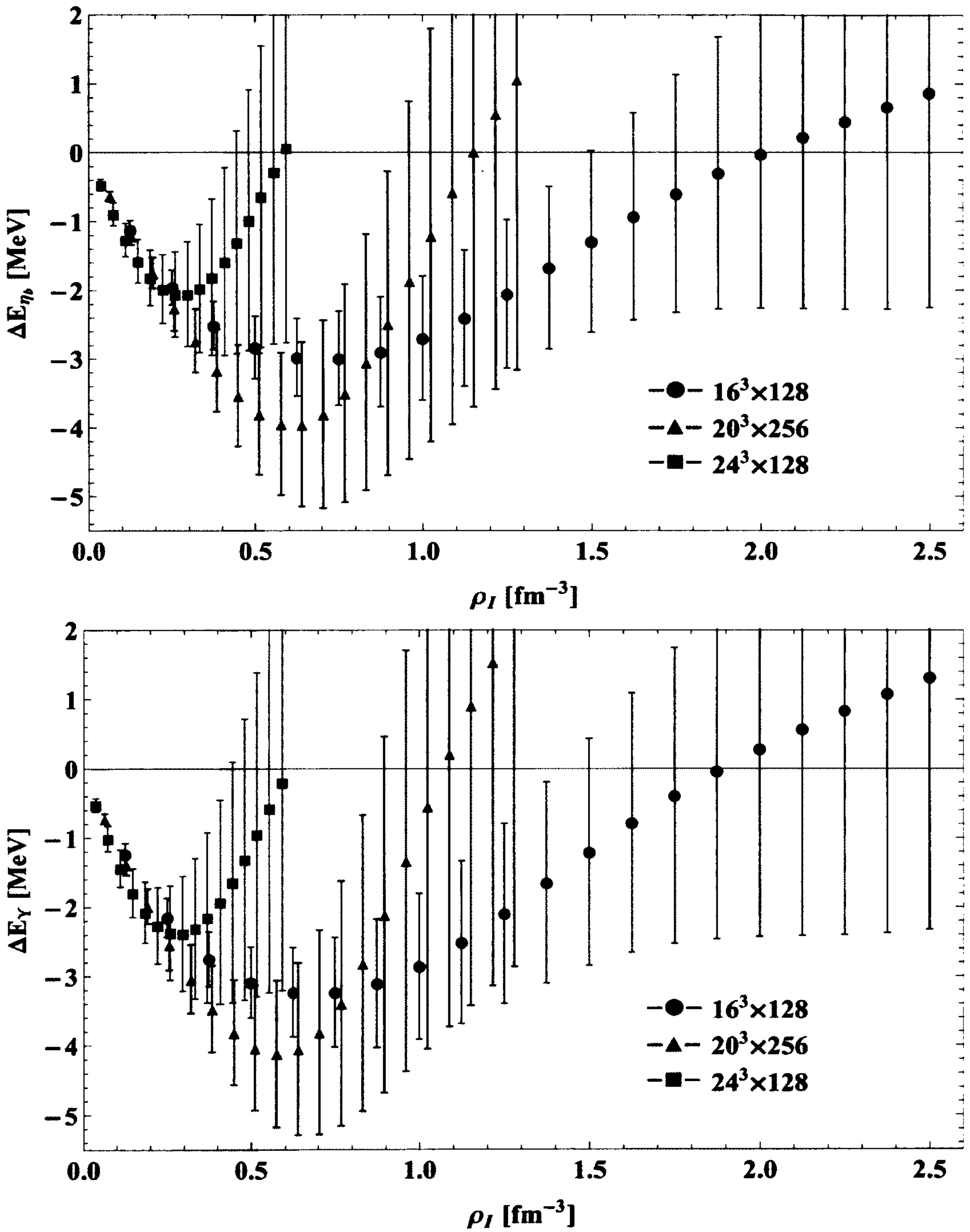

FIG. 5.8: The dependence of the energy shift on the isospin charge density is shown for the three lattice volumes for the η_b (upper panel) and Υ (lower panel). The shaded vertical band in each plot shows the region where there is a peak in the ratio of the pionic energy density to the Stefan-Boltzmann expectation (see Fig. 22 of Ref. [11]).

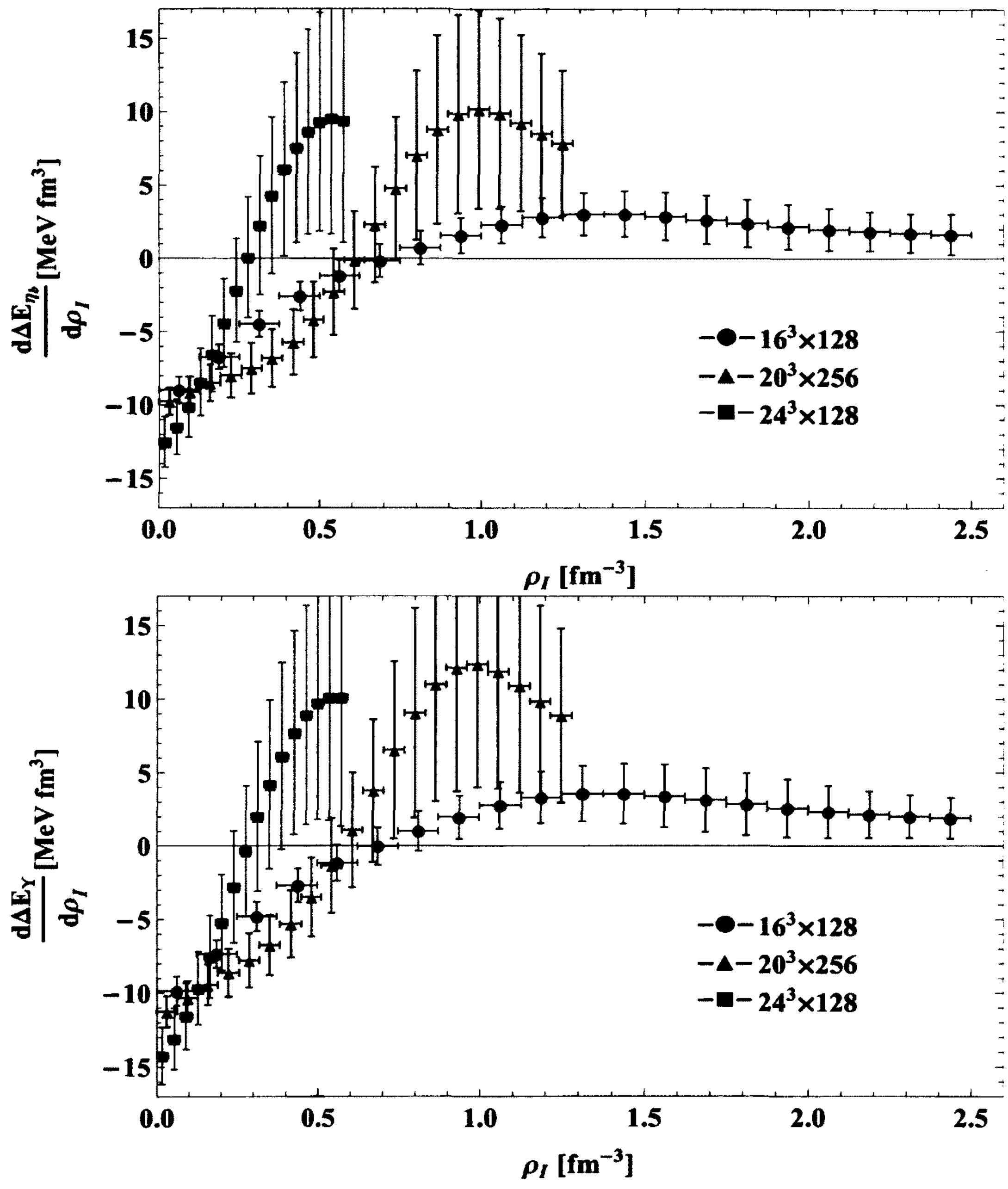

FIG. 5.9: The slope $d(\Delta E)/d\rho_I$ of the η_b energy shift (upper panel) and Υ energy shift (lower panel), approximated using correlated finite differences. The data sets and shaded bands are as described in Fig. 5.8.

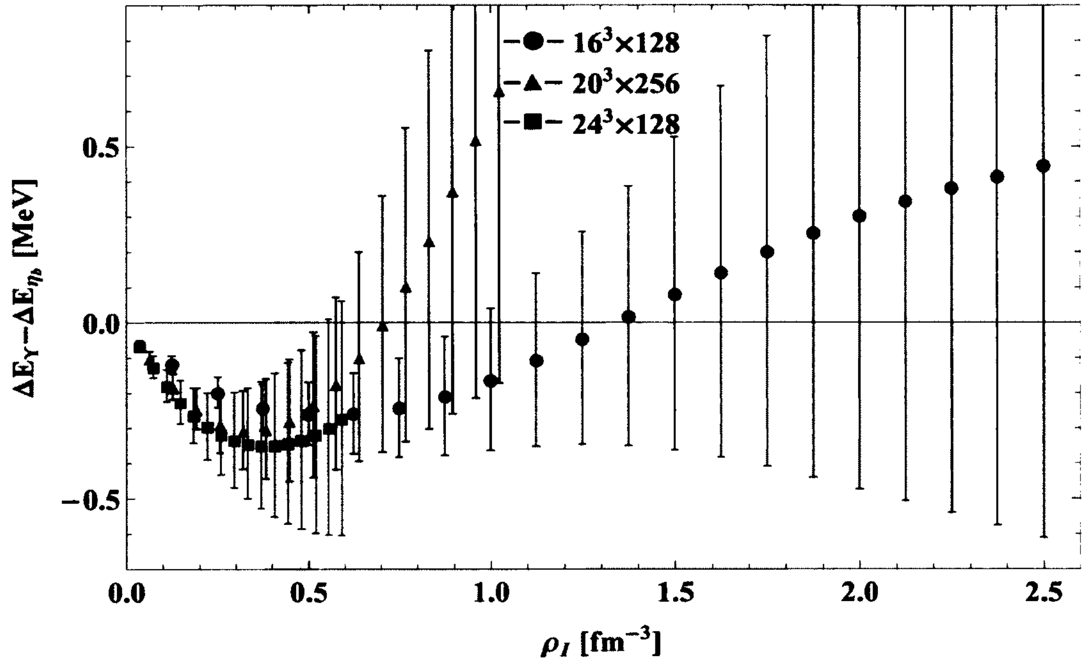

FIG. 5.10: Isospin density dependence of the shift of the S-wave hyperfine splitting between the Υ and η_b states in medium.

5.3.6 P-wave states

We also analyze the lowest-energy P-wave quarkonium states, h_b, χ_{b0}, χ_{b1} and χ_{b2}, in medium. We find that we cannot resolve differences between the medium effects for these different states and so consider a spin average of their energies. In order to extract the spin-averaged in-medium energy shift

$$\begin{aligned}\Delta E_{n;\overline{1P}} &= \tfrac{3}{12}\Delta E_{n;h_b} + \tfrac{1}{12}\Delta E_{n;\chi_{b0}} \\ &+\tfrac{3}{12}\Delta E_{n;\chi_{b1}} + \tfrac{5}{12}\Delta E_{n;\chi_{b2}},\end{aligned} \tag{5.13}$$

we construct the following product of fractional powers of the individual ratios,

$$\begin{aligned}R(n,\overline{1P};t) &= R(n,h_b;t)^{\frac{3}{12}}\ R(n,\chi_{b0};t)^{\frac{1}{12}} \\ &\times R(n,\chi_{b1};t)^{\frac{3}{12}}\ R(n,\chi_{b2};t)^{\frac{5}{12}},\end{aligned} \tag{5.14}$$

which at large t will behave as

$$R(n,\overline{1P};t) \longrightarrow Z_{n;h_b}^{\frac{3}{12}} Z_{n;\chi_{b0}}^{\frac{1}{12}} Z_{n;\chi_{b1}}^{\frac{3}{12}} Z_{n;\chi_{b2}}^{\frac{5}{12}} \exp(-\Delta E_{n;\overline{1P}}t). \tag{5.15}$$

We also consider the analogous S-wave spin-average combination

$$R(n,\overline{1S};t) = R(n,\eta_b;t)^{\frac{1}{4}} \; R(n,\Upsilon;t)^{\frac{3}{4}}. \tag{5.16}$$

Since the P-wave quarkonium correlators are themselves statistically noisier than the S-wave correlators (see Figs. 5.1 and 5.2), the precision with which we can extract the P-wave energy shifts is reduced. In our fits to these correlators, we choose $t_{\mathrm{min}} = 20$ and $t_{\mathrm{max}} = 40$ and get systematic error by shifting fitting windows ± 5 time slices as before. Fig. 5.11 shows representative correlator ratios for the spin average $P-$wave state for the $20^3 \times 256$ and $16^3 \times 128$ ensembles, and Fig. 5.12 summarises the extracted energy shifts. Here we only show results from the $16^3 \times 128$ and $20^3 \times 256$ ensembles, because the P-wave results on the $24^3 \times 128$ ensemble were too noisy. The potential model expectation is that the P-wave shift will be larger than the S-wave shift, and our lattice results confirm the expectation. In the lower panel of Fig. 5.12 we show the correlated differences between the spin-averaged P-wave and S-wave energy shifts.

5.3.7 Heavy-quark mass dependence

As discussed in Section 5.3.1, we have performed calculations for four different values of the heavy-quark mass, $a_s m$, ranging from the bottom-quark mass down to ~ 1.5 times the charm-quark mass. The analysis of the in-medium correlators and ratios is very similar for all masses and we do not present it in detail. To investigate the variation of the energy shifts as a function of the heavy-quark mass we

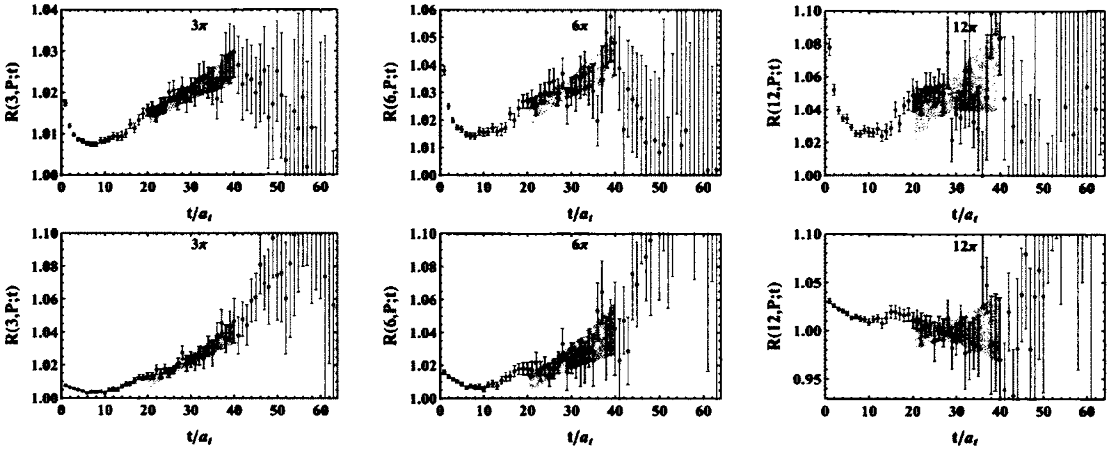

FIG. 5.11: The correlators ratios corresponding to the spin-averaged P-wave energy in a medium corresponding to isospin charges n = 3, 6, and 12. Data are shown for $a_s m = 2.75$ on the $20^3 \times 256$ (upper) and $16^3 \times 128$ (lower) ensembles.

compute $\Delta E_{n,\bar{b}b}(a_s m) - \Delta E_{n,\bar{b}b}(a_s m = 2.75)$ using the bootstrap method. Because of correlations between the measurements for different values of the heavy-quark mass, this provides a more statistically precise determination of the difference than would be evident from a naive comparison. Figure 5.13 shows these energy differences for the different values of $a_s m$. It is apparent that the strength of the energy shift in both η_b and Υ increases as the heavy-quark mass decreases, in line with expectations from the potential model discussed above. Since the quarkonium states for lower heavy-quark masses are physically larger, they probe regions of larger quark–anti-quark separation where the potential shift is more significant.

5.4 Charmonium in medium of non-zero isospin chemical potential

As the suppression of the propagation of J/ψ particles thourgh a hot dense medium has been observed for charmonium in various experiments at SPS, RHIC,

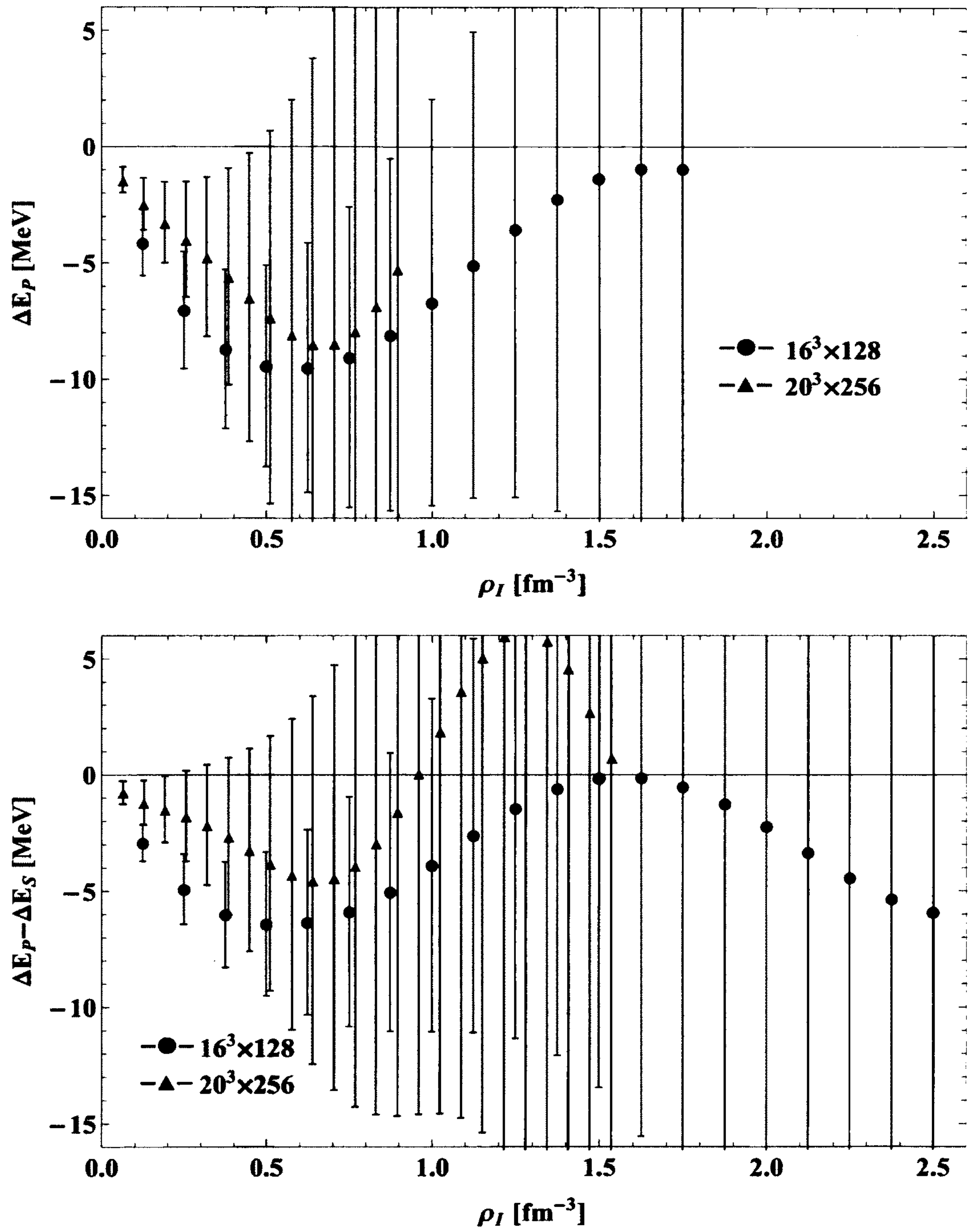

FIG. 5.12: Upper panel: the shift in the spin-averaged $1P$ energy as a function of the isospin charge density. Lower panel: the shift of the spin-averaged $\overline{1P} - \overline{1S}$ splitting. The vertical band shows the isospin density at which the pionic energy density is peaked relative to the Stefan-Boltzmann expectation. The results are for $a_s m = 2.75$.

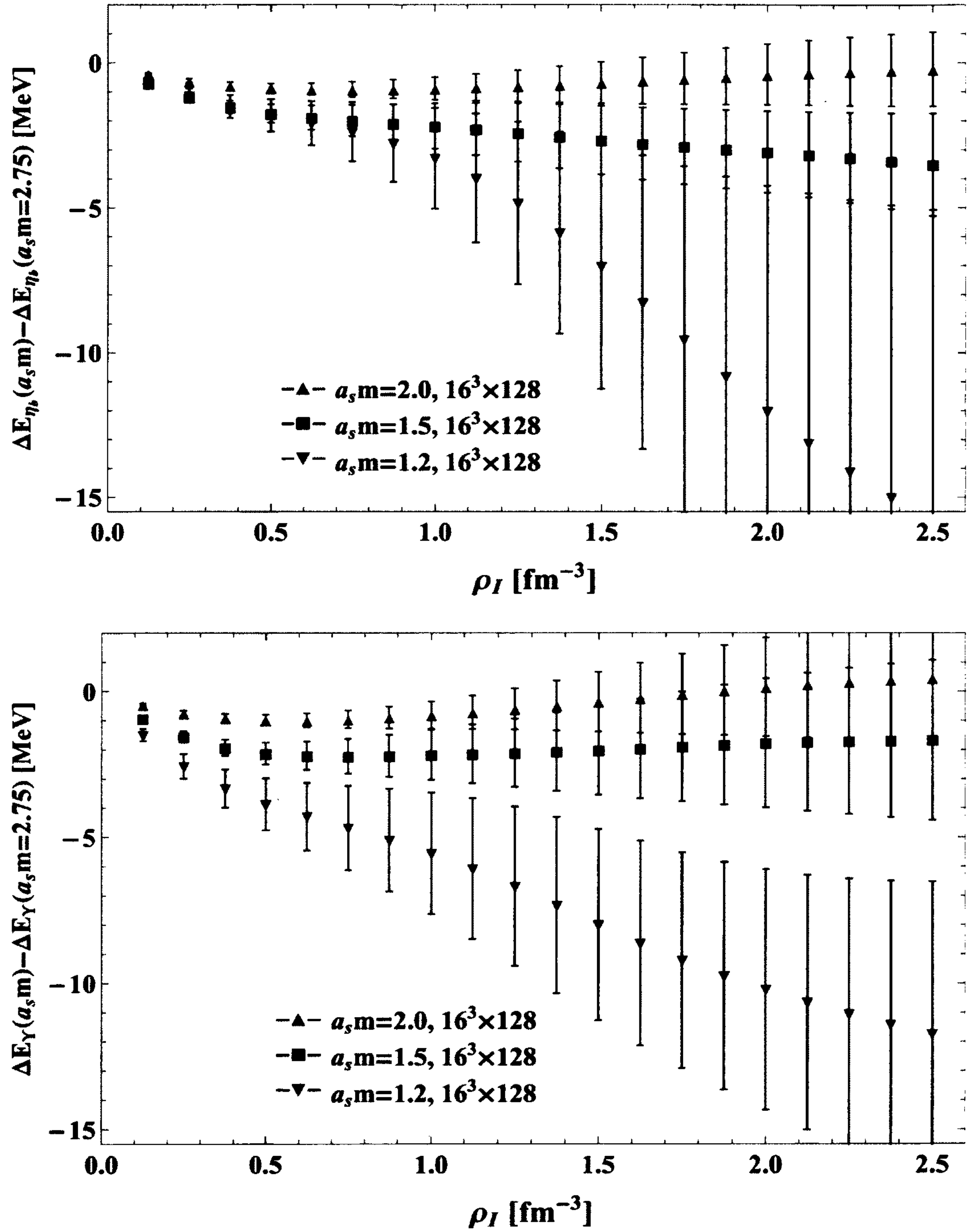

FIG. 5.13: The difference of the η_b (upper) and Υ (lower) energy shift for a given heavy quark mass from the shift for $a_s m = 2.75$ is shown as a function of the isospin charge density. Results are shown for the $16^3 \times 128$ ensemble.

and LHC[3]. it is very interesting to investigate the ralated effect of isospin density on charmonium non-perturbatively from first principles. From the above study of bottomonium energy shifts in the media of different isospin chemical potential, we found that the energy shifts become more significant as the mass of bottom quark decreases. This suggests that the energy shifts of charmonium states will be more significant than the bottomonium enery shifts. Similar to the study of the bottomonium energy shift, we extract the energy shift of charmoniums in medium of non-zero isospin chemical potential from its free energy from the following ratio,

$$R(n, \bar{c}c; t) = \frac{\langle \mathcal{O}_{\bar{c}c}(t)\mathcal{O}_{n\pi^+}(t)\tilde{\mathcal{O}}^{\dagger}_{\bar{c}c}(0)\mathcal{O}^{\dagger}_{n\pi^+}(0)\rangle}{\langle \mathcal{O}_{\bar{c}c}(t)\tilde{\mathcal{O}}^{\dagger}_{\bar{c}c}(0)\rangle\langle \mathcal{O}_{n\pi^+}(t)\mathcal{O}^{\dagger}_{n\pi^+}(0)\rangle}; \qquad (5.17)$$

where $\mathcal{O}_{\bar{c}c}(t)$ is the interpolating operator for charmonium states, for example $\mathcal{O}_{\bar{c}c}(t) = c\gamma_5\bar{c}$ for η_c and $\mathcal{O}_{\bar{c}c}(t) = c\gamma_i\bar{c}$, where $i = 1, 2, 3$ for J/ψ.

We employed the same fermion action as those used in generating light quark propagators to compute charm quark propagators. As in Ref. [59], the charm quark mass is tuned so that the ratio of masses of η_c and $\Omega(sss)$ recovers its experimental values, and the bare anisotropic parameter γ_c for the charm quark is tuned to be $\gamma_c = 3.988$ so that the correct energy-momentum dispersion relation is recovered at low momentum. The renormalized anisotropic parameter ξ_{η_c} calculated from the following energy-momentum dispersion relation of charmonium states

$$E^2_{\eta_c}(\mathbf{p}) = E^2_{\eta_c}(\mathbf{0}) + \xi^2_{\eta_c}\,\mathbf{p}^2 \qquad (5.18)$$

is consistent with 3.5. In order to get better signal for the $R(n, \bar{c}c; t)$ ratio, we computed colorwave propagators for charm quarks by using the same set up as those for light quark propagators. Correlation functions for charmonium states at rest are similarly calculated in momentum space by choosing quark propagators with suitable momenta, and more details can be found in Section 2.3.

5.4.1 η_c and J/ψ

Charmonium correlation functions, $C_{\eta_c}(t)$ and $C_{J/\psi}(t)$ are computed on the ensemble B1 with color-wave propagators by employing following point source interpolators for η_c and J/ψ,

$$\begin{aligned} \mathcal{O}_{\eta_c} &= \bar{c}\gamma_5 c, \\ \mathcal{O}_{J/\psi} &= \bar{c}\gamma_i c, \end{aligned} \tag{5.19}$$

where $i = 1, 2, 3$. By choosing different combinations of quark momenta, charmonia with different momenta can be easily constructed. In the current study only charmonia at rest are considered. In order to get better overlap on to the ground state, color-wave propagators with zero quark momentum are used in constructing charmonia at rest. Unlike the pion correlator, charmonium correlators have additional contributions from a disconnected piece, which we ignore in this study. These contributions are expected to be small as has been found in Ref. [60]. The η_c and J/ψ correlation functions are shown in Fig. 5.14, and the corresponding effective mass plots are shown in Fig. 5.15, where a clear plateau region can be seen at later time slices. Ground state energies, E_{η_c} and $E_{J/\psi}$, are extracted by fitting a single exponential to correlation functions over time slices, $t = [27, 53]$. Statistical errors are computed from bootstrap method, and systematic errors are computed by shifting fitting windows forward and backward 5 time slices. The extracted ground state energies are included in Table. 5.8.

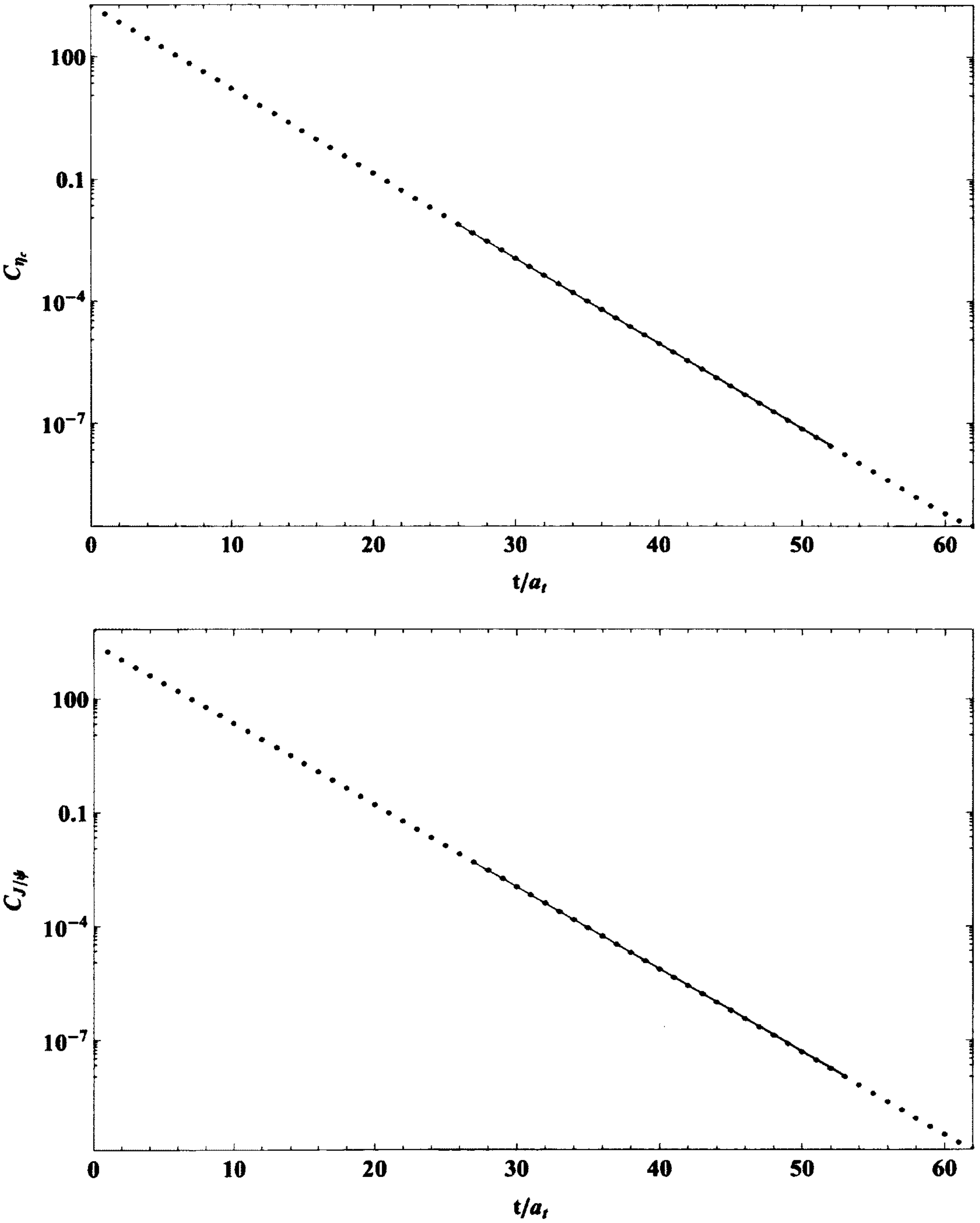

FIG. 5.14: In upper (lower) figure, the $C_{(\eta_c)}(t)$ ($C_{J/\psi}(t)$) computed on the $16^3 \times 128$ ensembles are shown.

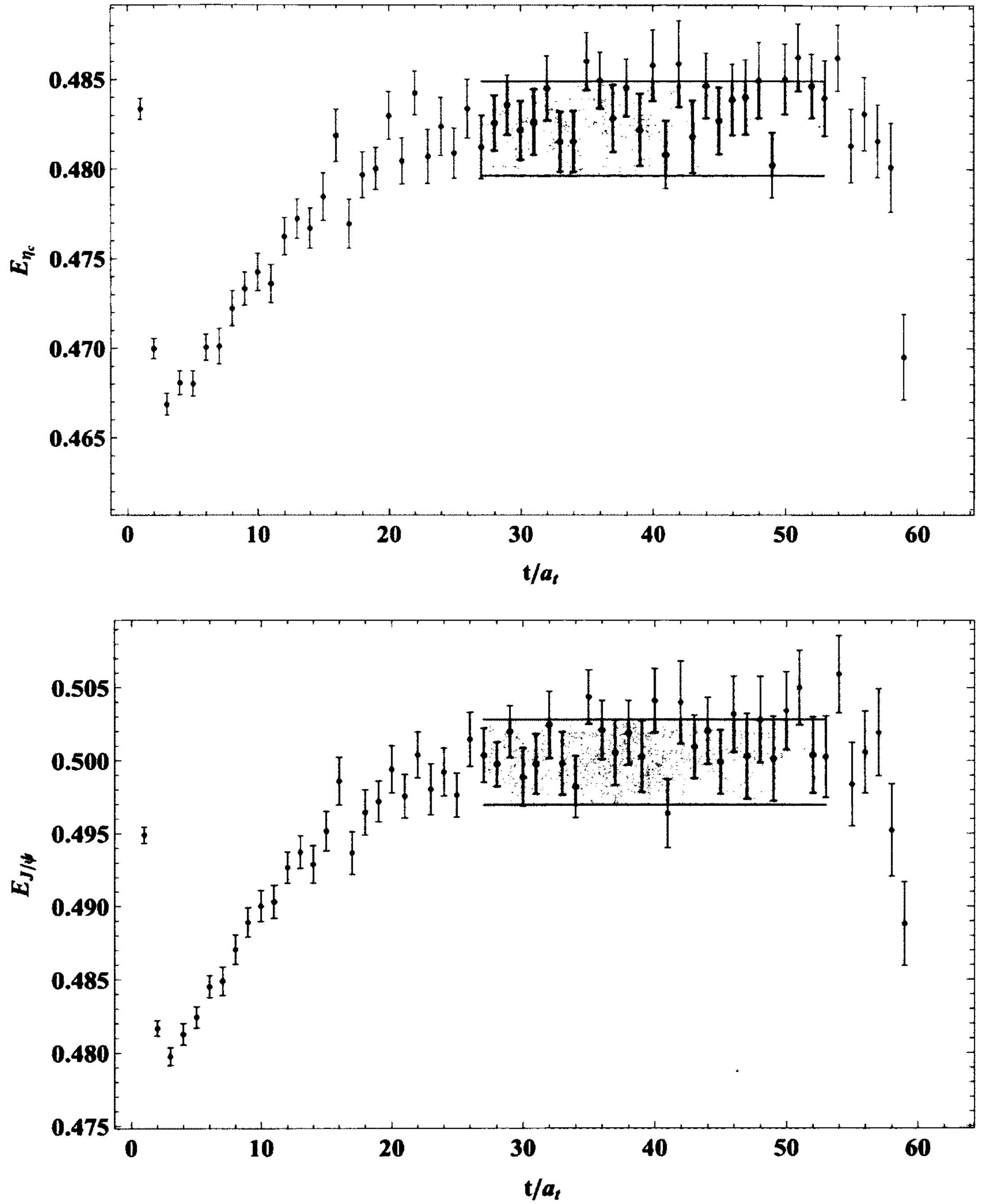

FIG. 5.15: In upper (lower) figure, the effective mass plot of η_c (J/ψ) computed from the corresponding correlation functions on the $16^3 \times 128$ ensembles are shown. Also the extracted ground state energies and the corresponding fitting ranges are shown as blue bands.

TABLE 5.8: Extracted ground state energies of η_c and J/ψ on the $16^3 \times 128$ ensemble, where the first uncertainty is the statistical uncertainty, and the second uncertainty is the systematic uncertainty.

	$a_t E_{c\bar{c}}$	$E_{c\bar{c}}$ (MeV)
E_{η_c}	0.4822(12)(23)	2673.3(6.7)(12.8)
$E_{J/\psi}$	0.5000(14)(26)	2772.0(7.8)(14.4)

5.4.2 Charmonium scattering length

By following the same procedure laid out in Section. 5.3.3, the scattering length of η_c (J/ψ) and π, $a_{\eta_c,\pi}$ ($a_{J/\psi,\pi}$) can be extracted by applying the Lüscher formula in Equation (5.9) from the energy shift of an interacting system of one η_c (J/ψ) and π from their free energy in a finite volume. The extracted phase shifts for charmonium states are tabulated in Table 5.9, which are larger than the $a_{\eta_b,\pi}$ and $a_{\Upsilon,\pi}$ calculated in Section. 5.3.3. A larger scattering length indicates a stronger interaction between the charmonium and pion than the bottomonium and pion. As only the result from one volume is available, no extrapolation to the infinite volume is attempted.

TABLE 5.9: The η_c–π and J/ψ–π phase shifts extracted using the Lüscher method on the $16^3 \times 128$ ensemble.

	p^2/m_π^2	$(p\cot\delta(p))^{-1}$[fm]	$m_\pi/(p\cot\delta(p))$
η_c	−0.0149(16)	0.0383(46)	0.0759(91)
J/ψ	−0.0170(18)	0.0442(53)	0.0875(104)

5.4.3 Charmonium energy shift

Similar to the study of bottomonium energy shift in the media of different isospin density, charmonium energy shifts are extracted from the ratio defined in Equation. (5.17). Such ratios rely on correlations between $C_{\eta_c}(t)/C_{J/\psi}(t)$ and $C_{n\pi}(t)$ calculated on the same configurations. Without such correlation, the ratio $R(n, \bar{c}c; t)$

will be consistent with 1.0 as in this case charmonium and pion correlation functions are independent. As a test, we deliberately turn off such correlations by using η_c (J/ψ) and $n\pi$ correlation functions from two different random configurations, or from two shifted configurations according to the following equation,

$$R'(n, \bar{c}c; t) = \frac{\langle C^c_{n\pi}\ C^{c+\delta c}_{\eta_c}\rangle}{\langle C^c_{n\pi}\rangle\langle C^{c+\delta c}_{\eta_c}\rangle}, \tag{5.20}$$

where C^c denotes the correlation function calculated on configuration c, and $\langle\ \rangle$ denotes averaging over all configurations after summing over different time sources on individual configurations, that is $\langle C^c_{n\pi}\ C^{c+\delta c}_{\eta_c}\rangle = \langle\langle C^c_{n\pi}\ C^{c+\delta c}_{\eta_c}\rangle_t\rangle_c$. The δc denote the number of configurations are shifted between the $n\pi$ and η_c correlation functions, for example if they are randomly shifted δc is a random integer. In Fig. 5.16, the shifted ratio defined in Equation. (5.20) with $\delta c = 50$ is compared with the ratio defined in Equation. (5.17) with matching configurations. It is clear that when correlations between charmonium and pion correlation functions are turned off, the ratio recovers the case for independent correlation functions.

By computing the ratio $R(n, \bar{c}c; t)$ correctly, that is with matching configurations, the energy shifts of charmonium states can be extracted by fitting to a single exponential at later time slices

$$R(n, \bar{c}c; t) = Z_{\bar{c}c}\exp((E_{\bar{c}c} + E_{n\pi} - E_{\bar{c}c.n\pi})t) = Z_{\bar{c}c}\exp(-\Delta E_{\bar{c}c,n}t), \tag{5.21}$$

where $E_{\bar{c}c,n\pi}$ is the ground state energy of a system having one $\bar{c}c$ and n π's, and $\Delta E_{\bar{c}c,n}$ is the shift in their energy from its vacuum value. Because of interactions between charmonium states and pions, the ground state energy will be different from the sum of the energies of a $\bar{c}c$ system and a n-π system.

The ratio $R(n, \eta_c; t)$ for different n's are shown in Fig. 5.17, and similar plots

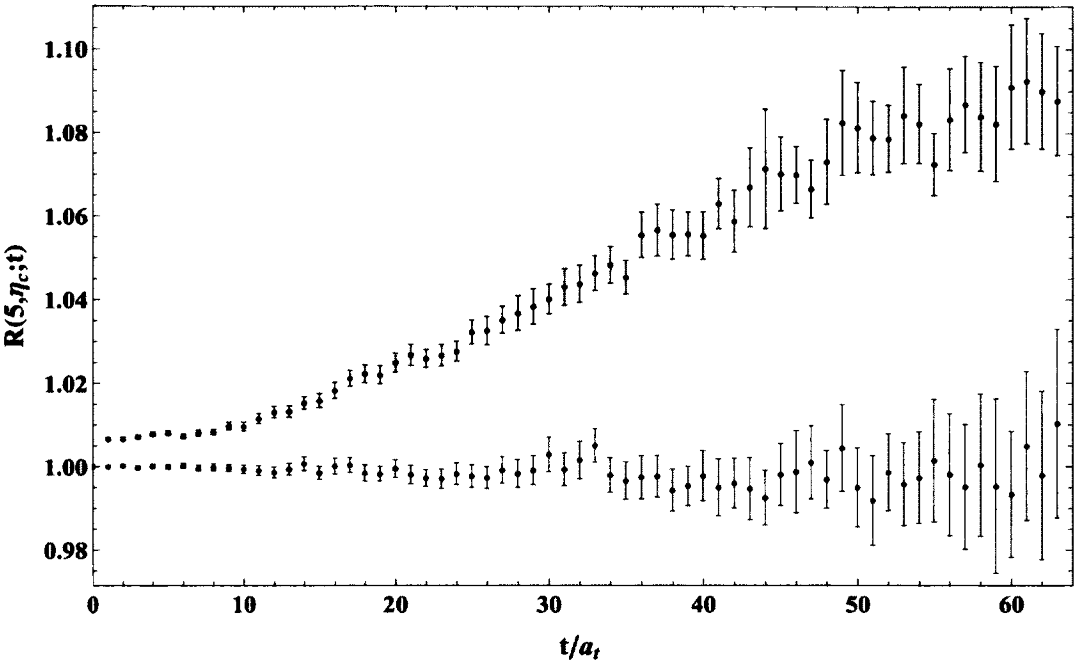

FIG. 5.16: In this figure, correlated contraction and uncorrelated contraction by shifting 50 configurations are compared. When correlations among $C_{\eta_c}(t)$ and $C_{n\pi}(t)$ are taken away, we indeed recover the result for uncorrelated correlation functions such that the ratio is consistent with 1.0.

for $R(n, J/\psi; t)$ are shown in Fig. 5.18. Energy shifts $\Delta E_{\bar{c}c,n}$ are extracted from the ratio $R(n, \bar{c}c; t)$ by fitting to Equation. [5.21]. The fitting range is chosen to be $t = [20, 40] \pm 5$ to minimize contaminations both from excited states and thermal states for all n's, which are also consistent with choices made in the bottomonium study to make the comparison easier. The central value of the $\Delta E_{\bar{c}c,n}$'s are extracted from time slices $t = [20, 40]$. The statistical uncertainties are computed from bootstrap methods, and the systematic uncertainties are calculated by shifting fitting windows forward and backward 5 time slices. The single exponential fits to the ratio are also shown in Fig. 5.17 and Fig. 5.18 as shaded bands The extracted energy shifts and statistical uncertainties and tabulated in Table. 5.10, and are shown as a function of isospin density in Fig. 5.19.

The quantitative behavior of the charmonium energy shift for η_c and J/ψ in media of different isospin density is consistent with those for bottomonium states,

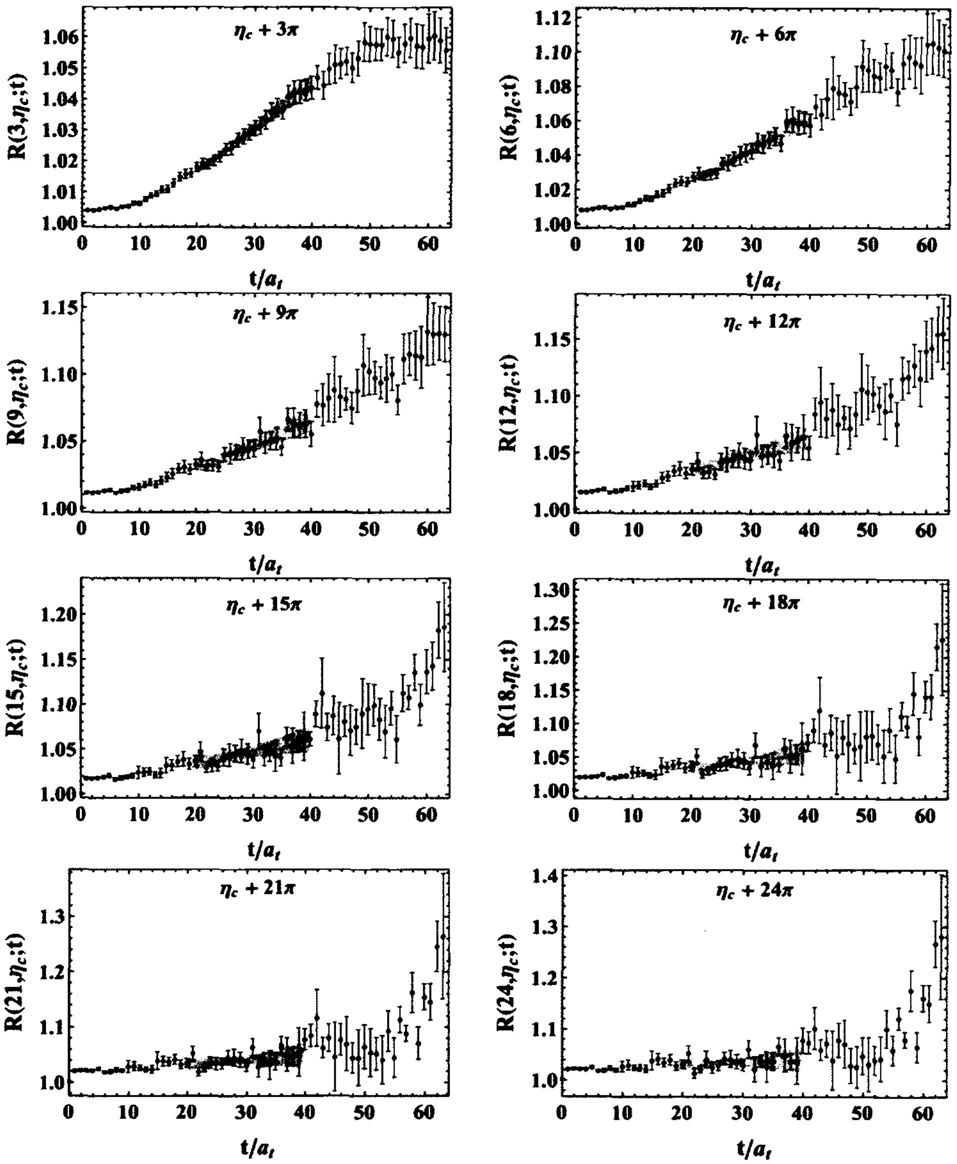

FIG. 5.17: The ratios $R(n, \eta_c; t)$ for different n's computed on the $16^3 \times 128$ ensemble are shown in this figure, where the shaded region is where a single exponential fit is performed. In this figure, only the statistical uncertainties are shown.

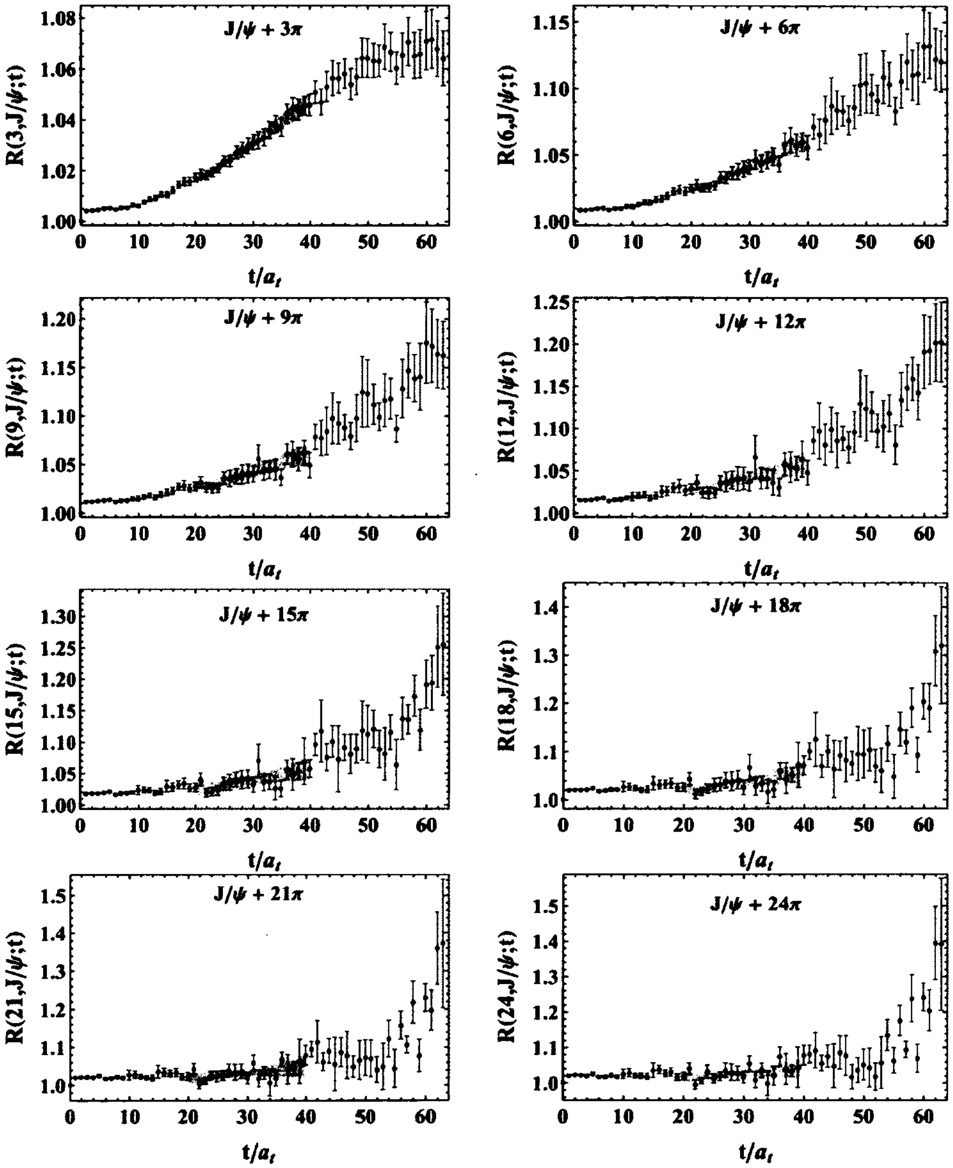

FIG. 5.18: The ratios $R(n, J/\psi; t)$ for different n's computed on the $16^3 \times 128$ ensemble are shown in this figure, where the shaded region is where a single exponential fit is performed. In this figure, only the statistical uncertainties are shown.

n	$16^3 \times 128$ $\Delta E_{n;J/\psi}$	$16^3 \times 128$ $\Delta E_{n;\eta_c}$
1	−3.75(34)(22)	−3.29(27)(25)
2	−6.53(63)(35)	−5.83(50)(37)
3	−8.45(90)(55)	−7.67(71)(37)
4	−9.67(1.19)(1.13)	−8.92(94)(36)
5	−10.35(1.51)(2.13)	−9.70(1.20)(74)
6	−10.59(1.83)(3.38)	−10.09(1.47)(1.39)
7	−10.48(2.12)(4.62)	−10.13(1.72)(2.06)
8	−10.11(2.36)(5.63)	−9.90(1.94)(2.60)
9	−9.61(2.59)(6.34)	−9.48(2.17)(2.94)
10	−9.09(2.85)(6.74)	−8.96(2.45)(3.09)
11	−8.65(3.21)(6.92)	−8.41(2.81)(3.10)
12	−8.34(3.74)(6.99)	−7.89(3.27)(3.03)
13	−8.19(4.49)(7.03)	−7.43(3.86)(2.91)
14	−8.22(5.48)(7.05)	−7.04(4.56)(2.75)
15	−8.40(6.67)(7.07)	−6.74(5.35)(2.56)
16	−8.68(7.95)(7.11)	−6.50(6.17)(2.39)
17	−8.95(9.19)(7.22)	−6.27(6.99)(2.3)
18	−9.12(10.28)(7.38)	−6.01(7.73)(2.31)
19	−9.11(11.16)(7.57)	−5.68(8.38)(2.38)
20	−8.9(11.80)(7.72)	−5.26(8.94)(2.48)

TABLE 5.10: Fits to the charmonium states' correlator ratios on the $16^3 \times 128$ ensembles. For each combination, we report: the mean and the statistical and systematic uncertainties.

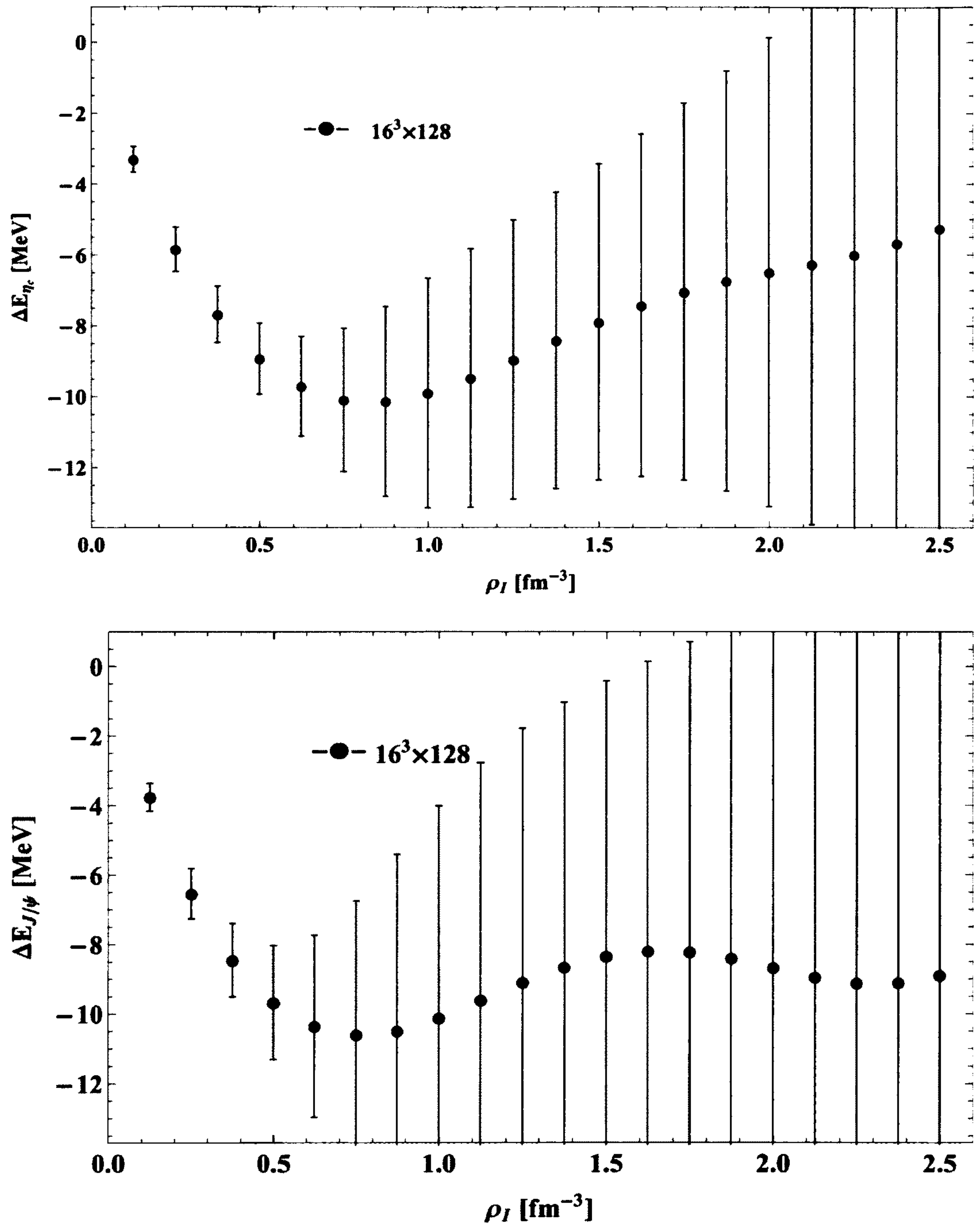

FIG. 5.19: The dependence of the energy shift on the isospin charge density is shown for the η_c (upper panel) and J/ψ (lower panel) from the $16^3 \times 128$ ensemble. The shaded vertical band in each plot shows the region where there is a peak in the ratio of the pionic energy density to the Stefan-Boltzmann expectation (see Fig. 4.8).

but is numerically larger. At small isospin density, the energy shifts of heavy quarkonium states, both bottomonium and charmonium, increases as the isospin density increases, but at around the density where the system is conjectured to transform from pion gas states to the BEC state as numerically confirmed in Chapter 4, the heavy quarkonium energy shifts start to flatten out. Such a behavior change further supports the existence of the transition from a pion gas to a BEC state.

5.5 Discussion

Heavy-quark bound states provide an important probe of the properties of a medium and have been used in this work to investigate systems of large isospin charge density created by many-pion correlators. Specifically, we have used lattice QCD to investigate how the presence of this medium modifies the energies of various bottomonium states computed from NRQCD and charmonium states from color-wave propagators. Our calculations make use of ensembles of lattices with three different physical volumes at a single lattice spacing and at a single light quark mass corresponding to $m_\pi \sim 390$ MeV for bottomonium studies and a single volume for charmonium studies. We have found a measurable decrease in the energy of both the η_b and Υ states and in the spin-averaged P-wave energy, and also for the η_c and J/ψ states. This decrease grows as the isospin charge increases, before plateauing at an isospin density at which we observed strongly non-monotonic behaviour of the energy density of the medium in Chapter. 4. The saturation of the energy shift provides further support to the conjecture that a transition from a pion gas to a Bose-Einstein condensate of pions occurs at this point. In the region of low isospin density where the energy shift is increasing, the quarkonium energy shifts are found to be qualitatively in agreement with the expectations from a potential model augmented with the hadronic screening effect found in Ref. [9], but the effect is larger.

A similar study of NRQCD quarkonium correlators in QC_2D (two-colour QCD) at non-zero quark chemical potential was recently presented by Hands *et al.* in Ref. [61]. In contrast to QCD with three colours, in QC_2D, the addition of a quark chemical potential does not result in a complex action due to the pseudo reality of reprentations of SU(2) and numerical calculations can be performed efficiently [62, 63, 64]. In Chapter. 4 it was pointed out that the phase structure of QCD at nonzero μ_I has an intriguing similarity to that of QC_2D at nonzero quark chemical potential. It is apparent that the similarities persist to the case of quarkonium energy shifts in medium as an at least qualitatively similar dependence on the charge density/chemical potential is observed in the two-colour QCD case. Recent work [65, 66, 67] has probed the connections between different gauge theories with non-zero (isospin) chemical potentials and, as the extent of this similarity is surprising, and warrants further investigation.

At the same time, by studying quarkonium–pion correlation functions on three different volumes, we have extracted η_b–π and Υ–π scattering phase shifts at low momentum. The interactions are found to be weak in both cases as expected from chiral dynamics. Since we only have studies on the charmonium states only in a single volume, we can only extract the η_c-π and J/ψ-π phase shift at single value of momentum.

CHAPTER 6

Conclusion and Outlook

Quantum Chromodynamics (QCD) plays an important role in studying hadron interactions, understanding hadron structure, and investigating non-zero temperature and non-zero chemical potential systems. However, it is extremely difficult to study strongly interacting systems analytically, as the strong interaction is non-perturbative at intermediate and low energy interacting scales; perturbation theory starts to fail and non-perturbative techniques are required. Lattice Quantum Chromodynamic (LQCD) provides a way to study such systems non-pertubatively from first principles by discretizing space and time, and useing Monte Carlo importance sampling techniques to numerically integrate the functional integrals that define physical observables as originated from QCD.

In recent years, a large amount of effort has been devoted to investigating hadronic systems and exploring phase structures at varying temperatures and chemical potentials. At zero chemical potential, the determinant of the QCD Dirac operator is positive definite, and importance sampling techniques can be applied. Although different research groups employ different discretizing techniques, they find mutual agreement that there is a crossover from a confined phase to a deconfined phase at high temperature. However the determinant of the Dirac opeartor with non-zero baryon chemical potential is complex, thus importance sampling techniques start to fail and cancellations between different field configurations are required to get correct results, thus the computational difficulty in solving such system grows exponentially. Different methods, for example reweighting, the use of imaginary chemical potential and small chemical potential expansion, have been constructed, and more details can be found in the Ref. [17].

For systems with non-zero isospin chemical potential, the sign problem that occurs in the non-zero baryon chemical potential system does not exist, and importance sampling technique can be adopted to study non-zero isospin chemical potential system directly. From χPT [1], a transition from normal haronic state to Bose Einstein Condensate state is conjectured at an isospin chemical potential $\mu_I \geq m_\pi$, and a deconfining phase transition at high temperature and non-zero isospin chemical potential is also suggested. In order to study hadronic systems and phase transitions at various temperatures and isospin chemical potentials, non-perturbative studies of these system can provide vital insight. One approach to study such system is using the grand canonical approach by generating configurations from Dirac operators of different isospin chemical potential. In Ref. [19], the authors studied systems of non-zero isospin chemical potential in this approach, and numerically identified (although with significant uncertainty) a phase transition from hadronic matter to the pion condensate (BEC) state at $\mu_I > m_\pi$, which is consistent with predictions from the χPT [1]. In this thesis, I studied systems of varying isospin chemical potentials from canonical approach by explicitly computing correlation functions of multi-meson systems with the quantum numbers of $n \leq 72\pi^+$ mesons. As there are $n!n!$ number of contractions needed in computing the n-pion correlators $C_{n\pi}(t)$ from Wick's theorem, new techniques have been developed to perform these contractions. The recursion relations of uncontracted correlation functions have been developed in Ref. [9] to reduce the number of independent contractions. I have implemented these recursion relation, generalized to momentum space, and numerically investigated systems containing up to 24 pions. Correlation functions of n-π systems, $C_{n\pi}$, receive contributions from excited states, ground states, and thermal states, resulting from a fraction of the pions propagating across the temporal boundary. In order to extract ground state energies, $E_{n\pi}$, all thermal states are required to be fitted to $C_{n\pi}$. Although systems of up to 24 π's can be calculated from the recursion relation in a manageable amount of time, extracting ground state energies becomes extremely difficult for $n \geq 12$. In order to study system containing more than 24 π's, new methodologies and longer temporal extents were required.

In order to study systems of more pions, I constructed four new algorithms by using the fact that the energy spectrum of a multi-meson system is independent of how mesons are distributed among different source locations. With these new algorithms, systems containing up to 72 pions have been studied on three anisotropic lattice ensembles, $16^3 \times 128$, $20^3 \times 256$ and $24^3 \times 128$, with physical volumes of $2, 2.5$ and 3 fm^3. Correlation functions of multi-pions systems have contaminations from both excited states and thermal states resulting from a fraction of the pions propagating backward around the temporal boundary. Thus in order to extract ground state energies, large temporal extension is necessary. For lattice ensembles with $T = 128$, the $A \pm P$ methods discussed in the Appendix can be applied to effectively double the temporal extent.

From the ground state energies of n-π systems, $E_{n\pi}$, the isospin chemical potential can be computed from a finite difference, $\mu_I(n) = E_{n\pi} - E_{(n-1)\pi}$. By studying the isospin chemical potential as a function of isospin density, ρ_I, the QCD phase diagram is explored at a fixed low temperature $\mathcal{T} \sim 20$ MeV (set by the temporal extent of the lattices used herein) for a range of $m_\pi \leq \mu_I \leq 9\ m_\pi$. In order to identify different physical states, we studied the ratio of the energy density and the zero temperature Stefan-Boltzmann expectation as a function of μ_I. The ratio increases at small μ_I, reaches a peak around $\mu_I = 1.30\ m_\pi$, starts to decrease after the peak, and eventually starts to flatten out at even larger μ_I, which suggests a change in the degrees of freedom of the system. Our interpretation of this behavior is that the system is in the state of a pion gases when $\mu_I < 1.30(7)\ m_\pi$, and it transforms to a BEC state when $\mu_I > 1.30(7)\ m_\pi$. At very large μ_I, the system becomes BCS state at asymptotically large μ_I from the perturbation QCD. Our study supports expectations of the QCD phase diagram from phenomenology studies.

The suppression of J/ψ and Υ [3] at non-zero temperature in heavy ion collision is an important diagnostic of the formation of the quark-gluon plasma and the onset of deconfinement. Such suppressing effects have been experimentally observed at SPS, RHIC and LHC. Similar changes are naturally also expected to occur near phase transitions at non-zero chemical potential and non-zero isospin chemical potential. In this thesis, I investigated the energy shift of heavy quarkonium states from first principles, and studied this suppression effect from first principles non-perturbatively. By utilizing the constructed n-pion systems, I investigated the energy shifts of bottomonium at different isospin density. Bottomonium correlation functions are computed using Non-Relativistic QCD (NRQCD), and the algorithms constructed in Chapter. 3 were used to compute n-pion correlation functions. By multiplying n-pion correlation functions and the bottomonium correlation functions on each configuration, energy shifts for different bottomoninum states have been extracted for different isospin densities. At small isospin densities the bottomonium energy shifts increases as afunction of ρ_I, however the dependence of the energy shift qualitatively changes its behavior and starts to flatten out around the same isospin density, where a transition from a pion gas to BEC state was identified from our multi-pion studies. Such a change of behavior strengthens the conjecture, that the system under goes a phase transition. According to the study of bottomonium, the energy shift of bottomonium becomes more prominent for lighter heavy quark masses, and an even larger and cleaner signal of energy shift is expected for charmonia.

By applying Lüscher's formula, scattering length can be extracted from energies of two body system in a finite volume. Since we have conducted bottomonium studies on three different voulmes, we can perform an extraction in terms of different interacting momenta to get the scattering length and effective range that parameterize the low energy interactions in the infinite volume limit. Infinite volume results are $m_\pi a_{\eta_b,\pi} = 0.039(13)$ and the $m_\pi r_{\eta_b,\pi} = 4.7(3.7)$ for the η_b state, and $m_\pi a_{\Upsilon,\pi} = 0.047(14)$ and $m_\pi r_{\Upsilon,\pi} = 5.8(3.3)$ in the case of the Υ. Both channels corresponding to a weak attractive interaction. Extrapolation to the physical pion mass according a quadratic form in Equation (5.12), scattering lengths at physical pion as $a^{(\text{phys.})}_{\eta_b,\pi} = 0.0025(8)(6)$ fm, $a^{(\text{phys.})}_{\Upsilon,\pi} = 0.0030(9)(7)$ fm, which are comparable to, and considerably more precise than estimates from phenomenological models [55, 56, 57, 58].

By applying similar computational techniques as those used in bottomonium energy shift study, charmonium energy shifts have also been investigated in media of different isospin chemical potential. In order to have better correlations with multi-pion correlators and have more clean signals for the charmoninum energy shift, charm quarks are implemented using color-wave propagators, computed with the same relativistic fermion action used in generating the light quark propagators. From the corresponding ratio of J/ψ and n-π correlation functions, energy shifts of J/ψ in the media of different isospin chemical potential can be extracted. The shape of the charmonium energy shifts is qualitatively in agreement with the bottomonium energy shifts, but with quantitatively larger negative energy shifts. Both studies from bottomonium and charmonium states strengthen the conjectured phase transition from pion gas states to BEC state around $\mu_I = 1.30(7)\ m_\pi$.

Although I have only investigated multi-pion systems in this thesis, the methods that I have developed can also be adapted to study systems with multi ρ or K mesons, and multi-species systems. By constructing moving mesons, we can also study the $I = 2$ $\pi\pi$ scattering length for a large range of interacting momenta from the energy shifts of two-pion systems with different center of mass momenta and different relative momenta as a function of the volume. Similarly, three-pion systems with non-zero momenta can also be studied with the same methods, which can provide a nice way to understand details of three-body dynamics before we turn to more phenomenologically relevant three-nucleon systems. By extending these contraction methods for multi-meson systems, we may also be able to study multi-baryon systems in the future.

APPENDIX A

Antiperiodic ± Periodic propagator method ($A \pm P$ method)

By keeping all Z^n_m factors the same as the ground state Z^n_0 extracted from the B4 ensemble, we have reconstructed the correlators corresponding to the B2 ensemble by utilizing the ground state energies extracted from the B4 ensemble[1]. In Fig. 4.1, the reconstructed effective masses are compared with those from the correlation functions computed from the B2 ensemble, showing agreement within uncertainties. The contamination from the thermal states on the $T = 128$ (B2) ensemble can clearly be seen in the rate at which the plateau region (where the ground state energy dominates) shrinks as n increases. For systems with a large number of pions, excited states have not died out before thermal states become important.

Since a temporal extent $T > 128$ is essentially required to get a clean signal for many-pion ground state energies, we have investigated the use of the $A \pm P$ method (combining propagators that satisfy anti-periodic and periodic boundary

---

[1] While we do not expect $Z^n_m = Z^n_0$ for all m because of the effects of pion interactions, deviations are expected to be small (This is also supported by thermal fits using Eq. (2.21) for small n.).

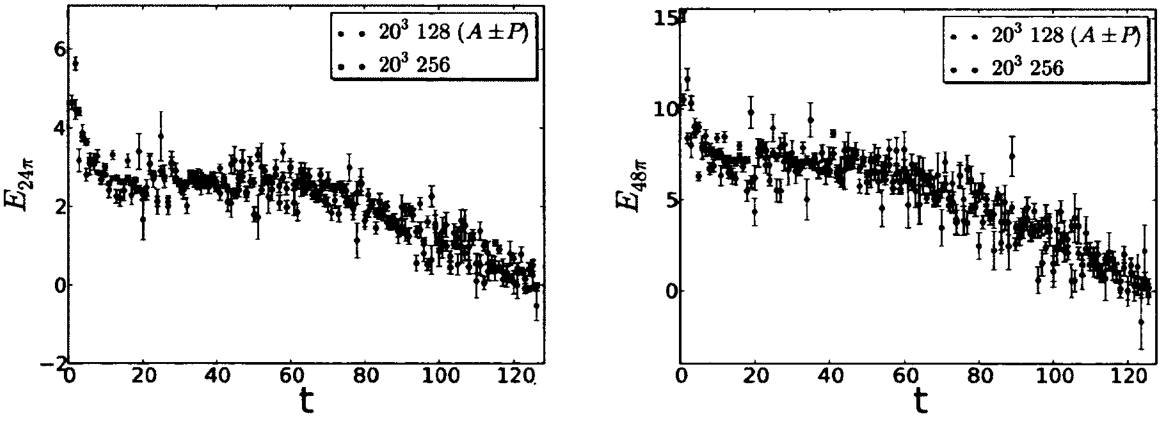

FIG. A.1: Effective mass plots for $24\pi^+$ and $48\pi^+$ correlators. The blue data are from ensemble B4 and the red data are from the $A \pm P$ method on ensemble B2. Effective mass plots are consistent between these two calculations for all n π^+ systems.

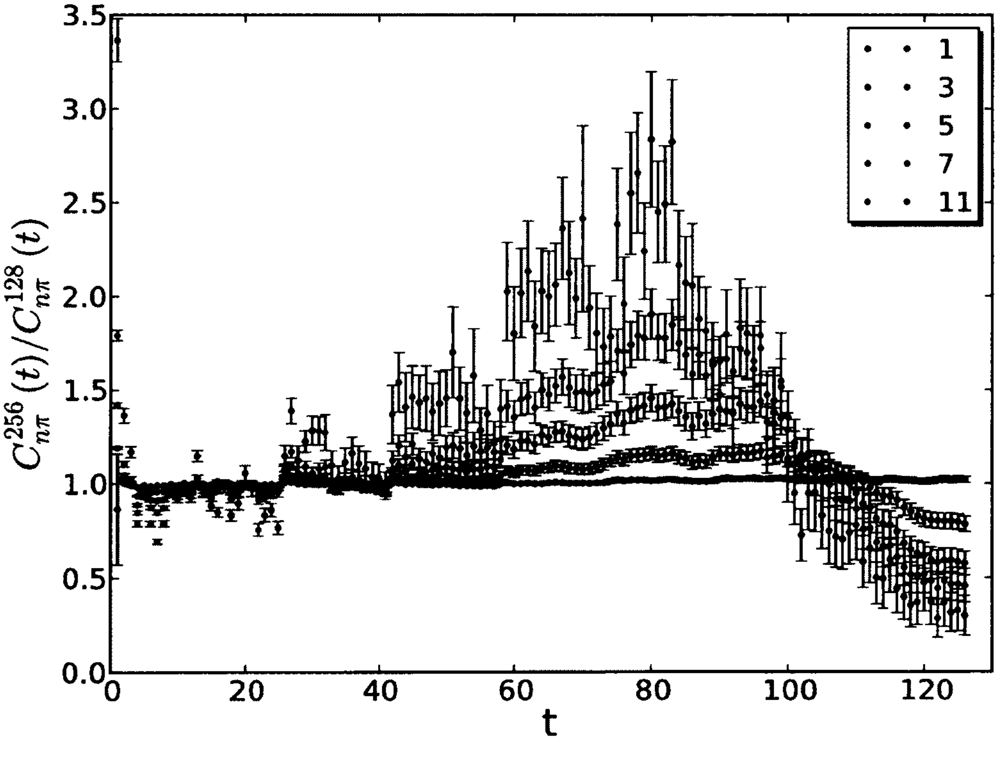

FIG. A.2: The ratio of the correlation function of n π^+'s calculated by using the $A \pm P$ method on B2 ensemble, $C^{128}_{n\pi}(t)$, compared with that from B4 ensemble, $C^{256}_{n\pi}(t)$, for $n = 1, 3, 5, 7, 11$, is shown.

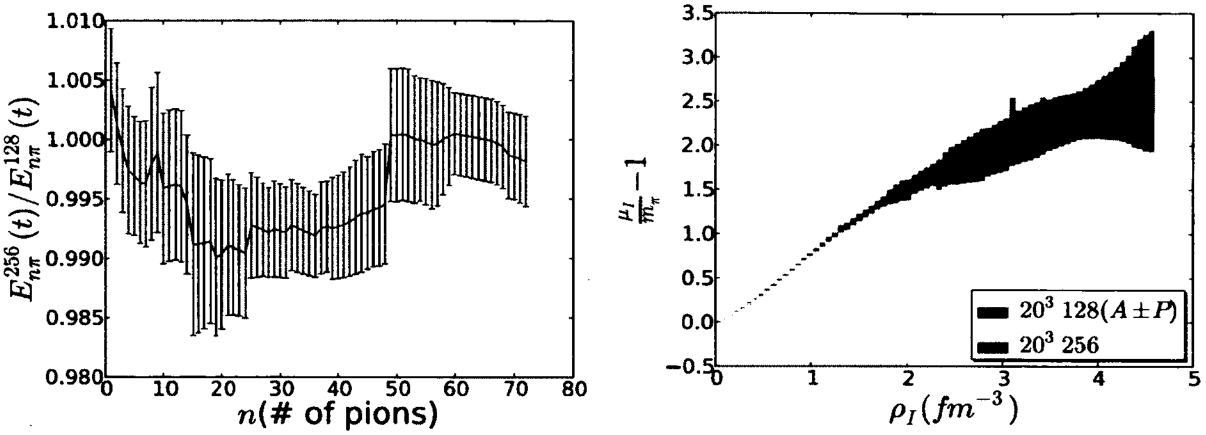

FIG. A.3: The ground state energies, $E_{n\pi}$, extracted from ensemble B2 ($E^{128}_{n\pi}$) with $A\pm P$ method are compared with those from ensemble B4 ($E^{256}_{n\pi}$) in the left plot, where the ratio of $E^{256}_{n\pi}/E^{128}_{n\pi}$ is plotted. The isospin chemical potentials, μ_I, at different densities for the two ensembles are compared in the right plot.

conditions in the temporal direction to cancel certain modes [31, 32, 33]). On the $T = 128$ B2 ensemble, we check the validity of this method in comparison to the B4 ($T = 256$) ensemble. In order to see the deviation of this method compared with those calculated directly from the $T = 256$ ensemble with anti-periodic boundary conditions in the temporal direction, effective mass plots from the two ensembles are compared in Fig. A.1, and the ratio of correlation functions from these two methods are shown in Fig. A.2. The $A \pm P$ method relies on the exact cancellation of thermal contributions, and is seen to work very well 1 π^+ system, see Fig. A.2. For systems with more than 1 π^+, the $A \pm P$ method starts fail at later time slices, however it still gives consistent results at earlier time slices, where ground state energies can be extracted. Energies and isospin chemical potentials extracted from the $A \pm P$ method are compared with those from ensemble B4 in Fig. A.3, which shows that the disagreement of extracted ground energies below 1%, and at our current precision, the $A \pm P$ method provides reliable results for the correlators we study. This gives us confidence to use the $A \pm P$ method for ensembles B1 and B3, where we could otherwise not extract ground state energies for large number of pions.

BIBLIOGRAPHY

[1] D. T. Son and M. A. Stephanov, Phys. Rev. Lett. **86**, 592 (2001).

[2] W. Detmold, M. J. Savage, A. Torok, S. R. Beane, T. C. Luu, et al., Phys.Rev. **D78**, 014507 (2008).

[3] S. Chatrchyan et al. (CMS Collaboration), Phys.Rev.Lett. **107**, 052302 (2011).

[4] Z. Shi and W. Detmold, PoS **LAT 2011**, 328 (2011).

[5] W. Detmold, K. Orginos, and Z. Shi, Phys.Rev. **D86**, 054507 (2012).

[6] A. Li, Private conversation (2012).

[7] W. Detmold, S. Meinel, and Z. Shi, Phys. Rev. D 87, **094504** (2013).

[8] D. H. Bailey et al., ARPREC: An arbitrary precision computation package, Available at http://crd.lbl.gov/~dhbailey/dhbpapers/arprec.pdf (2002).

[9] W. Detmold and M. J. Savage, Phys. Rev. D. **82**, 014511 (2010).

[10] S. Beane et al. (NPLQCD Collaboration), Phys.Rev. **D85**, 034505 (2012).

[11] W. Detmold, K. Orginos, and Z. Shi, Phys.Rev. **D86**, 054507 (2012).

[12] Particle Data Group (2012).

[13] K. Symanzik, Nucl. Phys. B **226**, 205 (1983).

[14] B. Sheikholeslami and R. Wohlert, Nucl. Phys. B **259**, 572 (1985).

[15] H.-W. Lin et al. (Hadron Spectrum Collaboration), Phys.Rev. **D79**, 034502 (2009).

[16] T. Misumi, PoS Lattice 2012: 005 (2012).

[17] O. Philipsen, arxiv:1009, 4089 (2010).

[18] S. Hands, S. Kim, and J.-I. Skullerud, Phys.Rev. **D81**, 091502 (2010).

[19] P. de Forcrand, M. A. Stephanov, and U. Wenger, PoS **LAT2007**, 237 (2007).

[20] W. Detmold, K. Orginos, M. J. Savage, and A. Walker-Loud, Phys.Rev. **D78**, 054514 (2008).

[21] S. R. Beane, W. Detmold, T. C. Luu, K. Orginos, A. Parreno, et al., Phys.Rev. **D80**, 074501 (2009).

[22] A. Stathopoulos and K. Orginos, SIAMJ. Sci. Comput **32**, 439 (2010).

[23] G. P. Lepage and P. B. Mackenzie, Phys. Rev. D. **48**, 2250 (1993).

[24] C. Morningstar and M. Peardon, Phys. Rev. D. **69**, 054501 (2004).

[25] S. Durr, arXiv:1011.2711 (2010).

[26] G. P. Lepage, From Actions to Answers: Proceeding of the TASI 1989 (1989).

[27] N. Macon and A. Spitzbart, The American Mathematical Monthly **65**, 95 (1958).

[28] M. Okamoto et al. (CP-PACS Collaboration), Phys.Rev. **D65**, 094508 (2002).

[29] P. Chen, Phys. Rev. D. **64**, 034509 (2001).

[30] B. Sheikholeslami and R. Wohlert, Nucl. Phys. B **259**, 572 (1985).

[31] T. Blum et al. (RBC Collaboration), Phys.Rev. **D68**, 114506 (2003).

[32] Y. Aoki, T. Blum, N. Christ, C. Dawson, T. Izubuchi, et al., Phys.Rev. **D73**, 094507 (2006).

[33] C. Aubin, J. Laiho, and R. S. Van de Water, Phys.Rev. **D81**, 014507 (2010), `0905.3947`.

[34] W. Detmold and B. Smigielski, Phys. Rev. D. **84**, 014508 (2011).

[35] Y. Hida et al., Quad-double arithmetic: Algo- rithms, implementation, and application, Technical Report LBNL-46996 (2000).

[36] M. Lüscher, Commun. Math. Phys. **105**, 153 (1986).

[37] M. Lüscher, Nucl. Phys. B. **354**, 531 (1991).

[38] S. Beane, P. Bedaque, A. Parreno, and M. Savage, Phys.Lett. **B585**, 106 (2004).

[39] S. R. Beane, W. Detmold, and M. J. Savage, Phys.Rev. **D76**, 074507 (2007).

[40] S. Tan, Phys. Rev. A. **78**, 013636 (2008).

[41] W. Detmold and M. J. Savage, Phys. Rev. D. **77**, 057502 (2008).

[42] B. Smigielski and J. Wasem, Phys. Rev. D. **79**, 054506 (2009).

[43] J. B. Kogut and D. K. Sinclair, Phys. Rev. D. **70**, 094501 (2004).

[44] T. Matsui and H. Satz, Phys. Lett. B. **178**, 416 (1986).

[45] P. Petreczky, J. Phys. G **39**, 093002 (2012).

[46] G. Aarts, C. Allton, S. Kim, M. P. Lombardo, M. B. Oktay, et al., JHEP **1303**, 084 (2013).

[47] W. Detmold and M. Savage, Phys. Rev. Lett. **102**, 032004 (2009).

[48] D. Son and M. A. Stephanov, Physical. Rev. Lett. **86**, 592 (2001).

[49] S. R. Beane, W. Detmold, T. C. Luu, K. Orginos, M. J. Savage, et al., Phys.Rev.Lett. **100**, 082004 (2008).

[50] W. Detmold and B. Smigielski, Phys. Rev. D. **84**, 014508 (2011).

[51] S. R. Beane, P. F. Bedaque, T. C. Luu, K. Orginos, E. Pallante, et al., Phys.Rev. **D74**, 114503 (2006).

[52] K. Yokokawa, S. Sasaki, T. Hatsuda, and A. Hayashigaki, Phys.Rev. **D74**, 034504 (2006).

[53] L. Liu, H.-W. Lin, and K. Orginos, PoS **LATTICE2008**, 112 (2008).

[54] L. Liu, PoS **LAT2009**, 099 (2009).

[55] M. E. Peskin, Nucl.Phys. **B156**, 365 (1979).

[56] G. Bhanot and M. E. Peskin, Nucl.Phys. **B156**, 391 (1979).

[57] H. Fujii and D. Kharzeev, Phys.Rev **D60**, 114039 (1999).

[58] X.-H. Liu, F.-K. Guo, and E. Epelbaum, Eur.Phys.J. **C73**, 2284 (2013).

[59] M. Dasgupta, K. Khelifa-Kerfa, S. Marzani, and M. Spannowsky, JHEP **1210**, 126 (2012).

[60] L. Levkova and C. Detar, Phys. Rev. D. **83**, 074504 (2011).

[61] S. Hands, S. Kim, and J.-I. Skullerud, Phys.Lett. **B711**, 199 (2012).

[62] S. Hands, S. Kim, and J.-I. Skullerud, Eur.Phys.J. **C48**, 193 (2006).

[63] S. Hands, P. Sitch, and J.-I. Skullerud, Phys.Lett. **B662**, 405 (2008).

[64] S. Hands, Phys. Rev. D **81**, 091502 (2010).

[65] A. Cherman and B. C. Tiburzi, JHEP. **1106**, 034 (2011).

[66] M. Hanada and N. Yamamoto, JHEP. **1202**, 138 (2012).

[67] M. Hanada, C. Hoyos, A. Karch, and L. G. Yaffe, JHEP **1208**, 081 (2012).

VITA

Zhifeng

Zhifeng Shi was born in Shihe, Chuzhou, Huaian, Jiangsu province, China on December 29, 1986. He went to Nanjing University in China and got his bachelor degree in 2008. After graduation, he continued his study on physics in the College of William and Mary, and got his master degree in 2010. Right now he is a PhD graduate student, pursuing his PhD degree in Physics and hope to get it soon.